Fatigue crack resistance of hierarchical laminated transformation-induced-plasticity maraging steel

張, 昭

出版情報：Kyushu University, 2018, 博士（工学）, 課程博士
バージョン：
権利関係：

Fatigue crack resistance of hierarchical laminated transformation-induced-plasticity maraging steel

A dissertation submitted to the faculty of engineering

Graduate school, Kyushu University, Japan

For the degree of doctor of philosophy

Presented by

ZHANG ZHAO

July 2018

Index

List of Abbreviations

EBSD	-	Electron backscatter diffraction
KAM	-	Kernel average misorientation
SEM	-	Scanning electron microscope
IPF	-	Inverse pole figure
IQ	-	Image quality
ND	-	Normal direction
RD	-	Reference direction
TD	-	Transverse direction
OICC	-	Oxide-induced crack closure
PICC	-	Plasticity-induced crack closure
RICC	-	Roughness-induced crack closure
TICC	-	Transformation-induced crack closure
TRIP	-	Transformation-induced plasticity

Nomenclature

K	-	Stress intensity factor
K_{IC}	-	Fracture toughness
ΔK_{th}	-	Threshold stress intensity factor range
ΔK_{eff}	-	Effective stress intensity factor range
l	-	Fatigue crack length
σ_a	-	Stress amplitude
N	-	Number of cycles
N_f	-	Number of cycles to failure

CHAPTER 1. General introduction

1.1 Research background

1.1.1 Present situation of high-strength steel

Advanced high strength steels with improved ductility and strength have been developed by utilizing the characteristic microstructure features, e.g. ultra-fine grains [1, 2], multi-phase microstructure [3, 4], and retained austenite showing transformation-induced plasticity (TRIP) effect [5, 6]. In particular, the TRIP effect has been extensively used in the automobile industry because extraordinary formability and shock absorption energy combined with a superior tensile strength can be realized [7]. TRIP effect primarily provides an improved elongation. The mechanism is that deformed metastable austenite transforming to martensite results in local hardening, subsequent deformation transfers to other austenite and activates this hardening process. This repetitive hardening process delays material necking phenomenon (Fig. 1.1 [8]). In fact, TRIP steel can be divided into various types characterized by second/third phase [9], the distribution of solute atoms [10, 11], the crystal structure of martensite [12, 13], and the morphology of retained austenite [14, 15]. More specifically, the combination of pre-existing ‘hard’ martensite (or bainite) and ‘soft’ metastable retained austenite can lead to achievement of high tensile strength without deterioration of ductility, and satisfy various demands of the automobile industry.

Martensitic steels have been widely applied in industrial fields such as connecting bolt, springs, bearings, pressure vessel shell, drive shafts, etc. because of the higher tensile strength, compared with ferric or austenitic steels. In fact, martensite matrix having hierarchical microstructure consists of martensite packet, block and lath boundaries within prior austenite boundary [16]. Besides, martensite matrix intrinsically contains large amount of dislocations. Under applied strain, new dislocations are generated. Due to dislocation-dislocation interaction and dislocation pile-up at boundary phenomena, back stresses are generated and result in strain hardening [16-18]. The strength level can be controlled by solution hardening, dislocation hardening, grain boundary strengthening, and precipitation hardening. Especially, intermetallic compounds precipitate during aging drastically increases the yield strength (Fig. 1.2 [19])[20, 21], because the intermetallic compounds have disloaction-pinning effect. Martensitic steel with intermetallic compounds is called maraging steel. However, the ductility of maraging steel is lower compared to that of other steels, e.g. austenitic steel.

To achieve an exceptional balance between ductility and strength, the metastable austenite, which possesses TRIP effect during deformation, has been recently applied to maraging steel, obtaining the so-called TRIP-maraging steel. This steel grade can achieve 21% total elongation with a ultimate tensile strength of approximately 1.3 GPa as shown in Fig. 1.3 [19, 22]. The microstructure of typically reported TRIP-maraging steels consist of maraging martensite/retained austenite fine laminate structure[23], which can arrest and confine crack. The retained austenite can transform to martensite, providing high work hardening capacity and uniform elongation. This instance illustrates that present development tendency of steel is moving towards ductility improvement of high-strength steel.

1.1.2 Fatigue and fatigue crack initiation

From the viewpoint of structural design, fatigue failure is the most important mechanical phenomenon in structural design. Even though the cyclic stress amplitude is lower than the yield strength, the occurrence of fatigue failure always causes catastrophic accidents in service such as in pearlitic steels [24]. In fact, fatigue crack results from locally microscopic plastic deformation [25, 26], because the material microstructure consists of heterogeneous gains in terms of size, geometry, crystallographic orientation, and dislocation quantity, and this fact determines an unevenly distributed stress on these grains. Although metal material contains multi-slip systems, one of them is preferably activated by the maximum shear stress and provides a slip plane for dislocation motion [27, 28]. Due to the irreversible gliding of dislocations [29, 30], microscopic plastic deformation forms and presents extrusion and intrusion phenomena on the material surface [31-33]. In fact, this process of micro-roughness formation is crack initiation. Simultaneously, stress concentration occurs at crack tip, and activates new microscopic plastic deformation for crack growth.

In the low cycle fatigue regime ($10^4 < N_f < 10^5$) [34], failure is caused by multi-crack initiation and subsequent crack growth and coalescence under a macroscopic yielding condition. In the high cycle fatigue regime ($10^5 < N_f < 10^7$) [35], crack initiation occurs owing to micro-yielding under a macroscopically elastic condition. In the very high cycle and gigacycle fatigue regimes ($N_f > 10^7$) [36], one of factors causing failure is fatigue crack initiation and growth from inclusions that trap environmental hydrogen. The hydrogen-related cracking can result in a fisheye feature on the fracture surface [37].

1.1.3 Fatigue propagation and fatigue crack growth rate

However, it is inevitable to cause defects during material processing. For instance, flaws, scratches and inclusions which act as stress concentration can initiate crack. Even artificial holes need to be designed in the structure steel. Moreover, overload usually occurs and influences crack propagation. In this regard, understanding fatigue crack propagation appears to be particularly important, which is not only beneficial to ensure production safety, but also to attain the maximum efficiency of the material. George R. Irwin [38] firstly proposed concept of the stress intensity factor (K) to quantify the stress severity at crack tip:

$$K = \sigma \sqrt{(\pi a)}$$

Where σ is remote applied stress, a is half of the crack length. Since Mode I crack describing brittle fracture is the most dangerous, fracture toughness is represented by K_{IC}. High value of K_{IC} indicates strong capacity of fracture resistance.

$$K < K_{IC}, \text{ (not fracture)}$$

$$K \geq K_{IC}, \text{ (fracture)}$$

Since cyclic overloads always occurs in engineering application, it is necessary to predict the fatigue propagation life through calculating fatigue crack growth rate (FCGR). There is a relationship between FCGR and stress intensity factor range (ΔK), including three stages (Fig. 1.4). Stage II_a describes near-threshold fatigue crack propagation behavior that crack starts to propagate under the condition of ΔK exceeding threshold stress intensity factor range (ΔK_{th}). Stage II_c describes ΔK approximate to K_{IC}, indicating that material is about to fracture. However, stage II_b shows a linear trend called Paris law [39] which is significantly helpful to predict the fatigue life using the equation:

$$\Delta K = K_{max} - K_{min}$$

$$dl/dN = C\,(\Delta K)^{m}$$

where l is fatigue crack length, N is number of cycles, C and m are material constants. However, FCGR decreases with stress ratio decreasing, there must be influence on fatigue resistance.

1.1.4 Fatigue crack closure

Based on stress ratio dependence of FCGR, W. Elber discovered plasticity-induced crack closure (PICC) from aluminum alloy [40]. Specifically, the elastic material provides the compressive residual stress to the plastically deformed crack surfaces, causing the fatigue crack tip premature contact. The effective stress intensity factor range, ΔK_{eff} was formulated with the stress intensity value calculated for the crack opening load (K_{op}) as follow:

$$\Delta K_{eff} = K_{max} - K_{op}$$

$dl/dN = C'\,(\Delta K_{eff})^{m'}$ (C' and m' are material constants)

Recently, a study concluded [41] that PICC effect and associated ΔK_{th} increase with (i) small crack length or (ii) material hardness under the condition of small crack. This law is characterized by high versatility involving in steels and aluminum alloys (Fig. 1.5). In addition, calculation exhibits that FCGR decreases when fatigue crack propagates from a soft to hard phase due to PICC effect increment [42]. These serial of studies reveal that the knowledge system of PICC has been established and is widely used to solve other questions.

With scientific research developing, other crack closure phenomena have been observed in metal material. They are classified through different mechanism, including

oxide-induced crack closure (OICC) [43], transformation-induced crack closure (TICC) [44, 45] and roughness-induced crack closure (RICC) [46]. In terms of OICC, S. Suresh, et. al., [47] found out the reason for the lower FCGR in moist environment than inert atmosphere. That is, oxidation layer gradually forms at crack surface, subsequent fretting oxidation is formed by compressive stress stemming from PICC [48]. In terms of TICC, martensitic transformation from metastable austenite causes volume expansion, corresponding analysis is based on the examination of austenite fraction ahead of crack tip [49]. In terms of RICC, the plastic zone size not larger than the grain size activates single shear stress. Based on this phenomenon, a zigzag crack path forms after crack crosses a few grains. Under this shear stress, the upper and lower crack surfaces relatively slip and contact each other [46]. R.O. Ritchie [50] applied 2048-T851 aluminum alloy with different grain size to conclude that coarse grain contributes to crack roughness and delay transition from Stage I to planar Stage II crack growth. Besides, Pippan [51] reported that crack surface is characterized by asymmetric morphology which is caused through the irreversible dislocations. In addition, G. T. Gray reported that [24, 52] crack surface roughness in pearlitic steel showed high microstructure dependence, because of the crack deflection along ferrite/cementite laminated microstructure.

1.2 Purpose of this study

In this study, I focus on the effect of RICC on the fatigue small crack resistance of a newly-developed high-strength alloy. During small crack evolving to long crack, ΔK_{th} and associated PICC effect significantly increase and become stable, because ΔK_{th} for long crack is determined only by Young's modulus and Poisson's ratio [41], in other

words, different metal materials have similar ΔK_{th} value under the small crack condition. Thus, the small crack resistance is important criteria for material evaluation. On the other hand, increasing PICC effect results in OICC effect increment. Specifically, fretting oxidation increases the thickness of oxide lays at crack tip with PICC effect under long crack condition, then associated compressive stress is increased to assist crack closure. That is, the OICC effect is less under the small crack condition [47, 53]. In addition, increasing small crack length also enhances crack surface roughness and associated RICC, because plastic zone size approximate to single grain size activates single shear system [50]. Therefore, understanding RICC effect on small crack behavior can contribute to material evaluation.

A type of TRIP-maraging steel (Fe-9Mn-3Ni-1.4Al-0.01C, wt.%) has great potential to be applied on present work, due to the maraging martensite/retained austenite fine laminated microstructure similar to bone (Figs. 1.6a and b), and exceptional tensile property achieving an ultimate tensile strength of approximately 920 MPa with a total elongation of about 30% [54]. In addition, different yield strength can be obtained by controlling annealing time. It is expected that TRIP-maraging steels have a robust fatigue performance. One hand, the maraging martensite/retained austenite fine laminated microstructure is similar to the pearlitic steels (Fig. 1.6c) [55], which have superior low-cycle fatigue resistance due to the cementite/ferrite fine laminated structure contributing to zigzag crack propagation and associated RICC [52]. One the other hand, TRIP can increase high-cycle fatigue and strength. It is well known that the fatigue life and strength of TRIP-aided multi-phase steels can be improved by increasing the amount of retained austenite. Local hardening and volume expansion-induced crack closure arising from martensitic transformation contribute to fatigue crack resistance, and

subsequent crack deflection is along soft region, e.g., ferrite and baintie [56]. Therefore, it is expected that austenite has positive effect on fatigue resistance in TRIP-maraging steels.

In terms of the specific work, firstly, the rotary bending fatigue tests are carried out to obtain stress amplitude-number of cycles to failure curves. Then, analysis data is to extract the intrinsic factors influencing fatigue life, because fatigue life includes extrinsic influence such as inclusion. As mentioned above, TRIP-maraging steels microstructure is characterized by fine laminate morphology, the maraging martensite with high deformation resistance probably effectively suppresses the transformation-induced volume expansion and results in a compressive residual stress. To this end, the subsequent work is to investigate the microstructural mechanism of fatigue crack propagation in order to fully understand the effect of fine laminate microstructure on roughness. Considering that friction phenomenon significantly reduces roughness height, even results in localized flat topography, particularly at high stress amplitude. It is not precise to evaluate roughness degree based on the fracture surface observation. Therefore, the following work is based on serial sectioning method to analyze the roughness evolution.

1.3 Thesis outline

The thesis consists of six chapters. All chapters are arranged in order to achieve the main theme and objectives of the research work. The specific relationship between each chapters is schematically shown in Fig. 1.7. The thesis is organized as follow:

Chapter 1 describes a general introduction of this work. A newly-developed high-strength alloy called TRIP-maraging steel has great potential in fields of the punch

forming and structural lightweight design, because of the extraordinary balance between strength and elongation by introducing TRIP effect. The motivation of this research is based on this new alloy to investigate RICC effect. The study of crack closure has been greatly developed, showing that crack closure is more effective in small crack growth. Cyclic overload accelerates fatigue crack growth rate and enable to cause catastrophic failure. However, pearlitic steels with laminate microstructure show superior low-cyclic fatigue resistance owing to RICC effect. Similar microstructure has been applied into TRIP-maraging steel. Accordingly, this new alloy is decided to investigate RICC effect on small crack resistance in the present work.

Chapter 2 generally introduces fatigue properties of the new alloy, TRIP-maraging steel, which is invented under the inspiration of superior fracture resistance of bone. This steel is characterized by a hierarchically laminated austenite/martensite microstructure, and thus exhibits an outstanding fatigue life at each stress amplitude, compared with other conventional steels, such as dual-phase steel, pearlitic steel, 304 stainless steel, etc. This excellent performance stems from TRIP and RICC.

Chapter 3 focuses on the effect of annealing time of 1 h and 8 h on the fatigue crack resistance of TRIP-maraging steel by observing the crack initiation site, propagation path and fracture surface. Our analyses show that annealing for a longer time increases austenite/martensite lamella size and connectivity of austenite. Simultaneously, increasing lamella size leads to a reduction in austenite strength; higher austenite connectivity accelerates crack propagation. In addition, remarkable roughness on the crack surface associated with the laminated structure was observed in both steels, which caused roughness-induced crack closure.

Chapter 4 illustrates the mechanism of TRIP-maraging steels to explain its exceptional high cycle fatigue resistance. The TRIP-maraging steel with fine grained austenite was used. Our analyses revealed that soft austenite region acts as a preferential crack propagation path, but the plastic deformation during crack opening involves martensitic transformation, resisting subsequent crack growth via transformation-induced local hardening or crack closure. Moreover, crack growth along the laminates and across the block boundary forms a zigzag crack path, which would act as RICC. The combined effect of these factors plays an important role in resisting fatigue crack growth at high cycle fatigue and fatigue limit.

Chapter 5 describes serial sectioning characterization to assess roughness-induced crack closure (RICC), which cannot be observed in chapter 3 and 4. This mothed presents the evolution of crack roughness. With exploring region closing to the crack front, submicrometer-scale crack surface roughness progressively appears in the 'hard' steel annealed for 1 hour; in contrast, only micrometer-scale roughness presents in the 'soft' steel annealed for 8 hours. High hardness determines strong wear resistance which enables to contribute a long-term effective RICC.

Chapter 6 summarized the results and proposed the outlook.

1.4 List of appended papers during Ph.D. period: include publications

[1]. M. Koyama, Z. Zhang, M. Wang, D. Ponge, D. Raabe, K. Tsuzaki, H. Noguchi, C.C. Tasan. *Bone-like crack resistance in hierarchical metastable nanolaminate steels*. Science 2017; 355: 1055-1057.

[2]. Z. Zhang, M. Koyama, M.M. Wang, K. Tsuzaki, C.C. Tasan, H. Noguchi. *Effects of lamella size and connectivity on fatigue crack resistance of TRIP-maraging steel.* International Journal of Fatigue 2017, 100: 176-786.

[3]. Z. Zhang, M. Koyama, M.M. Wang, K. Tsuzaki, C.C. Tasan, H. Noguchi. *Microstructural mechanisms of fatigue crack non-propagation in TRIP-maraging steels.* International Journal of Fatigue 2018, 98: 126-136.

[4]. Z. Zhang, M. Koyama, M.M. Wang, C.C. Tasan, H. Noguchi. *Fatigue Resistance of Laminated and Non-laminated TRIP-maraging Steels: Crack Roughness versus Tensile Strength*. Metallurgical and Materials Transactions A

[5]. Z. Zhang, M. Koyama, M.M. Wang, K. Tsuzaki, C.C. Tasan, H. Noguchi. *Three Dimensional Characterization of Roughness-Induced Crack Closure in TRIP-maraging steel.* Materials Science and Engineering A

1.5 References

[1] A. Lasalmonie, J.L. Strudel, Influence of grain size on the mechanical behaviour of some high strength materials, Journal of Materials Science, 21 (1986) 1837-1852.

[2] T. Lee, M. Koyama, K. Tsuzaki, Y.-H. Lee, C.S. Lee, Tensile deformation behavior of Fe–Mn–C TWIP steel with ultrafine elongated grain structure, Materials Letters, 75 (2012) 169-171.

[3] A.J. DeArdo, Multi-phase Microstructures and Their Properties in High Strength Low Carbon Steels, ISIJ International, 35 (1995) 946-954.

[4] M. Sudo, M. Higashi, H. Hori, T. Iwai, S. Kambe, Z. Shibata, Effects of Microstructures on the Mechanical Properties of Multi-phase Sheet Steels, Transactions of the Iron and Steel Institute of Japan, 21 (1981) 820-827.

[5] VF Zackay, ER Parker, D Fahr, R. Busch, The enhancement of ductility in high-strength steels, ASM Trans Quart, 60 (1967) 252-259.

[6] K.-i. Sugimoto, N. Usui, M. Kobayashi, S.-i. Hashimoto, Effects of Volume Fraction and Stability of Retained Austenite on Ductility of TRIP-aided Dual-phase Steels, ISIJ International, 32 (1992) 1311-1318.

[7] S. Thibaud, N. Boudeau, J.C. Gelin, TRIP steel: Plastic behaviour modelling and influence on functional behaviour, Journal of Materials Processing Technology, 177 (2006) 433-438.

[8] D.-Y. Ryoo, N. Kang, C.-Y. Kang, Effect of Ni content on the tensile properties and strain-induced martensite transformation for 304 stainless steel, Materials Science and Engineering: A, 528 (2011) 2277-2281.

[9] K.-i. Sugimoto, K. Nakano, S.-M. Song, T. Kashima, Retained Austenite Characteristics and Stretch-flangeability of High-strength Low-alloy TRIP Type

Bainitic Sheet Steels, ISIJ International, 42 (2002) 450-455.

[10] J.-B. Seol, D. Raabe, P.-P. Choi, Y.-R. Im, C.-G. Park, Atomic scale effects of alloying, partitioning, solute drag and austempering on the mechanical properties of high-carbon bainitic–austenitic TRIP steels, Acta Materialia, 60 (2012) 6183-6199.

[11] B.S. Seong, E.J. Shin, Y.S. Han, C.H. Lee, Y.J. Kim, S.J. Kim, Effect of retained austenite and solute carbon on the mechanical properties in TRIP steels, Physica B: Condensed Matter, 350 (2004) E467-E469.

[12] M. Pozuelo, J.E. Wittig, J.A. Jiménez, G. Frommeyer, Enhanced Mechanical Properties of a Novel High-Nitrogen Cr-Mn-Ni-Si Austenitic Stainless Steel via TWIP/TRIP Effects, Metallurgical and Materials Transactions A, 40 (2009) 1826-1834.

[13] M. Koyama, T. Sawaguchi, K. Tsuzaki, Effects of Si on Tensile Properties Associated with Deformation-Induced ε-Martensitic Transformation in High Mn Austenitic Alloys, MATERIALS TRANSACTIONS, 56 (2015) 819-825.

[14] K.-i. Sugimoto, M. Misu, M. Kobayashi, H. Shirasawa, Effects of Second Phase Morphology on Retained Austenite Morphology and Tensile Properties in a TRIP-aided Dual-phase Steel Sheet, ISIJ International, 33 (1993) 775-782.

[15] X.C. Xiong, B. Chen, M.X. Huang, J.F. Wang, L. Wang, The effect of morphology on the stability of retained austenite in a quenched and partitioned steel, Scripta Materialia, 68 (2013) 321-324.

[16] S. Morito, H. Tanaka, R. Konishi, T. Furuhara, T. Maki, The morphology and crystallography of lath martensite in Fe-C alloys, Acta Materialia, 51 (2003) 1789-1799.

[17] R. Bonadé, P. Spätig, R. Schäublin, M. Victoria, Plastic flow of martensitic model alloys, Materials Science and Engineering: A, 387-389 (2004) 16-21.

[18] S. Morito, H. Yoshida, T. Maki, X. Huang, Effect of block size on the strength of lath martensite in low carbon steels, Materials Science and Engineering: A, 438-440 (2006) 237-240.

[19] D. Raabe, D. Ponge, O. Dmitrieva, B. Sander, Designing ultrahigh strength steels with good ductility by combining transformation induced plasticity and martensite aging, Advanced Engineering Materials, 11 (2009) 547-555.

[20] S.D. Erlach, H. Leitner, M. Bischof, H. Clemens, F. Danoix, D. Lemarchand, I. Siller, Comparison of NiAl precipitation in a medium carbon secondary hardening steel and C-free PH13-8 maraging steel, Materials Science and Engineering: A, 429 (2006) 96-106.

[21] V.K. Vasudevan, S.J. Kim, C.M. Wayman, Precipitation reactions and strengthening behavior in 18 Wt Pct nickel maraging steels, Metallurgical Transactions A, 21 (1990) 2655-2668.

[22] D. Raabe, D. Ponge, O. Dmitrieva, B. Sander, Nanoprecipitate-hardened 1.5 GPa steels with unexpected high ductility, Scripta Materialia, 60 (2009) 1141-1144.

[23] M.M. Wang, C.C. Tasan, D. Ponge, A. Kostka, D. Raabe, Smaller is less stable: Size effects on twinning vs. transformation of reverted austenite in TRIP-maraging steels, Acta Materialia, 79 (2014) 268-281.

[24] G.T. Gray, A.W. Thompson, J.C. Williams, Influence of microstructure on fatigue crack initiation in fully pearlitic steels, Metallurgical Transactions A, 16 (1985) 753-760.

[25] J. Schijve, Fatigue of structures and materials, Springer Science & Business Media,

2001.

[26] S. Suresh, Fatigue of materials, Cambridge university press, 1998.

[27] P. Neumann, Coarse slip model of fatigue, Acta Metallurgica, 17 (1969) 1219-1225.

[28] P.J.E. Forsyth, Fatigue damage and crack growth in aluminium alloys, Acta Metallurgica, 11 (1963) 703-715.

[29] U. Essmann, U. Gösele, H. Mughrabi, A model of extrusions and intrusions in fatigued metals I. Point-defect production and the growth of extrusions, Philosophical Magazine A, 44 (1981) 405-426.

[30] K. Tanaka, T. Mura, A Dislocation Model for Fatigue Crack Initiation, Journal of Applied Mechanics, 48 (1981) 97-103.

[31] A H. Cottrell, D. Hull, Extrusion and intrusion by cyclic slip in copper, Proceedings of the Royal Society of London. Series A. Mathematical and Physical Sciences, 242 (1957) 211.

[32] P.J.E. Forsyth, Exudation of Material from Slip Bands at the Surface of Fatigued Crystals of an Aluminium–Copper Alloy, Nature, 171 (1953) 172.

[33] P. Forsyth, Some further observations on the fatigue process in pure aluminium, J. Inst. Metals, 82 (1954).

[34] J.F. Tavernelli, J.L.F. Coffin, Experimental Support for Generalized Equation Predicting Low Cycle Fatigue, Journal of Basic Engineering, 84 (1962) 533-537.

[35] P. Lukáš, M. Klesnil, J. Polák, High cycle fatigue life of metals, Materials Science and Engineering, 15 (1974) 239-245.

[36] I. Marines, X. Bin, C. Bathias, An understanding of very high cycle fatigue of metals, International Journal of Fatigue, 25 (2003) 1101-1107.

[37] Y. Murakami, T. Nomoto, T. Ueda, Y. Murakami, On the mechanism of fatigue failure in the superlong life regime (N>107 cycles). Part 1: influence of hydrogen trapped by inclusions, Fatigue & Fracture of Engineering Materials & Structures, 23 (2000) 893-902.

[38] G.R. Irwin, Analysis of stresses and strains near the end of a crack traversing a plate, J. appl. Mech., (1957).

[39] P. Paris, F. Erdogan, A critical analysis of crack propagation laws, Journal of basic engineering, 85 (1963) 528-533.

[40] W. Elber, The significance of fatigue crack closure, in: Damage tolerance in aircraft structures, ASTM International (1971) 230-242.

[41] N. Fukumura, T. Suzuki, S. Hamada, K. Tsuzaki, H. Noguchi, Mechanical examination of crack length dependency and material dependency on threshold stress intensity factor range with Dugdale model, Engineering Fracture Mechanics, 135 (2015) 168-186.

[42] B. Li, M. Koyama, S. Hamada, H. Noguchi, Threshold stress intensity factor range of a mechanically-long and microstructually-short crack perpendicular to an interface with plastic mismatch, Engineering Fracture Mechanics, 182 (2017) 287-302.

[43] R.O. Ritchie, S. Suresh, C.M. Moss, Near-Threshold Fatigue Crack Growth in 2 1/4 Cr-1Mo Pressure Vessel Steel in Air and Hydrogen, Journal of Engineering Materials and Technology, 102 (1980) 293-299.

[44] R.O. Ritchie, Mechanisms of fatigue crack propagation in metals, ceramics and composites: Role of crack tip shielding, Materials Science and Engineering: A, 103 (1988) 15-28.

[45] H.R. Mayer, S.E. Stanzl-Tschegg, Y. Sawaki, M. Hühner, E. Hornbogen, INFLUENCE OF TRANSFORMATION-INDUCED CRACK CLOSURE ON SLOW FATIGUE CRACK GROWTH UNDER VARIABLE AMPLITUDE LOADING, Fatigue & Fracture of Engineering Materials & Structures, 18 (1995) 935-948.

[46] S. Suresh, R.O. Ritchie, A geometric model for fatigue crack closure induced by fracture surface roughness, Metallurgical Transactions A, 13 (1982) 1627-1631.

[47] S. Suresh, G.F. Zamiski, D.R.O. Ritchie, Oxide-Induced Crack Closure: An Explanation for Near-Threshold Corrosion Fatigue Crack Growth Behavior, Metallurgical and Materials Transactions A, 12 (1981) 1435-1443.

[48] D. Benoit, R. Namdar-Irani, R. Tixier, Oxidation of fatigue fracture surfaces at low crack growth rates, Materials Science and Engineering, 45 (1980) 1-7.

[49] X. Cheng, R. Petrov, L. Zhao, M. Janssen, Fatigue crack growth in TRIP steel under positive R-ratios, Engineering Fracture Mechanics, 75 (2008) 739-749.

[50] R. Ritchie, S. Suresh, Some considerations on fatigue crack closure at near-threshold stress intensities due to fracture surface morphology, Metallurgical Transactions A, 13 (1982) 937-940.

[51] R. Pippan, G. Strobl, H. Kreuzer, C. Motz, Asymmetric crack wake plasticity – a reason for roughness induced crack closure, Acta Materialia, 52 (2004) 4493-4502.

[52] G.T. Gray, J.C. Williams, A.W. Thompson, Roughness-Induced Crack Closure: An Explanation for Microstructurally Sensitive Fatigue Crack Growth, Metallurgical Transactions A, 14 (1983) 421-433.

[53] D.L. Davidson, J. Lankford, The effect of water vapor on fatigue crack tip stress and strain range distribution and the energy required for crack propagation in low-

carbon steel, International Journal of Fracture, 17 (1981) 257-275.

[54] M.M. Wang, C.C. Tasan, D. Ponge, A.C. Dippel, D. Raabe, Nanolaminate transformation-induced plasticity–twinning-induced plasticity steel with dynamic strain partitioning and enhanced damage resistance, Acta Materialia, 85 (2015) 216-228.

[55] T. Fujisawa, S. Hamada, N. Koga, D. Sasaki, T. Tsuchiyama, N. Nakada, K. Takashima, M. Ueda, H. Noguchi, Proposal for an engineering definition of a fatigue crack initiation unit for evaluating the fatigue limit on the basis of crystallographic analysis of pearlitic steel, International Journal of Fracture, 185 (2014) 17-29.

[56] M. Abareshi, E. Emadoddin, Effect of retained austenite characteristics on fatigue behavior and tensile properties of transformation induced plasticity steel, Materials & Design, 32 (2011) 5099-5105.

1.6 Tables and figures

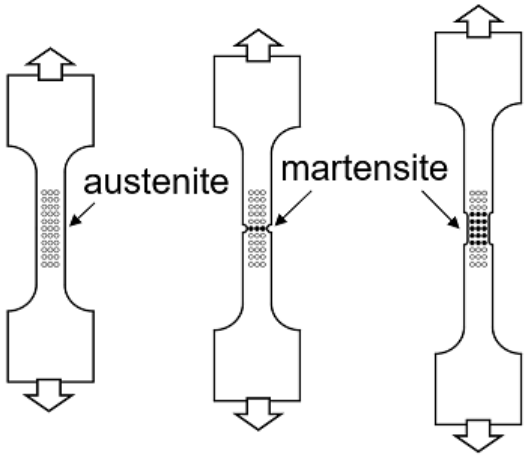

Fig. 1.1. Schematic of transformation-induced plasticity [8].

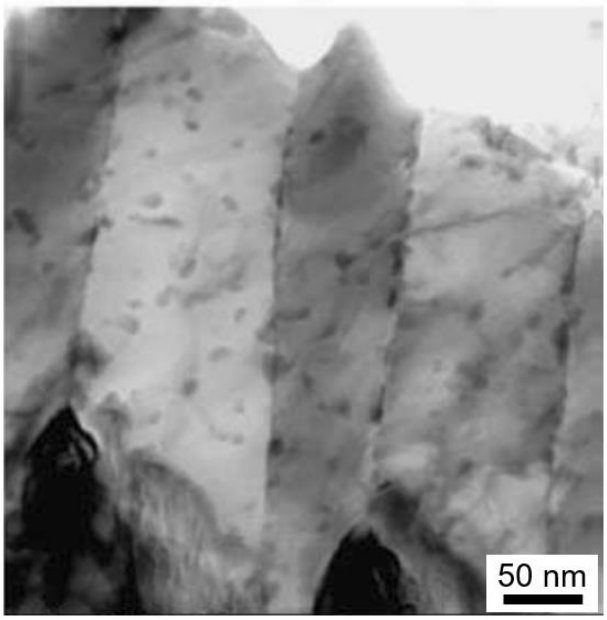

Fig. 1.2. Nanosized intermetallic compounds exist within martensite matrix [16].

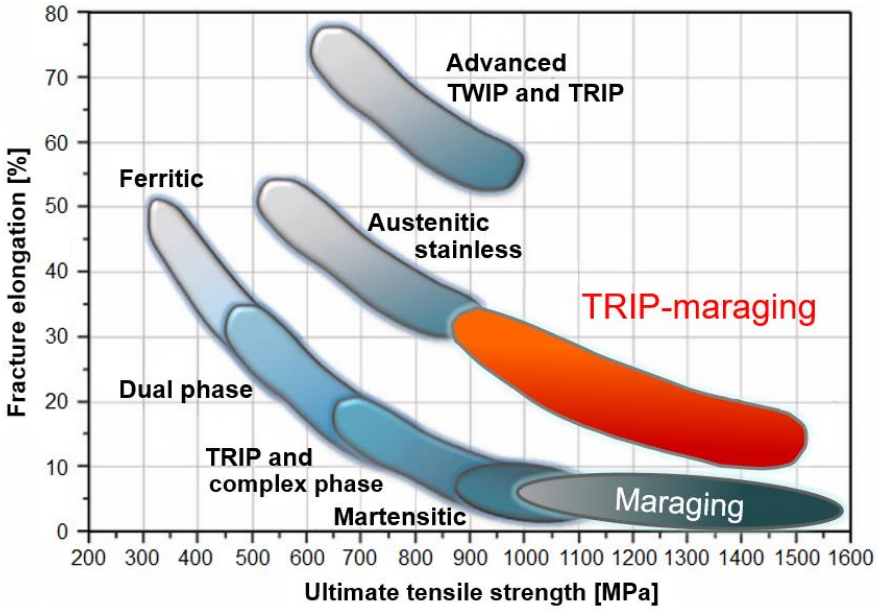

Fig. 1.3. Overview of the strength-ductility profiles of different types of steels [16, 19].

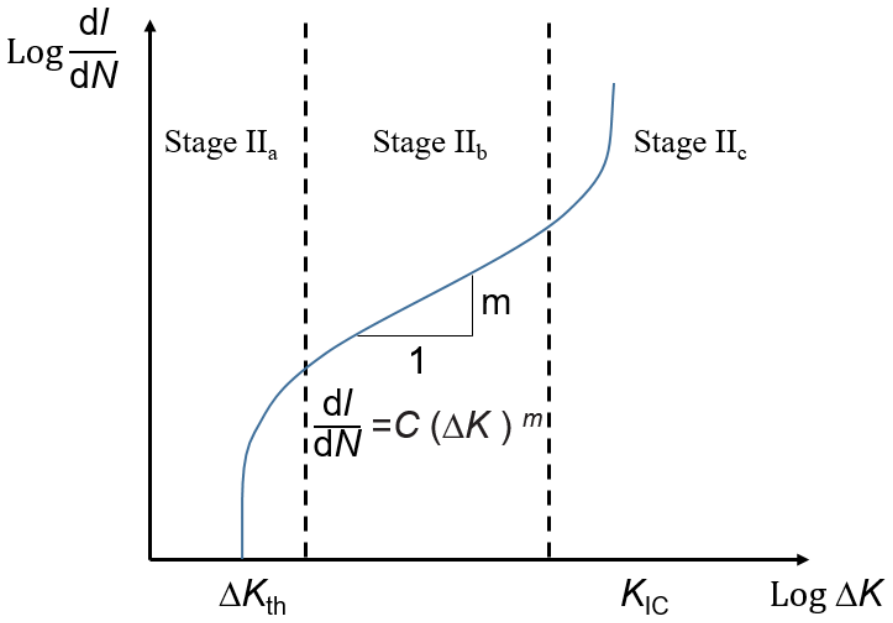

Fig. 1.4. Fatigue crack growth behavior.

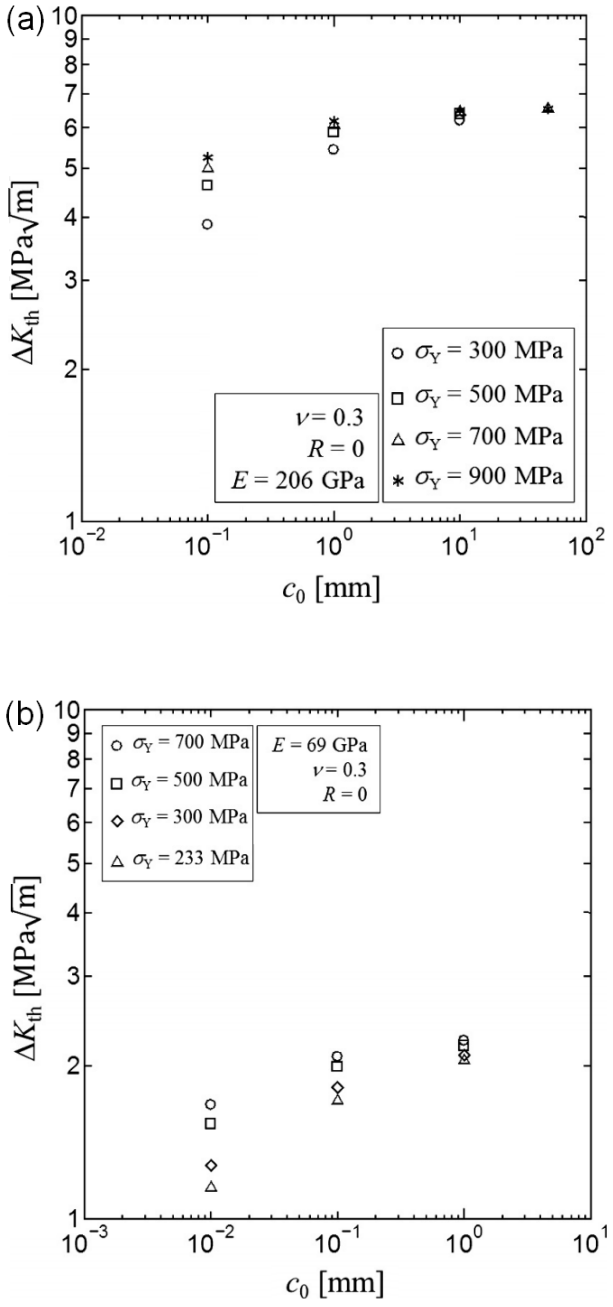

Fig. 1.5. Influence of half length of initial crack (c_0) and yield strength (σ_Y) on ΔK_{th} for (a) steels and (b) aluminum alloys [41].

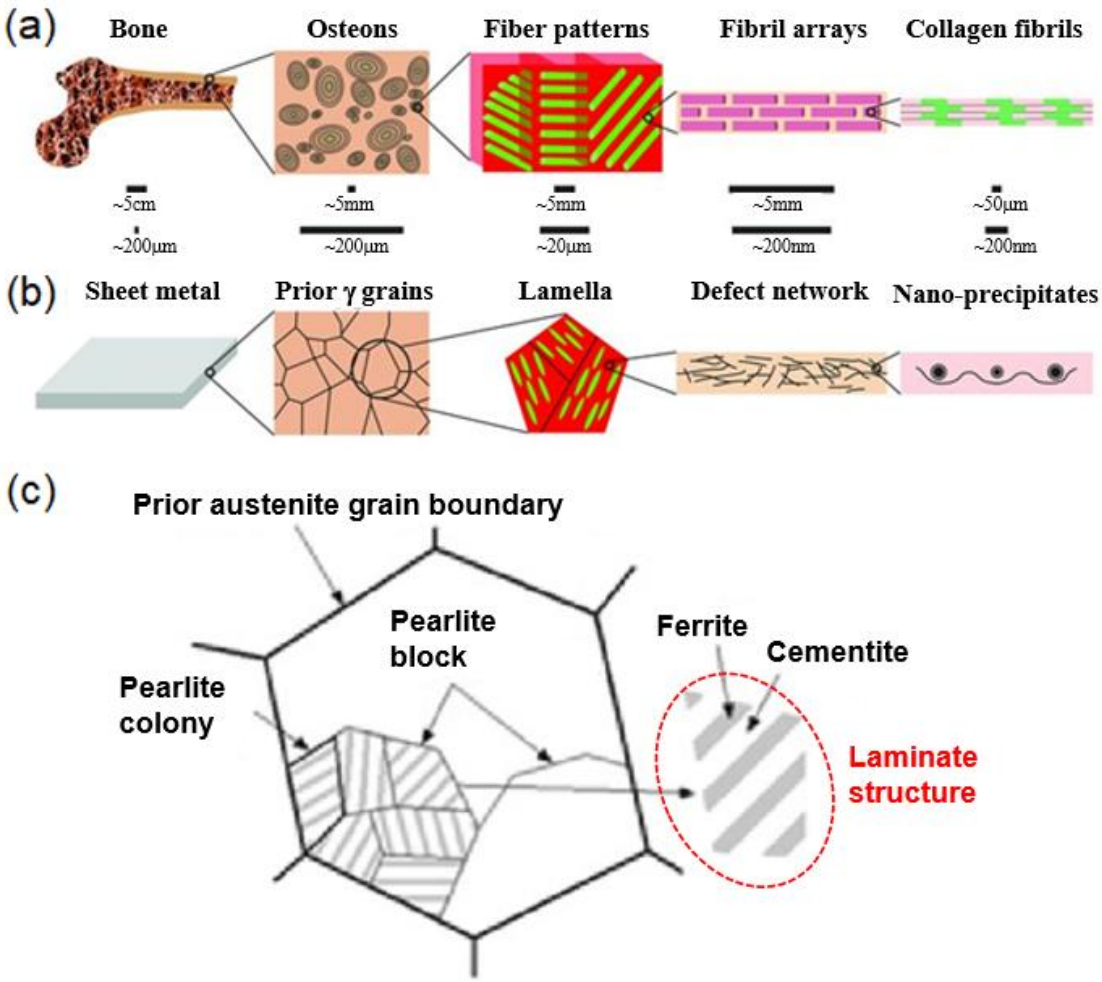

Fig. 1.6. Schematic of microstructure of (a) bone, (b) TRIP-maraging steels and (c) pearlitic steels [55].

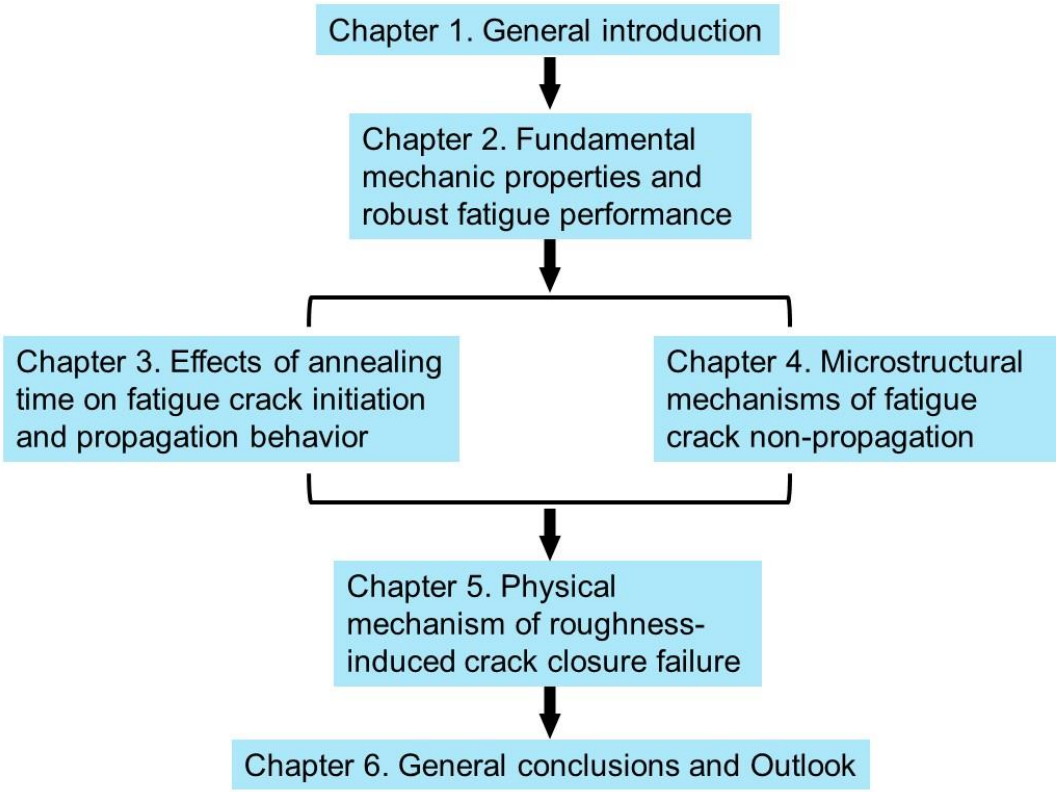

Fig. 1.7. Structure for present work.

CHAPTER 2. Fundamental mechanic properties and robust fatigue performance

2.1 Introduction

The substructure of bone is hierarchical fine laminate, which leads to superior crack resistance by simultaneous activation of multiple micromechanisms that resist crack propagation [1, 2]. It is hypothesized that (i) a similar response can be transferred to metals by designing a hierarchical and fine laminated multiphase microstructure to benefit from interface structure [3, 4] and distribution [5, 6] effects, and (ii) this resistance can be further enhanced by triggering the local phase transformation mechanisms from the metastable microstructure [7, 8]. The overall goal is the simultaneous activation of roughness-induced crack closure (RICC) and transformation-induced crack closure (TICC) mechanisms. TRIP-maraging steels which are explored to investigate the validity of above hypothesis, have an intrinsic hierarchical structure that is comparable to that of bone and composed of laminated martensite and metastable austenite phases. Thus, they possess the key combination of three characteristics—namely, multiple phases, metastability, and fine laminate.

2.2 Materials

The ferrite-martensite Fe–0.9C–1.7Mn–0.24Si (wt.%) dual-phase (DP) steel (Fig. 2.1a) was produced by intercritical annealing at 1023 K and follow-up quenching to

room temperature. The ferrite-cementite Fe–0.9C–0.9Mn–0.4Si (wt.%) pearlitic steel (Fig. 2.1b) was heat treated at 1200 ℃ for 30 min, followed by 650 ℃ for 3 min, and quenched in water. The pearlite block size and lamellar spacing were approximately 75 μm and 0.15 μm, respectively. The multi-phase TRIP steel is quoted from [9, 10] (Fig. 2.1c). The new steel with metastable multiphase fine laminate called TRIP-maraging steel (Fig. 2.1d) has a Fe-9Mn-3Ni-1.4Al-0.01C (wt.%) composition. The steel was cast and hot rolled at 1373 K. Afterwards, it was homogenized at 1373 K for 1 hour and subsequently water-quenched. The as-quenched microstructure was fully lath martensite. For obtaining reversed austenite with different volume fractions, the as-quenched martensite bulk specimens were respectively annealed at 873 K for 1 and for 8 hours, which causes a decline in strength with annealing time, instead elongation increases as shown in Fig. 2.2 [11, 12], the steels annealed for 1 h and 8 h were named as 1 h-steel and 8 h-steel, respectively. This treatment produced a martensitic matrix with austenite islands at various martensitic boundaries. The latter can be classified into two groups based on their size: those that range between 0.1 - 0.3 μm^2 and the others that are between 0.3 - 4.0 μm^2 [11]. Figure 2.3 shows the microstructures of 1h- and 8h-steels before fatigue tests. Both steels present a hierarchical laminated microstructure containing martensite packets/blocks/laths within a prior austenite grain boundary [11] (Fig. 2.3 a_3 and b_3). Another TRIP-maraging steel is featured by non-fine-laminate microstructure had a chemical composition of Fe-9Mn-3Ni-1.4Al-0.01C (wt. %). The steel was cast and hot rolled at 1373 K. Afterwards, it was homogenized at 1373 K for 1 hour and subsequently water-quenched. The as-quenched microstructure was fully lath martensite. The as-quenched steel plate was cold rolled by 70% thickness reduction. Partial reversion of cold-rolled α′-martensite to austenite was carried out at 873 K for 1 h [13].

2.3 Method

Fatigue properties were evaluated by rotary bending fatigue testing. Two types of geometries were used. For the cylinder bar as given in Fig. 2.4, the tests were carried out at a stress ratio of −1 with 50 Hz and room temperature (≈ 298 K). In the same material, the different geometry of plate was used as shown in Fig. 2.5a, to clarify the high importance of the fine laminate microstructure morphology for the improved properties. Since the reference material with a non-laminated metastable multiphase microstructure requires cold rolling, the design for specimen geometry is always a plate. Therefore, the fatigue test plate specimen was fixed on the round bar jig as shown in Fig. 2.5b, and fatigue tests were performed on an Ono-type rotating bending fatigue testing machine at room temperature with a stress ratio of −1 and a frequency of 30 Hz. To reduce the effect of temperature increase during testing, the specimens were cooled by an electric fan. The fatigue cracks were observed by optical microscopy using the replica technique [14]. Prior to testing, the specimens were mechanically polished with emery papers and colloidal silica. The polished specimens were chemically etched with 3% nital to reveal the microstructures. In terms of instrumentation, we used an Ono-type rotary bending fatigue test machine (specimens were clamped on both sides.) [15]. After fatigue testing, sample surface was prepared following standard metallography procedures. Samples were prepared by grinding, polishing in diamond suspension and final polishing in colloidal silica suspension. The last step ensures obtaining a deformation-free surface.

Microstructures were characterized by scanning electron microscopy based EBSD at 15 kV at a beam step size of 80 nm and ECCI at 20 kV. Samples for the SEM analyses were prepared by grinding, polishing in diamond suspension and final polishing in colloidal silica suspension.

2.4 Results and discussion

Figure 2.6 reveals that TRIP-maraging steels have robust fatigue performance, compared to other conventional steels (Fig. 2.1a to c). Ferrite-martensite dual-phase (DP) steel (Fig. 2.1a) shows relatively low fatigue limits (Fig. 2.6) [16, 17]. This is attributed to the absence of effective crack closure mechanisms that could hamper crack growth and the high mechanical contrast between the soft ferrite phase and the hard martensite phase [18]. In fact, efforts for developing better design strategies against crack propagation [19] were originally motivated by the need to render such high-strength and -formability multiphase steels more fatigue-resistant. On the other hand, ferrite-cementite pearlitic steel (Fig. 2.1b) shows improved fatigue resistance in comparison with the DP steel (Fig. 2.6). In pearlitic steel, the multiphase fine laminate microstructure morphology, which is different from the globular structure of DP steel, deflects fatigue cracks constantly during growth, thereby introducing a friction stress acting on the crack surface and decelerating the fatigue crack opening and growth process [20, 21]. Thus, this improvement is due to the RICC mechanism, which is affected by the morphological characteristics of the cementite network, such as the interlamellar spacing [20] and lamellar alignment [22]. The fatigue limit of pearlitic steel is low, because the RICC mechanism does not work efficiently for the deceleration of small cracks [23].

2.4.1 Transformation-induced crack closure

Metastable multiphase TRIP steel (Fig. 2.1c) also shows an improved fatigue resistance compared with DP steel (Fig. 2.6). The formation of compressive residual stress fields, arising from the volume-expanding transformation from face-centered

cubic γ-austenite to body-centered cubic (or body-centered tetragonal) α′-martensite at the crack tip [21, 24, 25], suppresses crack initiation and growth [26]. Thus, the higher strength-ductility balance for the multiphase TRIP steel is attributed to the TICC mechanism. However, similar to the RICC effect on fatigue life discussed above, the effects of TRIP and TICC are stress amplitude-dependent. Their contributions are less effective when the stress amplitude is high, because an increasing stress amplitude leads to larger plastic strain, which in turn results in a decrease in the fraction of metastable γ-austenite via transformation [12] during the early loading cycles. The improvements in the fatigue performance of TRIP-maraging steel with respect to that of these conventional steels provide an indirect confirmation of the simultaneous introduction of the RICC and TICC (and TRIP) effects. Another indirect corroboration was given when TRIP-maraging steel has a non-laminated microstructure, which indeed led to inferior fatigue properties (Fig. 2.7).

Figure 2.8 shows replica images for fatigue cracks developing at the fatigue limit. Crack initiation (Fig. 2.8a) is delayed until around 10^7 cycles. The delayed fatigue crack initiation and the hampering of its propagation are key factors for improving the fatigue limit. Crack non-propagation takes place in both directions (parallel and perpendicular to lath alignment) when the cracks reach prior austenite boundaries (Fig. 2.8c), which are the interfaces decorated by austenite films in this steel (Fig. 2.1d) [12]. These boundaries undergo substantial local hardening and residual compressive stress induced by the transformation of the austenite films (i.e., TICC effect) in the vicinity of the fatigue crack (Fig. 2.8d).

2.4.2 Roughness-induced crack closure

In contrast, at high stress amplitudes, fatigue cracks form at the early stages of the test and then continuously propagate until macroscopic failure. However, the fatigue crack propagation path is deflected when propagating across or along different grain boundaries or the lamellae (Fig. 2.9a). The crack surface morphology exhibits many small branches, indicated by the yellow arrows in Fig. 2.9b. The microroughness on the crack surface, enabled by the laminate's hierarchical microstructure morphology, enhances the RICC effect. The obvious similarity of the observed fracture process to the fracture of bone [1], despite the significant difference in the constitution of these two materials, provides another demonstration of the success of this microstructure characterized by fine laminate and metastable phase (Fig. 2.9c and d).

2.5 Section conclusion

We conceived and demonstrated the effectiveness of a metastable multiphase fine laminate microstructure concept for creating materials with exceptional fatigue resistance. This is achieved by simultaneously enabling transformation-induced and roughness-induced crack closure mechanisms. The demonstrated superior low-cycle fatigue life and high fatigue limit constitute essential progress for steels, and we expect similar improvements in material properties for any alloys that can be designed with similar microstructures. Thus, this strategy has potential to improve the safety of advanced structures and components that experience cyclic loads. For the different fatigue life in TRIP-maraging steels, the austenite morphology probable is influence factor that will be discuss in the following chapter.

2.6 References

[1] H. Peterlik, P. Roschger, K. Klaushofer, P. Fratzl, From brittle to ductile fracture of bone, Nature Materials 5 (2005) 52.

[2] R.K. Nalla, J.H. Kinney, R.O. Ritchie, Mechanistic fracture criteria for the failure of human cortical bone, Nature Materials 2 (2003) 164.

[3] L.L. Li, Z.J. Zhang, P. Zhang, Z.G. Wang, Z.F. Zhang, Controllable fatigue cracking mechanisms of copper bicrystals with a coherent twin boundary, Nature Communications 5 (2014) 3536.

[4] L.L. Li, P. Zhang, Z.J. Zhang, Z.F. Zhang, Intrinsically higher fatigue cracking resistance of the penetrable and movable incoherent twin boundary, Scientific Reports 4 (2014) 3744.

[5] Z. Ma, J. Liu, G. Wang, H. Wang, Y. Wei, H. Gao, Strength gradient enhances fatigue resistance of steels, Scientific Reports 6 (2016) 22156.

[6] Y. Kimura, T. Inoue, F. Yin, K. Tsuzaki, Inverse Temperature Dependence of Toughness in an Ultrafine Grain-Structure Steel, Science 320(5879) (2008) 1057.

[7] Y.-B. Ju, M. Koyama, T. Sawaguchi, K. Tsuzaki, H. Noguchi, In situ microscopic observations of low-cycle fatigue-crack propagation in high-Mn austenitic alloys with deformation-induced ε-martensitic transformation, Acta Materialia 112 (2016) 326-336.

[8] B. Gludovatz, A. Hohenwarter, D. Catoor, E.H. Chang, E.P. George, R.O. Ritchie, A fracture-resistant high-entropy alloy for cryogenic applications, Science 345(6201) (2014) 1153.

[9] E. Girault, A. Mertens, P. Jacques, Y. Houbaert, B. Verlinden, J. Van Humbeeck,

Comparison of the effects of silicon and aluminium on the tensile behaviour of multiphase TRIP-assisted steels, Scripta materialia, 44 (2001) 885-892.

[10] M. Abareshi, E. Emadoddin, Effect of retained austenite characteristics on fatigue behavior and tensile properties of transformation induced plasticity steel, Materials & Design, 32 (2011) 5099-5105.

[11] M.M. Wang, C.C. Tasan, D. Ponge, A. Kostka, D. Raabe, Smaller is less stable: Size effects on twinning vs. transformation of reverted austenite in TRIP-maraging steels, Acta Materialia 79 (2014) 268-281.

[12] M.M. Wang, C.C. Tasan, D. Ponge, A.C. Dippel, D. Raabe, Nanolaminate transformation-induced plasticity–twinning-induced plasticity steel with dynamic strain partitioning and enhanced damage resistance, Acta Materialia 85 (2015) 216-228.

[13] M.M. Wang, C.C. Tasan, D. Ponge, D. Raabe, Spectral TRIP enables ductile 1.1 GPa martensite, Acta Materialia 111 (2016) 262-272.

[14] S. Hamada, T. Fujisawa, M. Koyama, N. Koga, N. Nakada, T. Tsuchiyama, M. Ueda, H. Noguchi, Strain mapping with high spatial resolution across a wide observation range by digital image correlation on plastic replicas, Materials Characterization 98 (2014) 140-146.

[15] M. Ohnami, Fracture and society, IOS Press1992.

[16] J.A. Wasynczuk, R.O. Ritchie, G. Thomas, Effects of microstructure on fatigue crack growth in duplex ferrite-martensite steels, Materials Science and Engineering 62(1) (1984) 79-92.

[17] Z.G. Hu, P. Zhu, J. Meng, Fatigue properties of transformation-induced plasticity and dual-phase steels for auto-body lightweight: Experiment, modeling and

application, Materials & Design 31(6) (2010) 2884-2890.

[18] X.-L. Cai, J. Feng, W.S. Owen, The dependence of some tensile and fatigue properties of a dual-phase steel on its microstructure, Metallurgical Transactions A 16(8) (1985) 1405-1415.

[19] S. Suresh, R.O. Ritchie, Propagation of short fatigue cracks, International Metals Reviews 29(1) (1984) 445-475.

[20] G.T. Gray, J.C. Williams, A.W. Thompson, Roughness-Induced Crack Closure: An Explanation for Microstructurally Sensitive Fatigue Crack Growth, Metallurgical Transactions A 14(2) (1983) 421-433.

[21] R.O. Ritchie, Mechanisms of fatigue crack propagation in metals, ceramics and composites: Role of crack tip shielding, Materials Science and Engineering: A 103(1) (1988) 15-28.

[22] I. Verpoest, E. Aernoudt, A. Deruyttere, M. De Bondt, The fatigue threshold, surface condition and fatigue limit of steel wire, International Journal of Fatigue 7(4) (1985) 199-214.

[23] M.A. Daeubler, A.W. Thompson, I.M. Bernstein, Influence of microstructure on fatigue behavior and surface fatigue crack growth of fully pearlitic steels, Metallurgical Transactions A 21(3) (1990) 925-933.

[24] H. Mayer, S. Stanzl‐Tschegg, Y. Sawaki, M. Hühner, E. Hornbogen, Influence of transformation-induced crack closure on slow fatigue crack growth under variable amplitude loading, Fatigue & Fracture of Engineering Materials & Structures 18(9) (1995) 935-948.

[25] Z. Mei, J.W. Morris, Analysis of transformation-induced crack closure, Engineering Fracture Mechanics 39(3) (1991) 569-573.

[26] A.G. Pineau, R.M. Pelloux, Influence of strain-induced martensitic transformations on fatigue crack growth rates in stainless steels, Metallurgical Transactions 5(5) (1974) 1103-1112.

[27] A. Aran, H. Türker, The effect of martensite content on the fatigue behaviour of a ferritic-martensitic steel, Journal of Materials Science Letters, 9 (1990) 1407-1408.

[28] G.T. Gray, A.W. Thompson, J.C. Williams, Influence of microstructure on fatigue crack initiation in fully pearlitic steels, Metallurgical Transactions A, 16 (1985) 753-760.

[29] T. Fujisawa, S. Hamada, N. Koga, D. Sasaki, T. Tsuchiyama, N. Nakada, K. Takashima, M. Ueda, H. Noguchi, Proposal for an engineering definition of a fatigue crack initiation unit for evaluating the fatigue limit on the basis of crystallographic analysis of pearlitic steel, International Journal of Fracture, 185 (2014) 17-29.

2.7 Tables and figures

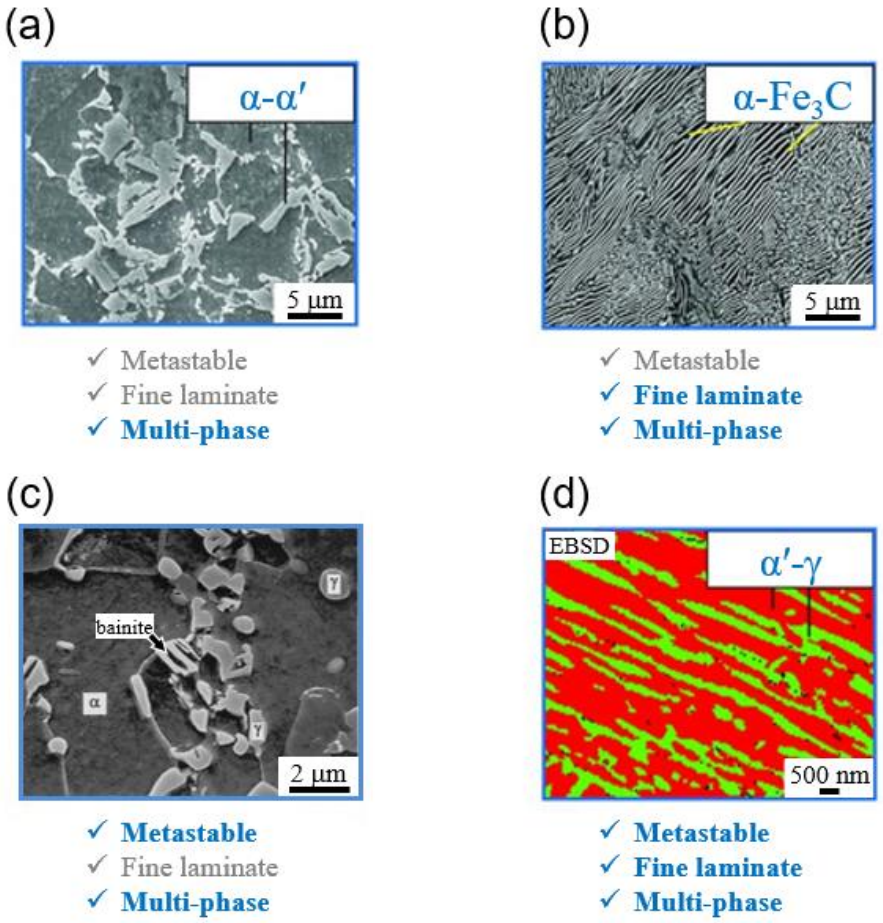

Fig. 2.1. Microstructure of (a) dual-phase steels, (b) pearlitic steels, (c) TRIP steels and (c) TRIP-maraging steels.

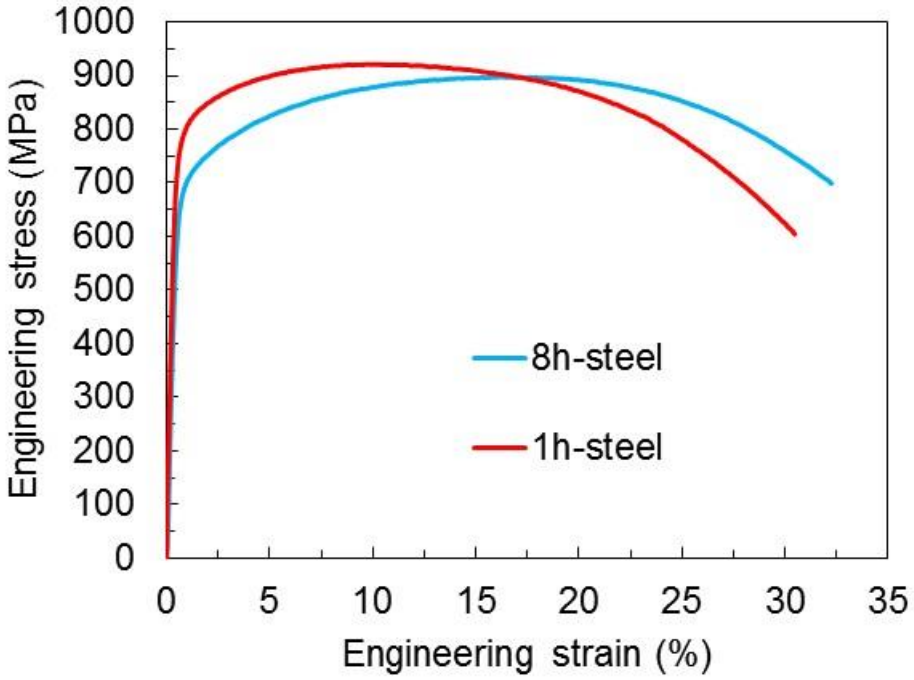

Fig. 2.2. Engineering stress-strain curves for TRIP-maraging steels annealed for 1 h and 8 h, respectively. The tensile tests were carried out at an initial strain rate of $10^{-3}s^{-1}$.

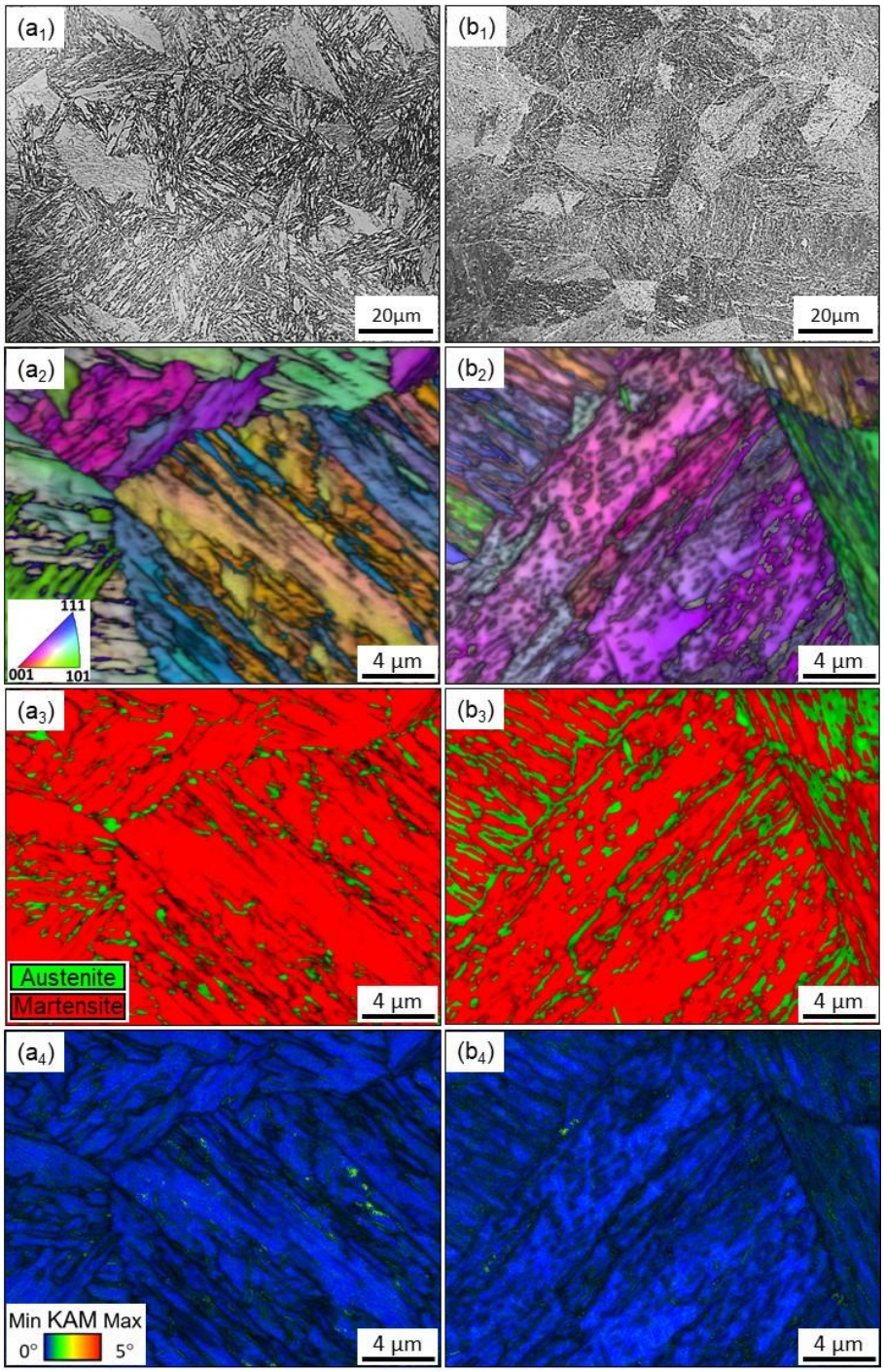

Fig. 2.3. Microstructure of TRIP-maraging steels after annealing at 873 K for (a) 1 h and (b) 8 h. (a_1, b_1): Optical microscopic images of replicas. (a_2, b_2): EBSD inverse pole (IPF) maps, (a_3, b_3) phase maps and (a_4, b_4) Kernel average misorientation (KAM) maps with IQ contrast.

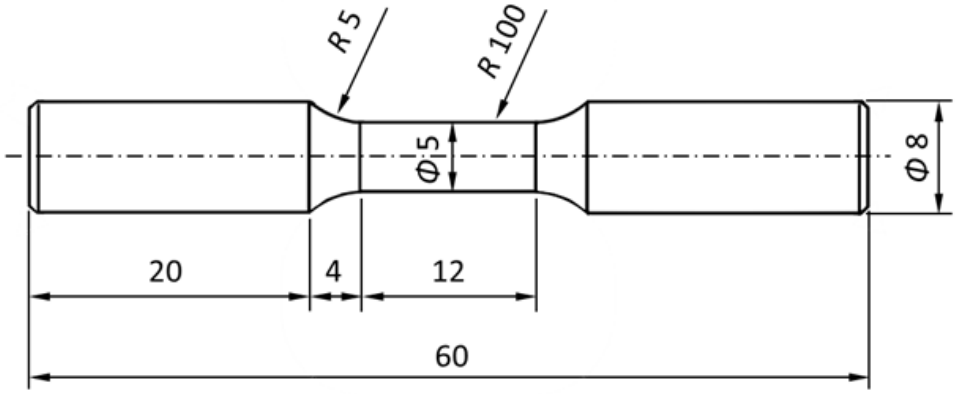

Fig. 2.4. Specimen geometry used for rotary bending fatigue tests (unit: mm)

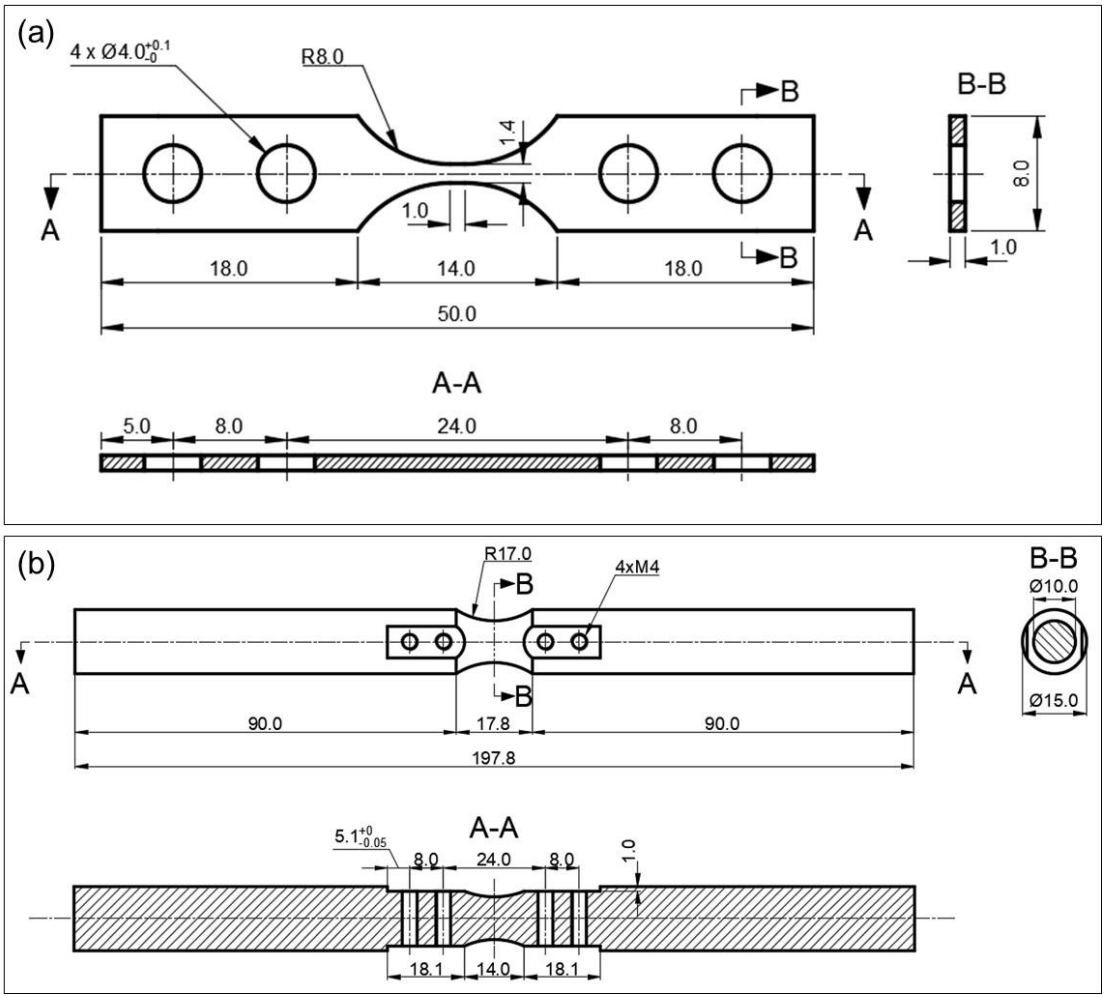

Fig. 2.5. (a) A schematic sketch of the plate specimen geometry used for the fatigue tests (unit: mm). A jig shown in (b) was used to test samples taken from the plate specimens by rotating bending fatigue testing. The plate specimen was fastened on the jig by screws.

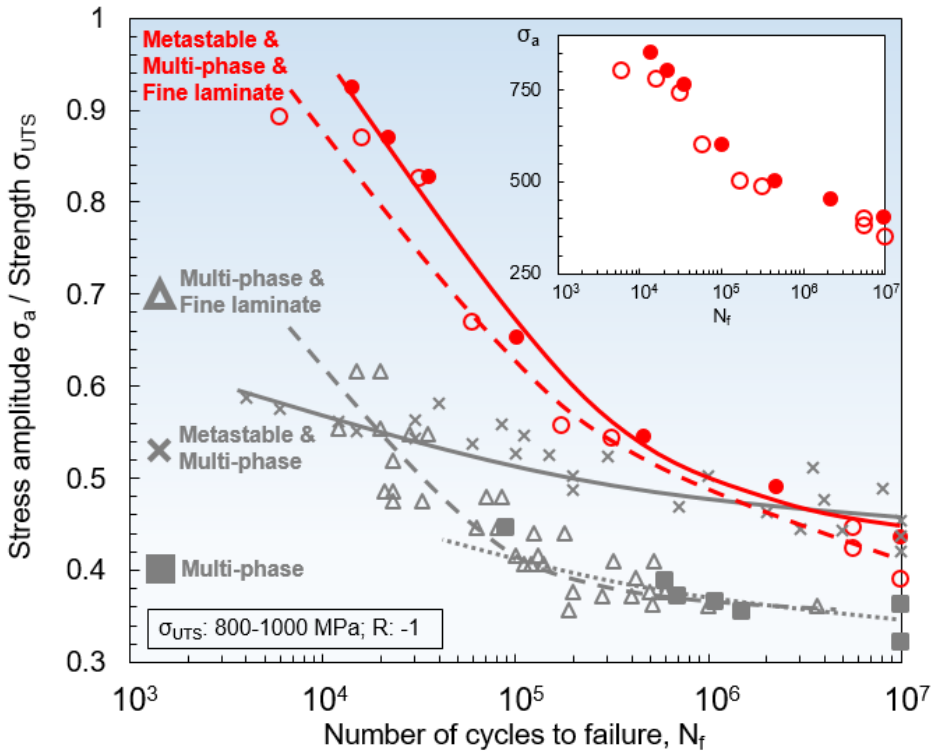

Fig. 2.6. Number of cycles to failure, plotted against stress amplitude. Results were obtained from the cylindrical bar specimens. The solid and open red circles indicate the results for the steels aged at 873 K for 1 and 8 hours, respectively. The conventional steels indicated by grey colour [10, 27-29].

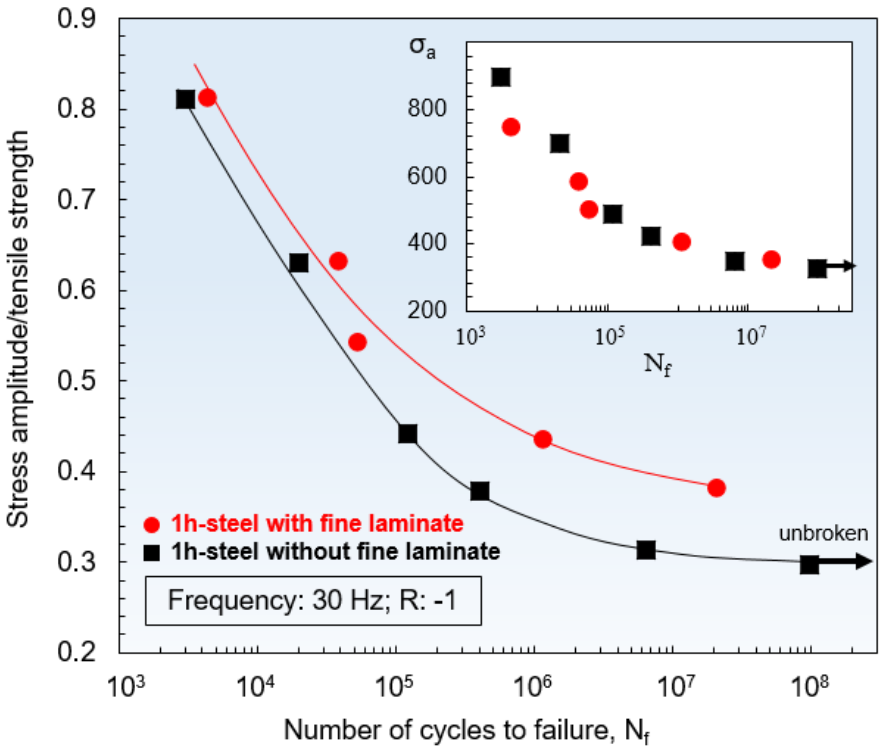

Fig. 2.7 Number of cycles to failure, plotted against stress amplitude. Results were obtained from the same plate specimen geometry and testing method.

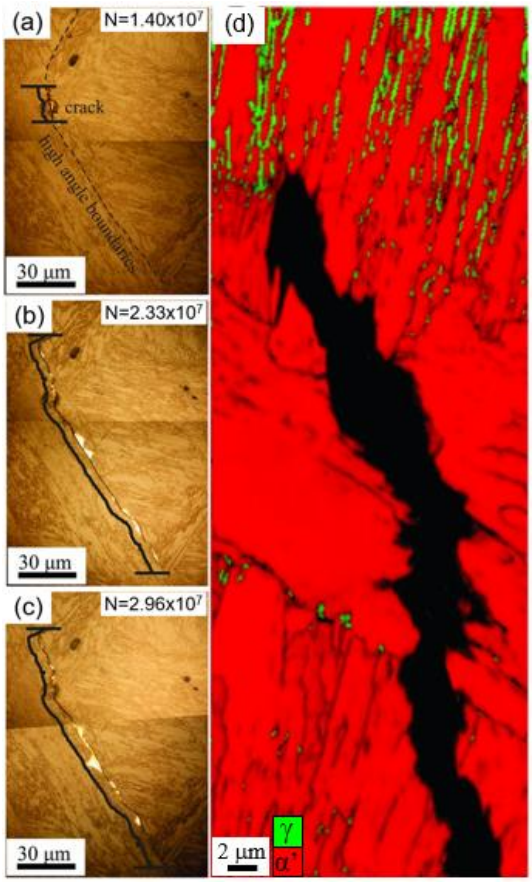

Fig. 2.8. TRIP-maraging steel annealed for 1 hour at the fatigue limit of 400 MPa. (a-c) Optical images; (d) EBSD phase map with quality image.

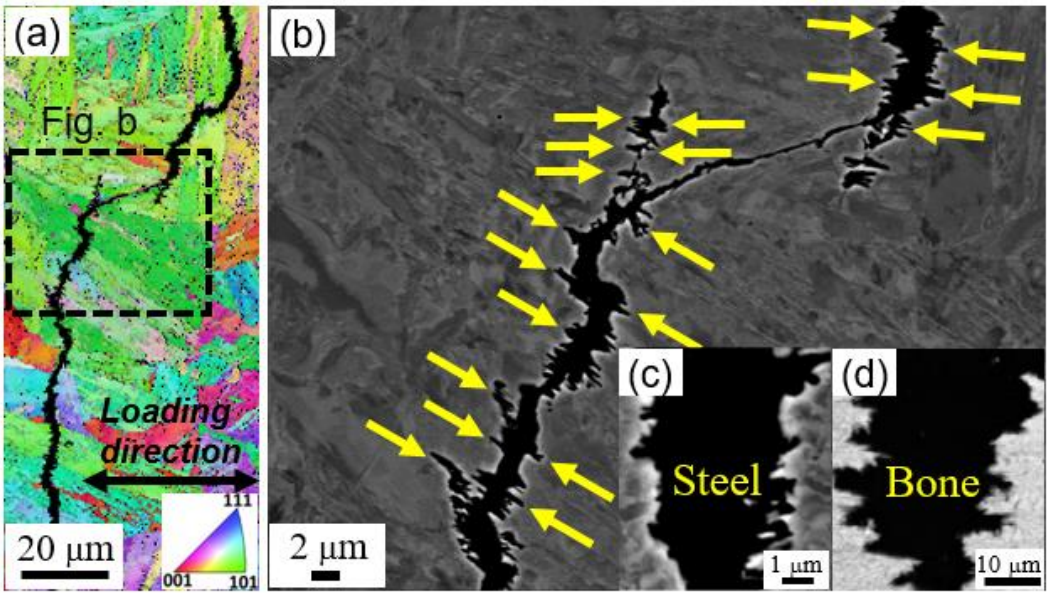

Fig. 2.9. Hierarchical roughness on the fatigue crack in the TRIP-maraging steel annealed for 1 hour at 760 MPa with fatigue life 3.6×10^4 cycles.

CHAPTER 3. Effect of annealing time on fatigue crack initiation and propagation behavior

3.1 Introduction

Chapter 2 showed that laminated TRIP-maraging steels are characterized by high fatigue limit and high fatigue life, because of the combined effect of transformation-induced crack closure (TICC) and roughness-induced crack closure (RICC) [1]. Therefore, a thorough understanding of the microstructural factors that affect the fatigue resistance is crucial for the practical application of TRIP-maraging steel. The occurrence of TICC depends on the austenite characteristics such as phase stability and fraction. The effectiveness of RICC depends mainly on the retained austenite morphology, e.g. lamellar spacing. The austenite fraction and morphology of TRIP-maraging steel can be adjusted by controlling annealing conditions for austenitization, i.e. both the austenite grain size and connectivity in lamella increase with annealing time.

In fact, the annealing time has been controlled to change an elongation-strength balance in TRIP-maraging steels [2], but the microstructure variation has not been considered for fatigue resistance. Hence, annealing time influence on the fatigue resistance of TRIP-maraging steel is potentially important to uncover several aspects of the austenite fraction and distribution. Specifically, it is expected that an increase in austenite fraction may enhance TICC. In addition, the austenite may promote RICC.

Hence, fatigue behavior can be optimized through controlling annealing time. In order to propose a guideline for optimizing TRIP-maraging steel microstructure, the austenite characteristics are correlated with fatigue behavior.

3.2 Materials and investigation method

In this work, the effect of austenite morphology on fatigue crack behavior is analyzed by using experimental results of chapter 2. Generally, in TRIP-aided multi-phase steels, higher amounts of retained austenite can lead to higher fatigue crack resistance, because of the deformation-induced martensitic transformation with a volumetric expansion at the crack tip, i.e. TICC [3]. However, the present TRIP-maraging steel with higher austenite fraction, i.e. 8h-steel, shows lower fatigue life, irrespective of the stress amplitude.

Microstructure characterizations were carried out using scanning electron microscopy (SEM)-based analyses: electron backscatter diffraction (EBSD) pattern measurements and secondary electron imaging. To measure the retained austenite distribution and reveal small fatigue crack propagation path, EBSD measurements were conducted at an accelerating voltage of 15 kV with a beam step size of 0.05 μm. To observe the characteristics of the fatigue fracture surface, the SEM images were obtained at an accelerating voltage of 15 kV.

3.3 Results

3.3.1 Crack initiation and propagation in high cycle fatigue

Figures 3.1(a) and (b) show the fatigue crack lengths and crack growth rate plotted against the number of cycles at 500 MPa in 1h-steel and at 488 MPa in 8h-steel. The stress amplitudes were selected to maintain the same ratio (0.54) of stress amplitude to

tensile strength for two steels. Even when comparing the results normalized by the tensile strength, the 8h-steel shows faster crack growth than that of the 1h-steel, particularly at small fatigue crack lengths (Fig. 3.1(a) and its magnified image at lower number of cycles regime in Fig. 3.1(b)). The corresponding crack growth rates are shown in Fig. 3.1(c). The diagrams of fatigue crack growth rate against crack length are plotted as shown in Fig. 3.1(d) and (e).

Figure 3.2(a) shows that the main fatigue crack of 1h-steel at 500 MPa is initiated from a defect. As can be seen in Fig. 3.2(b), the defect is located in the interior of a prior austenite grain. At the left tip of the crack, the crack growth was decelerated because of the presence of lamellae that are aligned diagonally as shown in Fig. 3.2(c). In contrast, at the other crack tip, it continuously propagated as shown in and Fig. 3.2(d). With increasing number of cycles, the fatigue crack propagated along the austenite/martensite lamella, as shown in Fig. 3.2(e). Because of the preferential fatigue crack propagation along the lamellar structure, the main crack propagation path is remarkably tortuous. Figure 3.2(f) indicates that the fatigue crack propagates not only along the lamella, but also across the lamellar structure. The final stage of fatigue growth at 4.6×10^5 cycles, when the fatigue crack propagates across the lamella, is accompanied with frequent crack branching, as indicated by the white dashed arrows in Fig. 3.2(g). For further crystallographic analysis, the EBSD results around a small sub-crack in the 1h-steel fatigued at 500 MPa are shown in Fig. 3.3. According to the normal direction (ND)-inverse pole figure (IPF) and IQ maps shown in Fig. 3.3(a), the fatigue crack growth path occurs both in the grain interior and the grain boundaries. Specifically, the crack tips, indicated by the yellow arrows, are present in the grain interior, while the central part of the crack is situated along grain boundaries. Since there is not a significant

amount of austenite around the crack, probably due to martensitic transformation in this region as shown in Fig. 3.3(b), detailed correlation between the lamellar microstructure and the crack growth path could not be clarified from this result.

Figures 3.4(a) and (b) show the main fatigue crack growth of 8h-steel at 488 MPa. Since the two cracks coalesce with each other eventually to form the main crack, both small fatigue crack growth behaviors before coalescence are crucial. Both fatigue cracks were initiated from grain boundaries, as highlighted by black arrows in Figs. 3.4(c) and (d). Corresponding to the crack growth rates as shown in Fig. 3.1(e), the growth of the right side of the crack was hindered by grain boundaries, the other side propagated along the boundary as shown in Figs. 3.4(d) and (e). The initiated cracks continuously propagated along the grain boundary, which acted as the crack initiation site. Then, the fatigue cracks propagated across or along the lamellar structure, as shown in Figs. 3.4(f) and (g), the black arrows indicate crack branching. The branched cracks stopped at the grain boundaries or grain interior, with the lamella aligned near-perpendicularly to the propagation direction. Finally, the two cracks coalesced with each other (Fig. 3.4(b)), which caused the abrupt increase in growth rate shown in Fig. 3.1(c). The fatigue crack propagation path of 8h-steel was similar as that of 1h-steel. Figure 3.5 shows the results of EBSD measurements for 8h-steel at 488 MPa, which reveals the crystallographic features of a small fatigue sub-crack propagation path. Figure 3.5(a) shows an example of a fatigue crack propagation ND-IPF map along the grain boundary. Similar to the case of 1h-steel, austenite was mostly transformed at the vicinity of the crack tip.

3.3.2 Crack initiation and propagation in low cycle fatigue

The fatigue crack propagation at high stress amplitudes is shown in Fig. 3.6, where

the fatigue crack length and crack growth rates are plotted against the number of cycles at 760 MPa in 1h-steel and at 741 MPa in 8h-steel. There was no significant difference in the small fatigue crack growth rate between 1h-steel and 8h-steel before 2.0×10^4 cycles. However, the large fatigue crack growth rate after 2.0×10^4 cycles in 1-h steel was lower than that in 8h-steel (Fig. 3.6(b)). The diagrams of fatigue crack growth rate against crack length are shown in Fig. 3.6(c) and 3.6(d).

Figure 3.7(a) shows the fatigue crack was initiated along the grain boundary in 1h-steel at a high stress amplitude of 760 MPa. The fatigue crack propagated both along and across the lamella alignment. In the case of the fatigue crack that propagated across the lamella alignment (Fig. 3.7(b)), the fatigue crack path formed a zigzag pattern, as also observed in the previous study [6]. These could be attributed to two phenomena: (i) the crack propagation along the lamella alignment shown in Fig. 3.7(c), and (ii) the frequent occurrence of crack coalescence shown in Figs. 3.7(d) and (e).

As shown in Fig. 3.8(a), 8h-steel at 741 MPa showed crack initiation mainly from the grain boundary, similar to 1h-steel. The propagation behavior is also quite similar to 1h-steel, as shown in Figs. 3.8(b) and (c), which display the fatigue crack propagation across and along the lamella alignment, respectively. Frequent crack coalescence was observed, as shown in Figs. 3.8(d), (e).

3.3.3 Fractographic observations

Figures 3.9(a_1) and (b_1) show the fracture surface images with indications of fatigue crack initiation sites, fatigue crack propagation, and the final fracture zone in a 1h-steel specimen at 500 MPa and in a 8h-steel specimen at 488 MPa, which correspond to the high cycle fatigue regime. The final fracture zone, indicated by C. The fatigue crack

propagation areas are classified into smooth and rough surface regions, denoted by A and B, corresponding to Figs. 3.9(a_2) and (a_3), and Figs. 3.9(b_2) and (b_3), respectively. The crack growth rate in region A is relatively low, and thus the corresponding fracture surface can be rubbed for longer times resulting in a smooth topography.

In the low cycle fatigue, both fracture surfaces of 1h- and 8h-steels are shown in Figs. 3.10(a_1) and (b_1). They also consist of a fatigue crack propagation area and a final fracture zone indicated by A and B, respectively. The fracture surface corresponding to the fatigue crack propagation part is remarkably rougher than that of the high cycle fatigue, although a portion of the fracture surface exhibits smooth features and scratches, as respectively indicated by blue arrows and yellow dashed line in Figs. 3.10(a_2) and (b_2). In fact, the fracture surface is wavy along the circumferential direction, as indicated by the yellow arrows. This wavy feature is likely to correspond to the frequency of the fatigue crack coalescence observed in Figs. 3.7 and 3.8.

3.4 Discussion

3.4.1 Relative microstructural hardness

Due to the existence of 'soft' retained austenite [4], strong stress partitioning occurs between the 'soft' austenite and 'hard' maraging martensite, which results in preferential deformation of the austenite compared to the maraging martensite. The deformation-induced martensite (fresh martensite) is softer than the pre-existing maraging martensite matrix, because of the absence of Ni_2MnAl intermetallic precipitates in fresh martensite [5]. Thus, even after the occurrence of the TRIP effect, the maraging martensite is supposed to be the hardest phase. This is an important point to understand the difference between the fatigue limits of 1h and 8h-steels. In fact, the difference in the fatigue limit

cannot be explained solely by tensile strength differences related to macroscopic hardness [1]. Since fatigue crack initiation and small fatigue crack propagation occur selectively in the weakest microstructure, the martensite with intermetallic precipitates is not a preferential fatigue crack initiation and propagation path. Instead, austenite or austenite-related boundaries become the preferential crack initiation site and propagation path in the present steels. In terms of microstructural hardness, the lamellar spacing is self-evidently important to discuss the micro-hardness of austenite, i.e., decreasing lamellar spacing increases the micro-hardness of austenite because of a reduction in effective grain size [1].

3.3.2 Effect of lamellar spacing

Based on the replica images, the 1h- and 8h-steels showed similar characteristics in terms of fatigue crack initiation and propagation path. However, under the same stress amplitude ratio to tensile strength, there is a significant difference in fatigue lives between 1h- and 8h-steels. This fact is not only attributed to the difference in austenite fraction, but also to the lamellar spacing. As shown in previous work [4], the thickness of the retained austenite film increases with annealing time. This fact indicates that the effective grain size in austenite increases from 150 nm to 300 nm with annealing time from 1 hour to 8 hours. Therefore, the austenite region in the lamellar structure in 8h-steel is softer compared to that in 1h-steel. Thus, in the high cycle fatigue, the thick lamellar spacing in 8h-steel results in faster fatigue crack propagation than that of thin lamellar spacing (1h-steel). In other words, reducing the austenite thickness by decreasing the annealing time is beneficial to fatigue resistance, due to an increase in local hardness of the weakest microstructure i.e., strengthening austenite. Accordingly,

the fatigue limit is enhanced with decreasing annealing time, which explains why the ratio of fatigue limit to tensile strength of 1h-steel is higher than that of 8h-steel.

3.3.3 Fatigue crack initiation regime

In the high cycle fatigue, fatigue cracks in 1h-steel were preferentially initiated from pre-existing defects, such as inclusion, rather than specific microstructural boundaries, as shown in Fig. 3.2(b). On the other hand, fatigue cracks in 8h-steel were initiated from austenite-related boundaries. The suppression of fatigue crack initiation on the austenite-related boundaries in the 1h-steel is attributed to the higher hardness of austenite resulting from the thin lamellar spacing.

In contrast, in the low cycle fatigue, most of the retained austenite transformed to martensite before fatigue crack initiation due to the high stress amplitude. Moreover, the high stress amplitude caused multiple fatigue crack initiation sites. Since the coalescence of cracks causes deflection of the crack propagation path, a considerable amount of fatigue crack initiation provides large roughness, as seen in the fractographic analyses shown in Fig. 3.10. In the low cycle fatigue regime, no significant difference in fatigue crack initiation between 1h- and 8h-steels was observed, which indicates that the fatigue crack initiation site does not change by the difference in annealing time, namely, the fatigue cracks of both of the steels appeared along grain boundaries (Figs. 3.7(a) and 3.8(a)) where metastable austenite exists. The fatigue crack initiation at austenite-related boundaries would be caused by elastic misfit associated with a significant difference in hardness between maraging martensite and fresh martensite that transformed from metastable austenite[5]. The elastic misfit between the two phases causes high localized plastic strain in a vicinity of their interface. Even after deformation-induced martensitic

transformation, the maraging martensite is harder than fresh martensite because of the presence of intermetallic compounds [2]. Thus, the plastic strain localization mechanism is active both before and after martensitic transformation, irrespective of metastable austenite fraction. Since the fatigue crack initiation life is remarkably shorter than the propagation life when the stress amplitude is high, the fatigue crack initiation frequently occurred in the early stages of fatigue testing. Therefore, the coalescence of crack arising from multiple crack initiation increase fatigue crack growth rate. This point must be affected by retained austenite fraction.

3.3.4 Fatigue crack propagation regime

The formation of a zigzag pattern in the fatigue main crack propagation path was often caused by lamella alignment at both low and high cycle fatigue regimes, as shown in Figs. 3.2(f), 3.4(f), 3.7(c) and 3.8(c). The hierarchical laminated microstructure contributes to decelerate fatigue crack propagation when it reached a boundary as shown in Figs. 3.2(c)(d) and 3.4(d)(e). In addition, crack branching occurred along the lamella alignment e.g. Fig. 3.2(g). The deflection and branching of cracks in a μm-scale can be attributed to two main factors: (i) hierarchical lath martensitic structure with a considerable amount of austenite film; and (ii) higher hardness of the maraging martensite, even in deformed microstructures. The combined effect of the two factors causes deformation inhomogeneity, which guides the fatigue crack propagation into austenite or austenite-related boundaries. In addition, the fatigue crack propagation across the lamellar structure at a specific combination of loading direction and lamella alignment provides saw-teeth-like crack surface morphologies. Specifically, the austenite region is highly deformed before the crack penetrates the hard maraging

martensite, which causes nm-scale roughness. Interestingly, the effects of the austenite fraction and lamellar spacing did not provide a significant difference between 1h- and 8h-steels regarding the crack propagation path. However, similar to the fatigue crack initiation regime, smaller effective grain sizes in the 1h-steel caused a lower fatigue crack growth rate in the austenite region compared to that in 8h-steel.

In the high cycle fatigue regime shown in Fig. 3.1, the fatigue crack growth rate of 1h-steel is lower than that of 8h-steel, regardless of the number of cycles, although the main crack of 1h-steel initiated early from the defect. The lower crack growth rate of 1h-steel is attributed to the thin lamellar spacing, which restricts the motion of the dislocation emitted from a crack tip [6]. In addition, one of the most important characteristics of TRIP-maraging steel, namely TICC, also contributes to improve the fatigue life and fatigue limit. As shown in Figs. 3.3(b) and 3.5(b), the austenite region transformed to martensite. This fact indicates that the TICC was associated with the material volume dilatation, causing a compressive residual stress at the crack tip. Unlike the TRIP effect in tensile testing, the average volume fraction of retained austenite is not important for the fatigue crack closure. Instead, the local retained austenite fraction at the crack tip is important in high cycle fatigue, where the stress amplitude is much lower than the macroscopic yield strength. In other words, increasing the number of austenite films is less effective at low stress amplitudes around the fatigue limit, since TICC cannot be dramatically enhanced by increasing the austenite fraction. A difference in mechanical phase stability of austenite associated with grain size and elemental partitioning may compensate the difference in austenite fraction between the two steels. The effect of mechanical phase stability will be concerned in a future work. In addition, note that a preferential crack propagation path is a relatively soft region i.e. austenite

region. Hence, in high cycle fatigue, longer fatigue life of 1h-steel than that of 8h-steel is attributed to a combined effect of high hardness, connectivity, and optimal fraction of local austenite at the crack tip.

In the low cycle fatigue regime, the transformation from austenite to martensite has already occurred before the crack initiation, since the stress amplitude is higher than the yield strength. The homogeneous volume expansion by transformation cannot act as TICC. As a result, the crack growth rates of 1h- and 8h-steels at the same normalized stress amplitude are nearly the same before 1.7×10^4 cycles, as shown in Fig. 3.6(b). Nevertheless, significant differences on the crack growth rate appear when the crack becomes long, e.g. after 1.7×10^4 cycles, where 8h-steel showed faster propagation rates than 1h-steel. This phenomenon may be attributed to the differences in retained austenite distribution of initial microstructure. The retained austenite is always distributed sparsely in 1h-steel, while in 8h-steel it is usually distributed as a quasi-continuous network [3]. In the low cycle fatigue, the preferential crack propagation path is through fresh martensite transformed from austenite, which is significantly softer than maraging martensite with intermetallic precipitates. Therefore, a decrease in the connectivity of fresh martensite in the 1h-steel increases the existing probability of having maraging martensite at the crack tip, particularly for a long crack, decelerating the fatigue crack growth rate compared to that of 8h-steel with higher austenite connectivity.

Although a significant difference in the fatigue crack growth rate was observed between the 1h- and 8h-steels, both steels showed remarkable roughness on the fatigue crack surface, shown by the topography in Figs. 3.10(a_1) and (b_1) and the zigzag pattern propagation path in Figs. 3.7 and 3.8. As observed in the replica images, the main factors creating the zigzag path are grain boundary cracking and lamella alignment. Therefore,

the degree of roughness is considered to be independent of the austenite fraction as long as the microstructure can be recognized as austenite/maraging martensite lamellae. Consequently, the major factor, RICC, was not affected by the change in lamella size and connectivity. Finally, on the fracture surface, smooth regions and scratches were observed in Figs. 3.10(a_2) and (b_2). This fact indicates that crack surfaces rubbed each other, which supports the occurrence of RICC in both steels.

3.5 Section conclusion

The effects of austenite/martensite lamella size and austenite connectivity on the fatigue behavior of TRIP-maraging steels were investigated by analyzing the crack initiation site, propagation path, and fracture surface. The conclusions are as follows.

(1) The fatigue life and strength of 1h-steel are superior to that of 8h-steel, which results from two factors: (i) relatively high hardness of austenite, arising from thinner austenite film thickness; and (ii) lower connectivity of austenite.

(2) Even after the TRIP phenomenon, the pre-existing maraging martensite is the hardest phase. This leads to preferential fatigue crack propagation either along austenite-related boundaries, producing a zigzag pattern on the propagation path.

(3) The austenite connectivity affects the fatigue crack growth rate, i.e., less austenite connectivity provides high resistance to long crack propagation because of the number of maraging martensite increases. In addition, in the low cycle fatigue regime, both 1h- and 8h-steels present RICC, which can be demonstrated by comparing the zigzag fatigue crack path from replica images and smooth fracture surfaces. However, a significant effect of the lamella size and connectivity on RICC was not observed in the present study.

3.6 References

[1] M. Koyama, Z. Zhang, M. Wang, D. Ponge, D. Raabe, K. Tsuzaki, H. Noguchi, C.C. Tasan, Bone-like crack resistance in hierarchical metastable nanolaminate steels, Science, 355 (2017) 1055-1057.

[2] M.M. Wang, C.C. Tasan, D. Ponge, A.C. Dippel, D. Raabe, Nanolaminate transformation-induced plasticity–twinning-induced plasticity steel with dynamic strain partitioning and enhanced damage resistance, Acta Materialia, 85 (2015) 216-228.

[3] M. Abareshi, E. Emadoddin, Effect of retained austenite characteristics on fatigue behavior and tensile properties of transformation induced plasticity steel, Materials & Design, 32 (2011) 5099-5105.

[4] M.M. Wang, C.C. Tasan, D. Ponge, A. Kostka, D. Raabe, Smaller is less stable: Size effects on twinning vs. transformation of reverted austenite in TRIP-maraging steels, Acta Materialia, 79 (2014) 268-281.

[5] J. Millán, S. Sandlöbes, A. Al-Zubi, T. Hickel, P. Choi, J. Neugebauer, D. Ponge, D. Raabe, Designing Heusler nanoprecipitates by elastic misfit stabilization in Fe–Mn maraging steels, Acta Materialia, 76 (2014) 94-105.

[6] M.A. Daeubler, A.W. Thompson, I.M. Bernstein, Influence of microstructure on fatigue behavior and surface fatigue crack growth of fully pearlitic steels, Metallurgical Transactions A, 21 (1990) 925-933.

3.7 Tables and figures

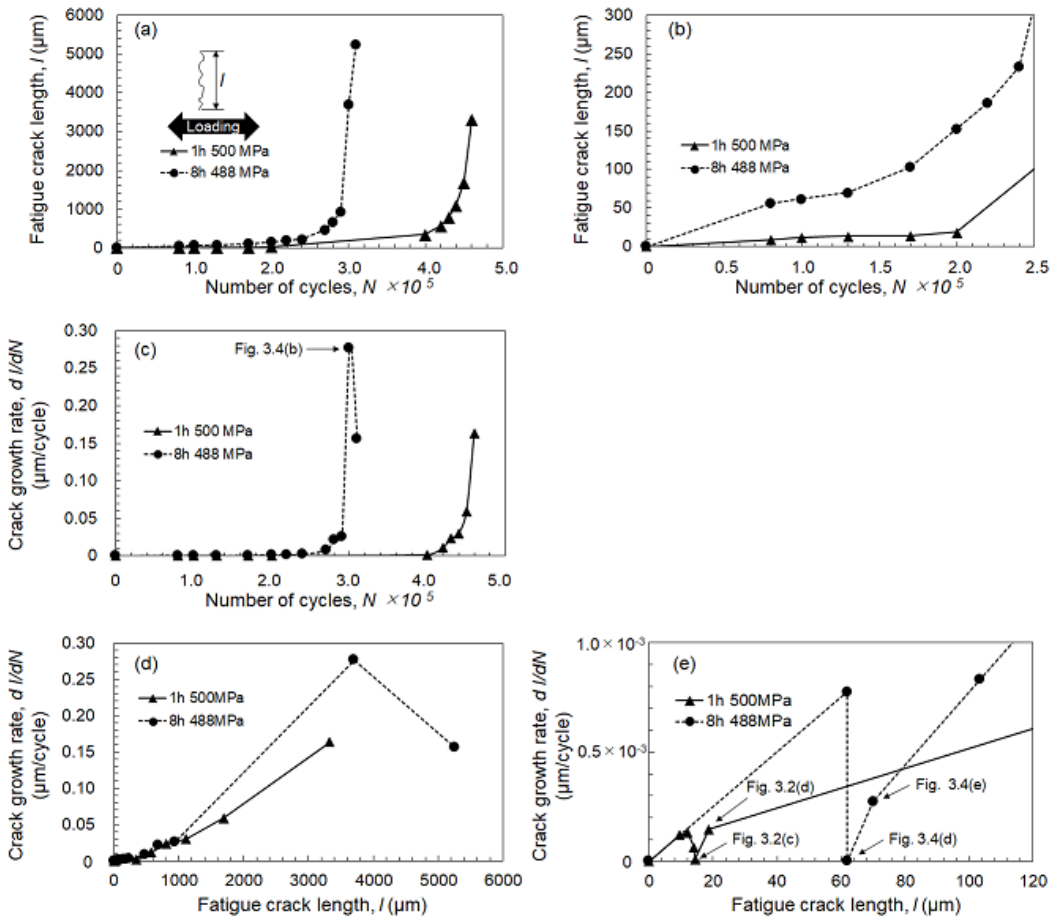

Fig. 3.1. Crack growth data in the high cycle fatigue regime. (a) Fatigue crack length plotted against the number of cycles, (b) magnified graph of the region for small crack growth (0-2.5×10^5 cycles), and (c) corresponding crack growth rate plotted against the number of cycles. (d) Fatigue crack growth rate plotted against fatigue crack length, and (e) its magnified graph of the small crack growth region (0-120 mm of crack length). The stress amplitude/tensile strength ratio is 0.54.

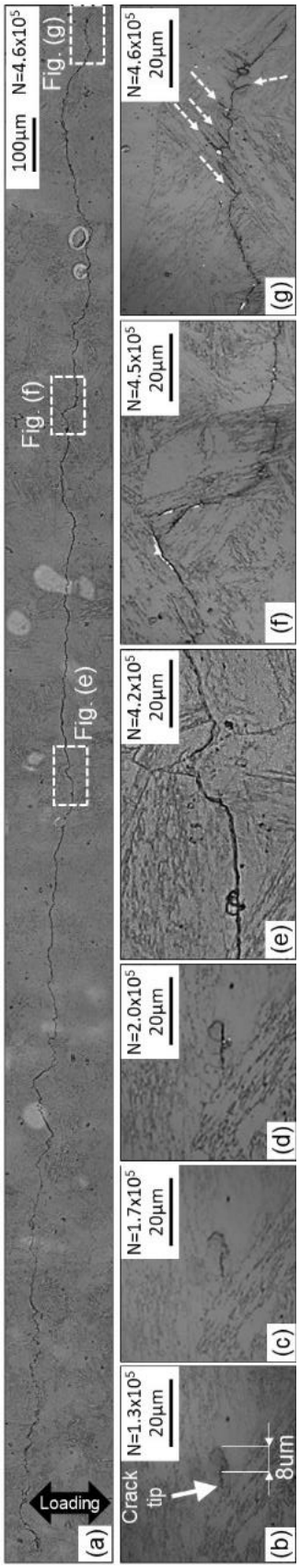

Fig. 3.2. A 1 h-steel tested at 500 MPa with fatigue life 4.68×10^5 cycles. Replica images showing (a) the fatigue crack propagation path, and (b) the crack initiation at a pre-existing defect. (c-d) the left tip of the crack stopped to move, and the right tip propagated. (e-f) Magnified images of the regions indicated in (a). The black arrows indicate the location of the defect acting as the crack initiation site. The white dashed arrows indicate fatigue crack branching.

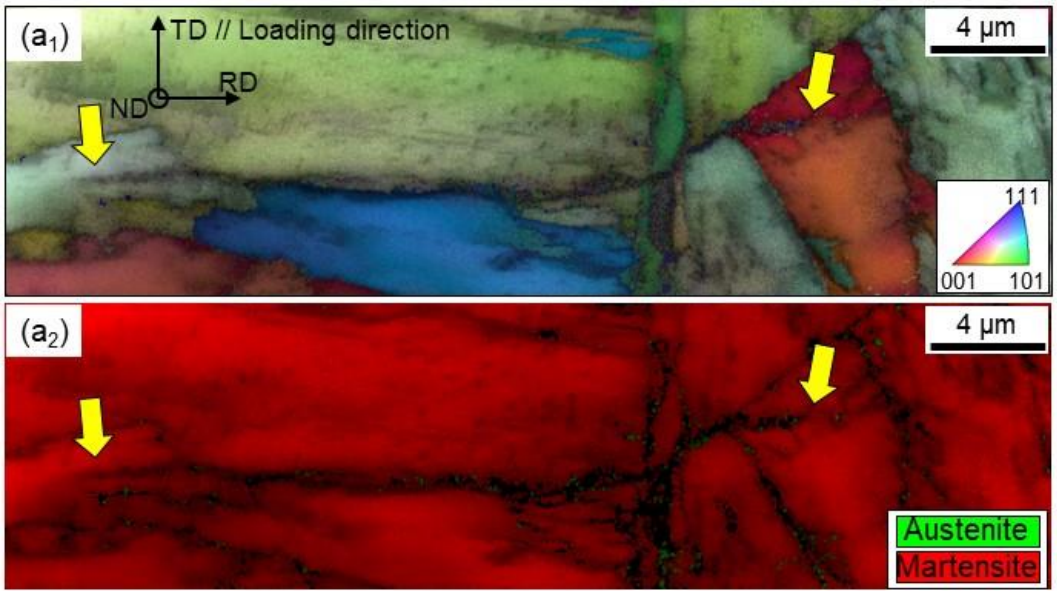

Fig. 3.3. EBSD data of high cycle fatigue sub-crack in 1h-steel at 500 MPa obtained after the failure at 4.68×10^5 cycles. (a) ND-IPF map with IQ contrast and (b) phase map with IQ contrast. The arrows indicate fatigue crack tip.

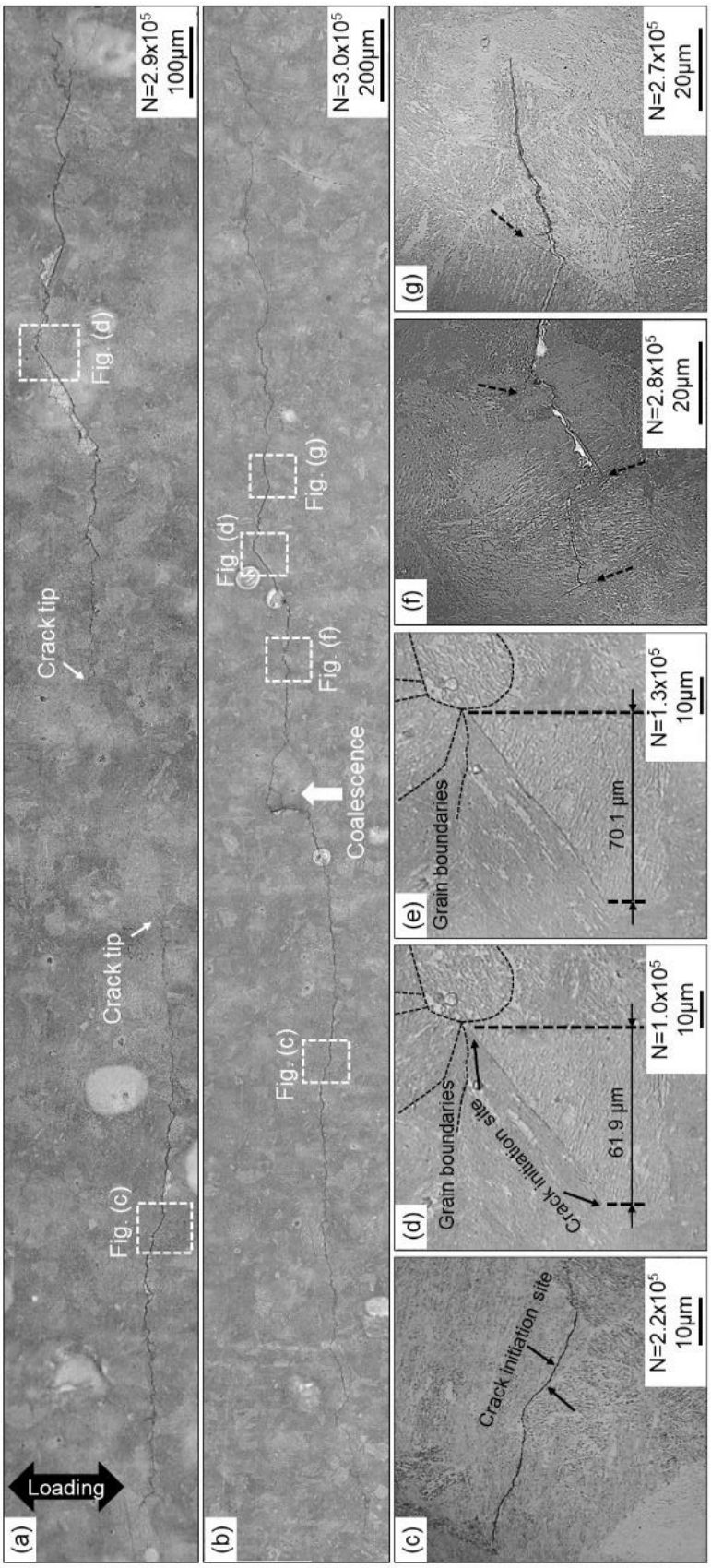

Fig. 3.4. A 8 h-steel tested at 488 MPa with fatigue life 3.14×10^5 cycles. Replica images showing the fatigue crack propagation path (a) before coalescence and (b) after coalescence. (c) A crack initiation from the boundary. (d) Another crack initiated from a boundary. (e) The crack grew slowly due to presence of grain boundaries. (c-g) Magnified images of the regions indicated in (b).

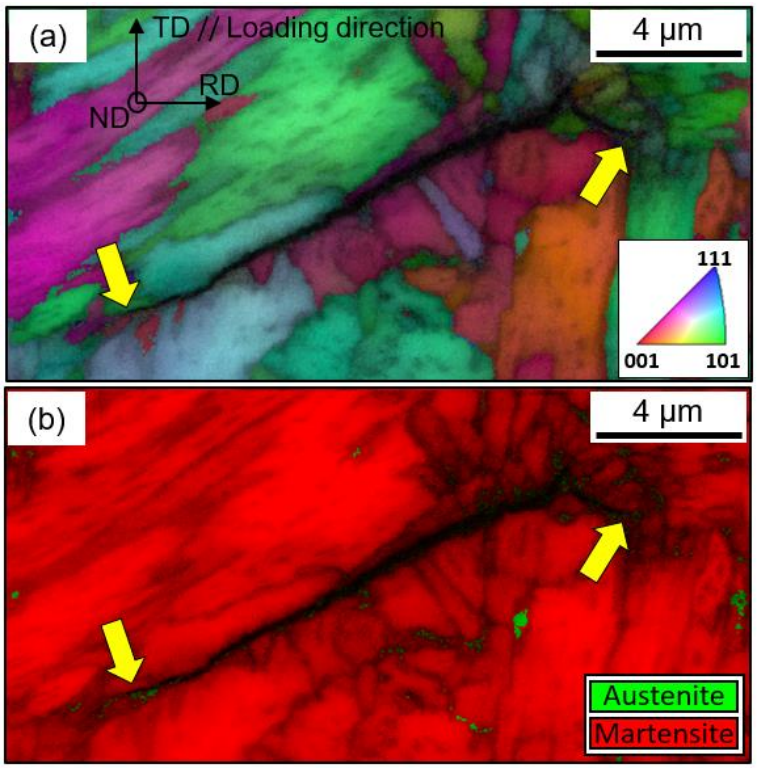

Fig. 3.5. EBSD data of high cycle fatigue sub-crack in 8h-steel at 488 MPa obtained after the failure at 3.14×10^5 cycles. (a) ND-IPF map with IQ contrast and (b) phase map with IQ contrast. The arrows indicate fatigue crack tips.

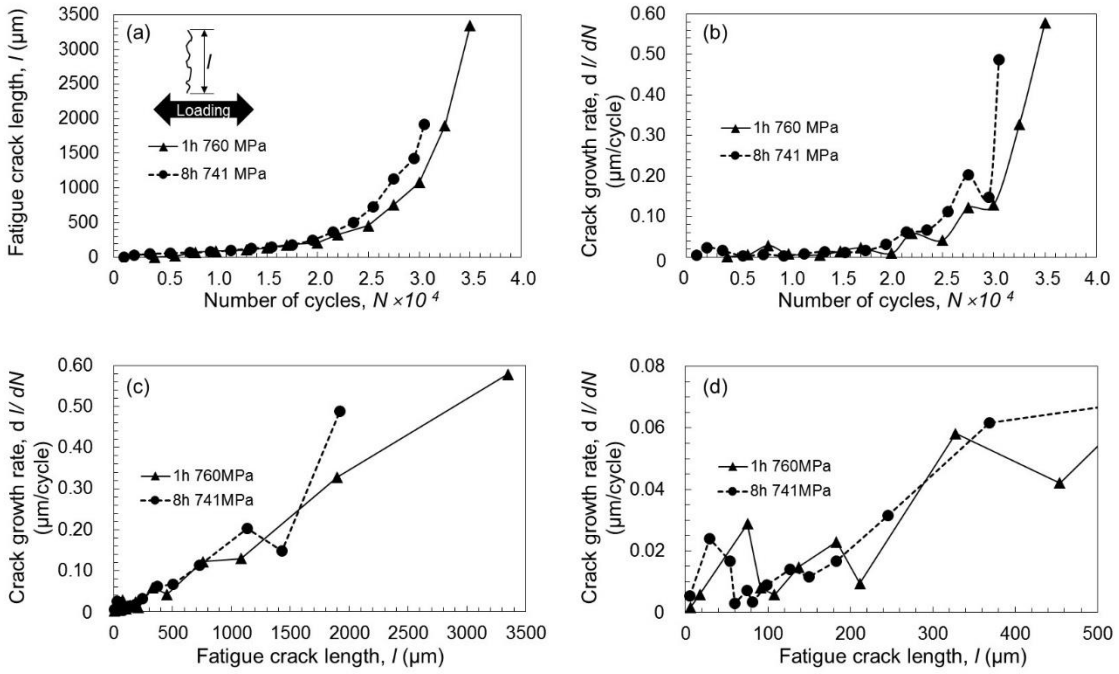

Fig. 3.6. Crack growth data in the low cycle fatigue regime. (a) Fatigue crack length and (b) corresponding crack growth rate plotted against the number of cycles. (c) Fatigue rack growth rate plotted against fatigue crack length, and (d) its magnified graph of region for crack growth rate (0-500 μm of crack length). The stress amplitude/tensile strength ratio is 0.82

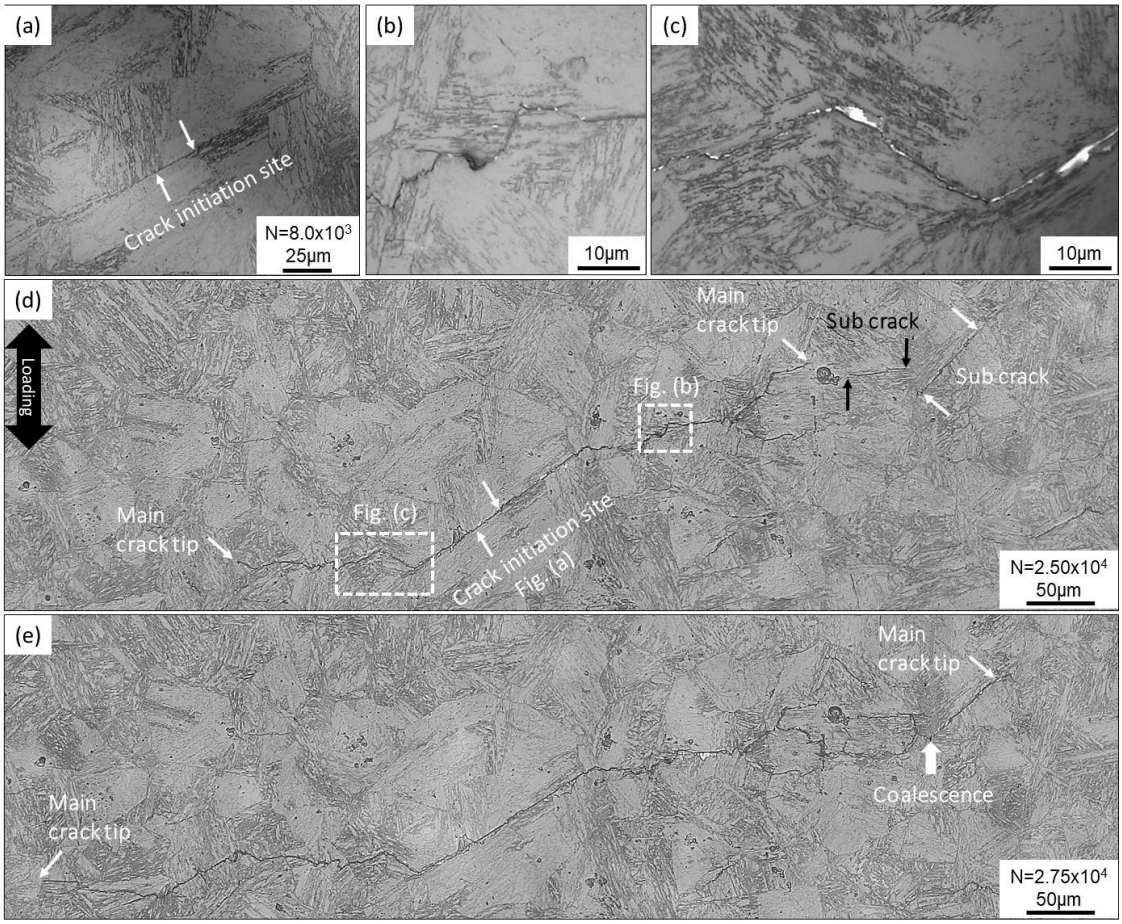

Fig. 3.7. 1h-steel at 760 MPa with fatigue life of 3.60×10^4 cycles. (a) Main crack initiation site, (b) fatigue crack propagation across the lamella alignment, (c) fatigue crack propagation along the lamella alignment, and (d) main crack propagation path before coalescence and (e) after coalescence.

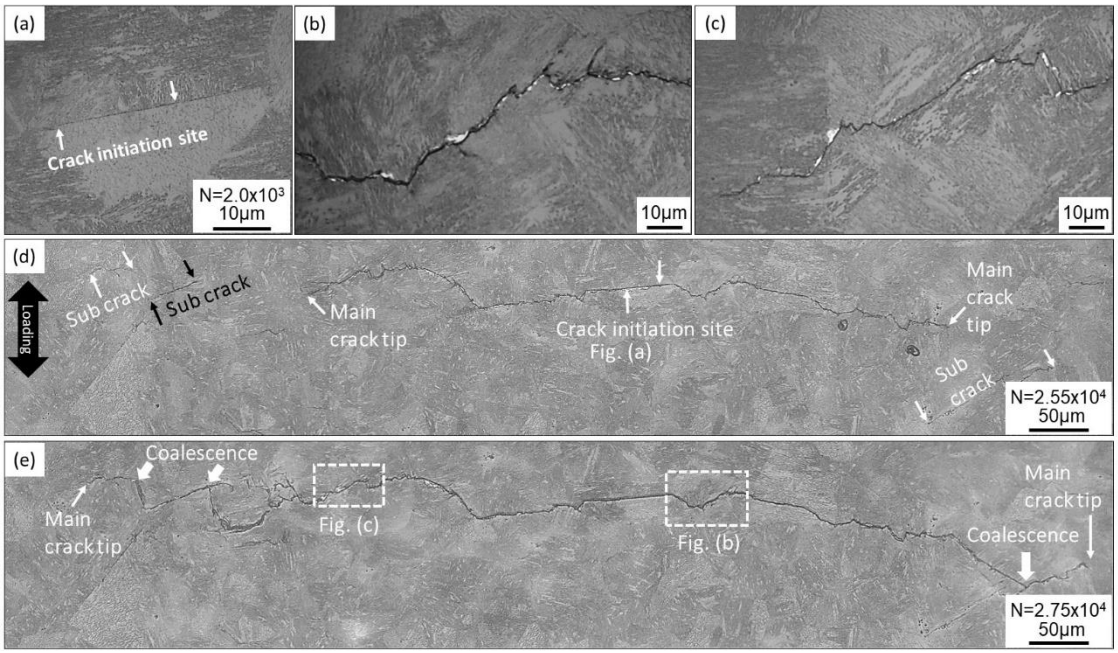

Fig. 3.8. 8h-steel at 741 MPa with fatigue life of 3.15×10^4 cycles. (a) Main crack initiation site, (b) fatigue crack propagation across the lamella alignment, (c) fatigue crack propagation along the lamella alignment, and (d) main crack propagation path before coalescence, and (e) after coalescence.

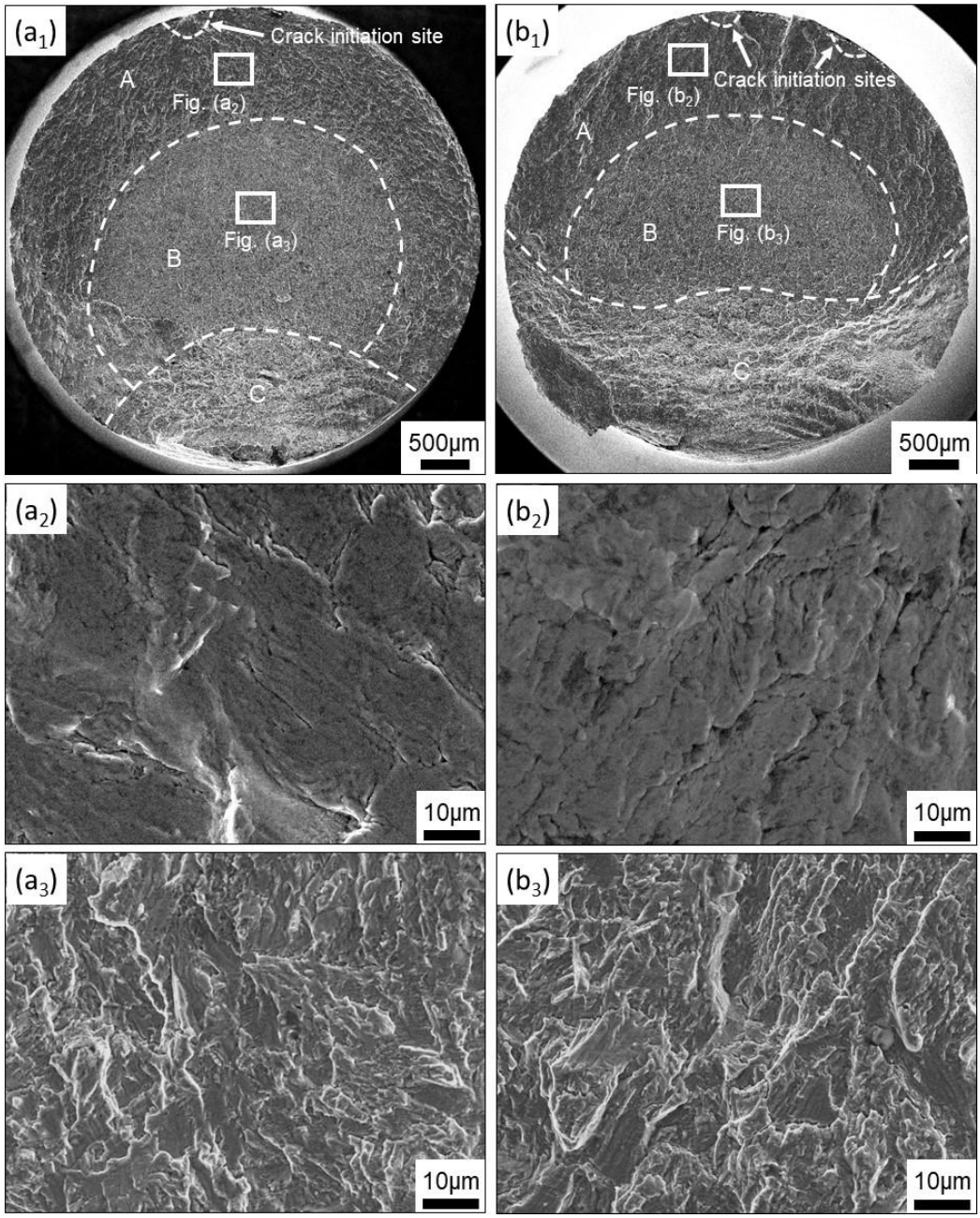

Fig. 3.9. Fracture surfaces obtained by high cycle fatigue in (a_1) the 1h-steel specimen at 500 MPa with fatigue life of 4.68×10^5 cycles and (b_1) the 8h-steel specimen at 488 MPa with fatigue life of 3.14×10^5 cycles. Images (a_2) and (b_2) are example of the smooth fatigue propagation region, and (a_3) and (b_3) are example of the rough fatigue propagation region.

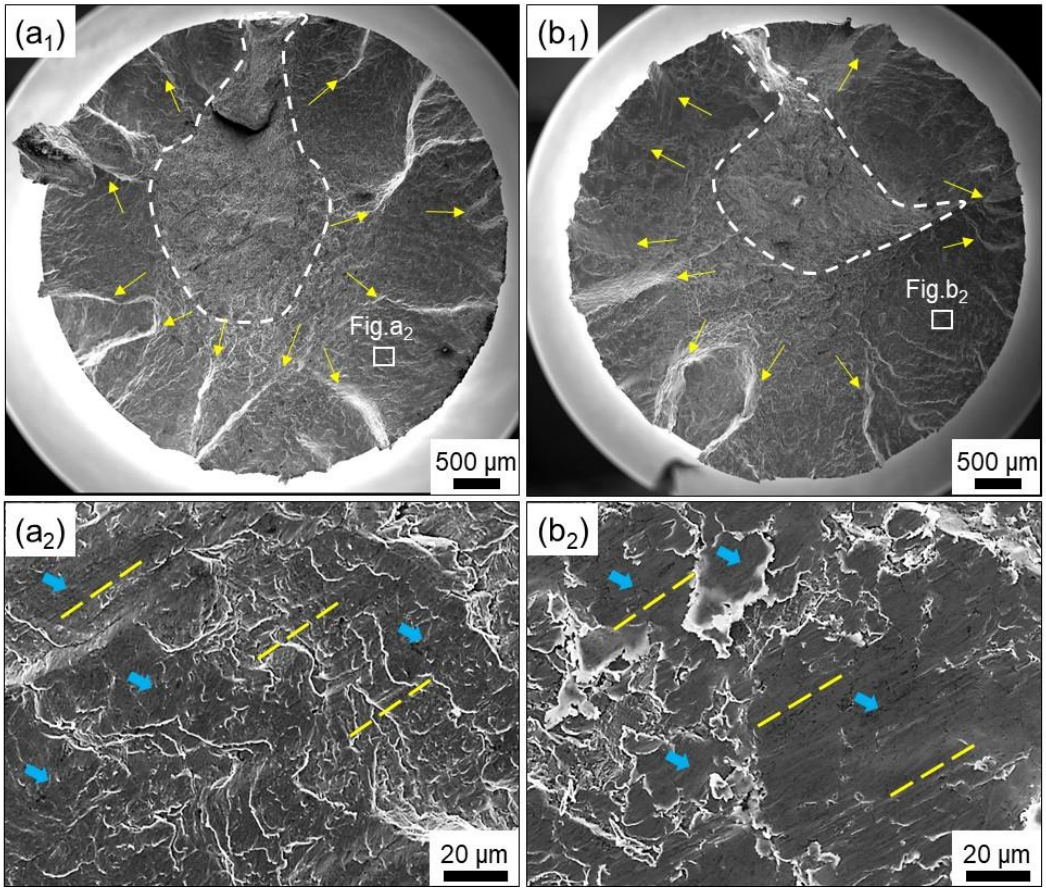

Fig. 3.10. Fracture surface of (a) 1h-steel at 800 MPa with fatigue life of 2.23×10^4 cycles and (b) 8h-steel at 780 MPa with fatigue life of 1.61×10^4 cycles. Blue arrows indicate smooth regions and yellow dashed lines highlight friction scratches. Final fracture region is highlighted by white dashed line.

CHAPTER 4. Microstructural mechanisms of fatigue crack non-propagation

4.1 Introduction

In the chapter 3, TRIP-maraging steels exhibited robustness of high cycle fatigue strength associated with fatigue crack growth resistance, because of the metastable laminated microstructure [1]. It has been demonstrated that metastable retained austenite can decelerate fatigue crack growth owing to the introduction of extra compressive stress at the crack tip pertaining to martensitic transformation from close-packed to non-close-packed crystal structures, i.e., transformation-induced crack closure, i.e., TICC [2, 3]. Accordingly, TRIP can contribute to fatigue crack resistance particularly at high cycle fatigue regime. Moreover, a laminated structure also contributes to fatigue life by deflecting a crack, which can result in the roughness-induced crack closure (RICC) and the associated reduction in the effective driving force for crack growth [4, 5].

From engineering point of view, the fatigue limit has generally been determined as the stress amplitude where a specimen is not fractured at 10^7 cycles, and thus, the high cycle fatigue regime is regarded as the most important phenomenon in engineering structure design. In fact, fatigue limit can be relatively low even if the tensile strength is high such as in pearlitic steels [6]. Therefore, the improvement of high cycle fatigue resistance and fatigue limit has been a primary issue for the use of high-strength

materials in actual structure parts. Accordingly, in this study, we firstly investigate the underlying mechanisms of the influences of TRIP and roughness on high cycle fatigue with respect to microstructure characteristics such as lamellar alignment and martensitic transformation behavior at the fatigue crack tip. Further, we focus on the relationship between microstructure and fatigue crack non-propagation at the fatigue limit.

The investigation of small sub-cracks revealed that the metastable laminated microstructure did not completely restrict crack initiation at retained austenite [7]. However, non-propagating cracks were observed at the surface of the 1 h-steel at 400 MPa, which is defined as the conventional engineering fatigue limit of a TRIP-maraging steel [1]. Therefore, the fatigue crack non-propagation mechanism is key to reveal the superior high cycle fatigue resistance. Considering that retained austenite grains are located along the boundaries of maraging martensite, the maraging martensite with significant deformation resistance owing to the existing intermetallic compounds might highly restrict the transformation-induced volumetric expansion from the retained austenite and increase the compressive residual stress. Moreover, the hierarchical laminated microstructure not only improves the crack deflection and associated RICC, but also acts as an obstacle against crack propagation. The non-propagating cracks at 400 MPa must be influenced by the TRIP and hierarchical microstructure. In fact, fatigue failure occurred at 400 MPa, which is the very high cycle fatigue regime, perhaps owing to the presence of internal inclusions [7]. However, as mentioned above, the nature of the very high cycle fatigue stemming from internal inclusions is beyond our scope, and we specifically aim to clarify the microstructural mechanism of the fatigue crack non-propagation at the fatigue limit in this study in order to generalize the design concept of metastable laminated microstructure regarding metal fatigue.

4.2 Experimental procedure and microstructure characterization

The main purpose of this work is to analyze the fatigue crack propagation mechanism in the high cycle fatigue regime. Therefore, we characterized the microstructure and crack growth behavior using specimens and their replica images obtained from chapter 2. With the specimen tested at the stress amplitude of 450 MPa, we focused on characterizing fatigue crack initiation and subsequent small crack growth behavior in the high cycle regime for a comparison with fatigue crack non-propagation at the fatigue limit of 400 MPa. At the fatigue limit where the specimen did not exhibit fracture at 10^7 cycles, we analyzed the influence of microstructures on fatigue crack non-propagation. Details of the fatigue crack "non-propagation" and associated microstructure at the fatigue limit have never been examined so far. The fatigue crack length was measured using the plastic replica method. The crack length was defined as projected length of surface cracks on respective replica images. The crack length includes a size of an initiation site such as inclusion.

In order to clarify the fatigue behavior of the TRIP-maraging steel, microstructure characterizations were carried out using optical microscope and SEM-based EBSD measurements. EBSD measurements were performed at an accelerating voltage of 15 kV with a beam step size of 50 nm to observe the distribution of retained austenite and the propagation path of small fatigue crack. The characteristics of the fatigue fracture surface were observed using SEM at an accelerating voltage of 15 kV.

4.3 Results

4.3.1 High cycle fatigue crack growth

First, we present fatigue crack growth behavior in high cycle fatigue regime for a comparison with behavior of fatigue crack non-propagation shown later. Figure 4.1 shows a set of replica images for a specimen fractured at 2.27×10^6 cycles under a stress amplitude of 450 MPa. Note that the specimen surface was entirely flat prior to the test as shown in Fig. 4.1b. Subsequently, the surface was distorted during the test, which caused surface relief with a circular shape as shown in Fig. 4.1c. The circular shape could correspond to an inclusion underneath the specimen surface, which acted as a stress concentration source [8, 9]. Owing to the presence of "soft" and metastable retained austenite along the martensite-related boundaries in the TRIP-maraging steel, the fatigue crack initiated from this deformed area and further propagated along the martensite packet boundary (Fig. 4.1d).

Fatigue crack propagation was decelerated when the laminated microstructure tended to be aligned perpendicular to the direction of crack growth, as indicated by the yellow arrows in Figs. 4.1e–f (or Figs. 4.1g–h), resulting in the retardation of crack growth at the austenite/martensite interface. In contrast, the other side of the crack tip propagated parallel to the lamellar alignment, as indicated by the red arrows, exhibiting relatively faster growth until reaching the martensite boundaries as shown in Figs. 4.1e–f (or Figs. 4.1g–h). Accordingly, the crack deflection strongly depends on the alignment direction of the laminated microstructure consisting of maraging martensite and retained austenite [10].

Conventional maraging steels have high tensile strength, but the impact tests demonstrated them to be susceptible to brittle fracture, which is characterized by evident

grain facets caused by the carbides at prior austenite grain boundaries and various martensite boundaries [11]. In TRIP-maraging steel, brittle phenomenon was not observed on the fracture surface (Fig. 4.2), which is attributed to the presence of retained austenite rather than carbides at the boundaries [12]. The retained austenite increases the ductility and leads to the formation of a dimpled fracture surface as observed in Fig. 4.2d. These observations for crack "propagation" are consistent with the previous study that showed almost the same behavior of crack propagation at a relatively high stress amplitude [7].

4.3.2 Fatigue crack non-propagation at the fatigue limit

At least three non-propagating fatigue cracks were observed in a single specimen tested at 400 MPa. Figure 4.3 shows the fatigue crack length plotted against the number of cycles. The non-propagating cracks were formed with the length of 75–80 μm as shown in Fig. 4.3a. The crack growth rates fluctuated as shown in Fig. 4.3b. Figure 4.4 shows the fracture surface of the specimen, which showed failure after 10^7 cycles. This image demonstrates that the crack was initiated from an internal inclusion, and its subsequent propagation caused the failure after 10^7 cycles. In other words, the failure at 400 MPa indicates the typical very high cycle fatigue regime, which is out of scope of this study.

Figure 4.5 shows the inverted replica images of crack 1, corresponding to the black curve in Fig. 4.3. The fatigue crack initiation was observed at 1.00×10^7 cycles, which originated from the inclusion acting as the stress concentration site as shown in Fig. 4.5c. Subsequently, the crack propagated along the austenite-related boundary, which caused a sudden initial increase in the crack growth rate. A unit length of the initial rapid

propagation of a fatigue crack corresponds to the martensite packet size or prior austenite grain size. With further increase in the number of cycles, the fatigue crack stopped propagating at a certain length as shown in Figs. 4.5f–h. To analyze the underlying crystallographic features, the sample was subjected to slight mechanical polishing and the subsurface microstructure was investigated using EBSD (Fig. 4.6). The crack path near the bottom of the crack tip is indicated by a yellow dashed line shown in the magnified inset within the EBSD images. Crack branching along the lamellar boundary was also observed as indicated by a green arrow. Austenite was barely observed near the crack, indicating that it had already transformed into martensite (Fig. 4.6c). The corresponding KAM map shows high values along most of the austenite-related boundaries compared with the other regions (Fig. 4.6d).

Figure 4.7a shows a replica image of the microstructure before the initiation of crack 2. The crack initiated from an inclusion is indicated by a white arrow and crack tips are marked by black arrows in Fig. 4.7b. Most of the crack path was along the lamellar alignment and grain boundary. Subsequently, the top side of the propagating crack encountered lamellae aligned nearly perpendicular to the direction of propagation, as indicated by the black dashed region. In contrast to the non-propagation of the bottom side of the crack tip, the top side of the crack tip continued to propagate within the laminated structure in a zigzag path (Fig. 4.7b-d). Eventually the crack propagation of the top side stopped from 2.00×10^7 cycles (Fig. 4.7e–g). A detailed observation showed that the crack propagated across the laminated structure in a tortuous path, as highlighted by the yellow dashed line in Fig. 4.7h. The corresponding EBSD results showed that the fatigue crack propagated through a martensite packet including martensite blocks with different orientations surrounded by the white dashed line in Fig. 4.8b. The phase map

showed that austenite barely existed near the crack, which indicated that the martensitic transformation was induced by the deformation of the crack tip (Fig. 4.8c). In order to observe the crack path deeply, the identical region was further mechanically polished to show a new microstructure as shown in Fig. 4.9 (the new subsurface was approximately 12 μm from the original spherical surface). Compared with the original microstructure shown in Fig. 4.8b, it can be observed that the shape of the identical region within the latest polished subsurface was different, as highlighted by the white dashed region (Fig. 4.9b). The top side of the crack propagation path passed through a grain in a tortuous path indicated by the white arrow in the IPF map (Fig. 4.9c). The other side of the crack path was along the boundaries, and the tip penetrated into the grain (Fig. 4.9d). From the overall point of view, notably, the austenite fraction in the subsurface in Fig. 4.9e was higher than that of the surface in Fig. 4.8c, demonstrating that the martensitic transformation occurred easier in the specimen surface than in the subsurface.

Figure 4.10 shows the replica images of crack 3 at 400 MPa. The fatigue crack initiated from the microstructure boundary at 7.6×10^6 cycles as shown in Fig. 4.10b. Subsequently, the crack was deflected owing to propagation along the microstructure boundaries and the finely zigzag transgranular crack growth across the packet/block boundaries (Figs. 4.10c–d). The crack penetrated into the neighboring packet (indicated by the black dotted line in Fig. 4.10e), and propagated along the block boundary (Fig. 4.10f). When the fatigue crack encountered the packet boundary again, it was observed to have stopped propagating until 2.96×10^7 cycles (Figs. 4.10g–h).

4.4 Discussion

4.4.1 Factors affecting fatigue crack initiation at fatigue limit

Before noting the crack non-propagation, we first discuss an origin of the crack at the fatigue limit. The KAM maps before and after the fatigue tests (Figs. 2.3a$_4$ and 4.6d) show that the austenite-related boundaries were susceptible to plastic deformation, whereas most parts of the maraging martensite exhibited no plastic deformation even after the test at the fatigue limit of 400 MPa (Fig. 4.6d). Note that only maraging martensite contains the intermetallic compounds [13]. Intermetallic compounds enhance the yield and ultimate tensile strength of the maraging martensite. Therefore, maraging martensite is more resistant to plastic deformation than retained austenite. According to a previous study [10], during an in-situ experiment, the austenite in TRIP-maraging steel transformed to α′-martensite at low strain, i.e., approximately 2%. In other words, crack initiation would occur at an austenite region, as a fatigue crack always forms in the softest microstructure. Furthermore, an inclusion existing on an austenite-related boundary was observed to assist the main fatigue crack nucleation at the stress amplitudes of 400 and 450 MPa, as it caused stress concentration like a hole as shown in Figs. 4.1d, 4.5c, and 4.7b. An analogous phenomenon was observed in a previous work where a crack also initiated from the an inclusion at a stress amplitude of 500 MPa in a similar type of TRIP-maraging steel [7]. According to the previous study [7] and Figs. 4.1, 4.5 and 4.7, the primary fatigue crack initiation site is concluded to be austenite-related boundary having an inclusion, irrespective of stress amplitude.

4.4.2 Microstructural characteristics of fatigue crack propagation

Next, we discuss the small fatigue crack propagation behavior prior to the non-

propagation. Based on the observations of the specimen surface replica and post-mortem EBSD analyses, the effects of a hierarchical laminated microstructure on the fatigue crack resistance are schematically illustrated in Fig. 4.11. Owing to the low stress intensity factor at the small crack tip, crack prefers to propagate along the microstructure boundaries such as the prior austenite grain boundary and packet/block boundaries. A crack along the boundaries encounters the retained austenite via propagation, which facilitates the deformation of the austenite (Fig. 4.11a). The deformation of crack opening triggers the martensitic transformation at the crack tip as shown in the EBSD phase maps of Figs. 4.6c, 4.8c and 4.9e, which decelerated crack growth (Fig. 4.11b). The deceleration associated with martensitic transformation has been discussed in terms of PICC [14] and associated TRIP effect [2]. For instance, in Fig. 4.6c, austenite was almost consumed for crack propagation-induced martensitic transformation. Correspondingly, the fatigue crack growth rate markedly decreased with crack length, which resulted in the non-propagating fatigue crack as shown in Fig. 4.5 (crack 1). When the plastic zone size is significantly large at a long crack tip [15], martensitic transformation occurs even in the retained austenite located slightly far from the crack tip (Fig. 4.11c). Assuming that crack closure effect can significantly work in this condition, the martensitic transformation ahead of the crack tip also contributes to PICC when the crack tip propagates into the transformed region. Work hardening associated with the TRIP effect is accomplished when the retained austenite is fully transformed into martensite. When the crack approaches fresh martensite, the crack-opening-related deformation induces dislocation multiplication, which enables further work hardening. After overcoming the crack closure effects and work hardening, the fatigue crack further propagates by yielding fresh martensite. With further propagation, the crack is resisted

by the martensite boundary (the bottom side of the crack in Figs. 4.10d and h) because grain boundaries containing atomistic misfits also act as strong barriers against dislocation motion [16] and subsequently cause back-stress arising from the dislocation pile-up [17, 18] (Fig. 4.11d). When a martensite packet/block boundary is aligned perpendicular to the direction of crack propagation, the crack grows across the laminated microstructure with a finely zigzag feature as experimentally shown in Fig. 4.7h (schematically in Fig. 4.11e). Although experimental quantification of the roughness effect on the crack growth is not possible in this study, the crack deflection and fine zigzag feature have been recognized to induce RICC, such as in pearlitic steels [19] and titanium alloy [20]. The RICC effect enables the reduction in the driving force of crack growth [2, 4], and thus decelerates the crack growth (Fig. 4.11e). In summary, in this propagation regime, the hierarchical microstructure and martensitic transformation jointly influence the resistance of fatigue crack growth. The hierarchical fine microstructure consisting of martensite boundary and martensite/austenite laminates causes (1) multiple types of crack deflection that would cause RICC, and (2) frequent occurrence of dislocation pile-up at the boundaries, which prevents crack opening. Crack-tip-opening-induced martensitic transformation induces (1) volumetric expansion from face centered cubic to body centered cubic, which can increase compressive residual stress and further enhance PICC, and (2) work hardening from soft austenite matrix to harder fresh martensite owing to TRIP at a crack front.

4.4.3 Microstructure effect on fatigue crack non-propagation

As mentioned above, the fatigue crack propagation path can be classified into two cases: across the laminated structure (Figs. 4.8b and 4.9b) and within the soft austenite

along the lamellar alignment (Fig. 4.6b). We discuss the details of the two cases separately.

The crack propagation across the laminates requires a higher driving force because the crack unavoidably propagates within hard maraging martensite where the dislocation mobility is low. According to a previous work [21], propagation from a soft to hard phase causes a greater effect of PICC compared with the case of single phase. Furthermore, the hierarchical microstructure of martensite consisting of prior austenite grain, packet, block, and lath enhances the deflection behavior via propagation along the martensite-related boundary. Specifically, the boundaries of the martensite block that is the smallest microstructure unit with a significant orientation change act as a major crack propagation path when the crack propagates within the maraging martensite region (polygon with the dashed line in Fig. 4.8b). This causes crack deflection (Fig. 4.7h), which can induce crack closure, i.e., RICC. As shown in Figs. 4.1e and f, crack propagation is retarded at the block boundaries, which indicates the difficulty of crack propagation across the block boundaries. Instead, crack tends to be deflected along the block boundary. A combined effect of these factors endows high fatigue crack non-propagation limit.

In contrast, the fatigue crack propagates preferentially along the austenite film when the lamella is aligned parallel to the propagation path. The progressive crack growth passing through multiple packet/block boundaries induces roughness in the crack morphology. Thus, RICC associated with the roughness is the most presumable positive effect of the retained austenite. The negative influence of retained austenite would accelerate crack growth with respect to maraging martensite, when the crack propagates along the laminates and approaches austenite as schematically shown in Fig. 4.12a. Assuming that the crack propagates via blunting and re-sharpening mechanism, the

crack growth requires stress accommodation at the crack tip. As austenite is soft, the number of dislocation emissions from the crack tip is greater than the case wherein the crack propagates within maraging martensite. Simultaneously, martensitic transformation also occurs at the crack tip (Fig. 4.12b). After the transformation, dislocation emission from the crack tip occurs in fresh martensite. The motion of the emitted dislocation can be impinged at the fresh martensite/maraging martensite interface or the intermetallic precipitates in maraging martensite (Figs. 4.12b and c). Note that a previous work demonstrated that the boundary between fresh martensite and maraging martensite exhibits a misorientation of only ~1° [13]. Such a low-angle boundary does not act as a strong obstacle against dislocation motion owing to the coherency of atomic arrangement [22, 23]. However, the intermetallic compounds in maraging martensite act as barriers against dislocation motion. Thus, the dislocation in austenite can move easily until it encounters the intermetallic compound, which causes a relatively high crack growth rate in austenite films. Correspondingly, the fatigue crack cannot stop around the central region of the austenite film (Fig. 4.12b) even at the fatigue limit when it is along the laminates (Fig. 4.7b). However, the large plastic deformation in retained austenite effectively assists work hardening and PICC. Therefore, coupled with the RICC, the enhanced work hardening and PICC can decelerate the subsequent crack growth after passing through the fresh martensite region. Consequently, the crack is terminated easily by the hard maraging martensite, resulting in a non-propagating fatigue crack as shown in Fig. 4.7e.

4.5 Section Conclusion

In this work, we investigated the microstructural effects on fatigue crack non-propagation and associated phenomena in a laminated TRIP-maraging steel to uncover the underlying mechanism of superior crack resistance. The findings of the present study are summarized as follows.

(1) Austenite-related boundaries having inclusions are the most susceptible to fatigue damage evolution compared with maraging martensite. The initial fatigue crack rapidly propagates along the "soft" austenite until it reaches the packet or prior austenite grain boundary.

(2) Although austenite is the preferential site for crack propagation, the crack opening induces martensitic transformation in the austenite region. The martensitic transformation enhances volume expansion and work hardening. These are important for deceleration of crack growth in terms of crack closure and dislocation motion resistance.

(3) A zigzag crack propagation path forms through its growth along the laminates and across the block boundary, which contributes to non-propagating fatigue crack.

4.6 References

[1] M. Koyama, Z. Zhang, M. Wang, D. Ponge, D. Raabe, K. Tsuzaki, H. Noguchi, C.C. Tasan, Bone-like crack resistance in hierarchical metastable nanolaminate steels, Science, 355 (2017) 1055-1057.

[2] R.O. Ritchie, Mechanisms of fatigue crack propagation in metals, ceramics and composites: Role of crack tip shielding, Materials Science and Engineering: A, 103 (1988) 15-28.

[3] H. Mayer, S. Stanzl-Tschegg, Y. Sawaki, M. Hühner, E. Hornbogen, Influence of transformation-induced crack closure on slow fatigue crack growth under variable amplitude loading, Fatigue & Fracture of Engineering Materials & Structures, 18 (1995) 935-948.

[4] S. Suresh, Crack deflection: Implications for the growth of long and short fatigue cracks, Metallurgical Transactions A, 14 (1983) 2375-2385.

[5] J. Tianfu, Z. Jingwu, F. Wantang, G. Ming, High performance steel plates with micro-laminated layer structure produced by plastic deformation, Journal of Materials Science Letters, 16 (1997) 485-489.

[6] G.T. Gray, A.W. Thompson, J.C. Williams, Influence of microstructure on fatigue crack initiation in fully pearlitic steels, Metallurgical Transactions A, 16 (1985) 753-760.

[7] Z. Zhang, M. Koyama, M.M. Wang, K. Tsuzaki, C.C. Tasan, H. Noguchi, Effects of lamella size and connectivity on fatigue crack resistance of TRIP-maraging steel, International Journal of Fatigue, 100, Part 1 (2017) 176-186.

[8] J. Polak, J. Man, K. Obrtlik, AFM evidence of surface relief formation and models

of fatigue crack nucleation, International Journal of Fatigue, 25 (2003) 1027-1036.

[9] J. Hyzak, I. Bernstein, The effect of defects on the fatigue crack initiation process in two P/M superalloys: Part I. Fatigue origins, Metallurgical transactions A, 13 (1982) 33-43.

[10] M.M. Wang, C.C. Tasan, D. Ponge, A. Kostka, D. Raabe, Smaller is less stable: Size effects on twinning vs. transformation of reverted austenite in TRIP-maraging steels, Acta Materialia, 79 (2014) 268-281.

[11] M. Sarikaya, A. Jhingan, G. Thomas, Retained austenite and tempered martensite embrittlement in medium carbon steels, Metallurgical Transactions A, 14 (1983) 1121-1133.

[12] M.M. Wang, C.C. Tasan, D. Ponge, A.C. Dippel, D. Raabe, Nanolaminate transformation-induced plasticity–twinning-induced plasticity steel with dynamic strain partitioning and enhanced damage resistance, Acta Materialia, 85 (2015) 216-228.

[13] J. Millán, S. Sandlöbes, A. Al-Zubi, T. Hickel, P. Choi, J. Neugebauer, D. Ponge, D. Raabe, Designing Heusler nanoprecipitates by elastic misfit stabilization in Fe–Mn maraging steels, Acta Materialia, 76 (2014) 94-105.

[14] W. Elber, The significance of fatigue crack closure, in: Damage tolerance in aircraft structures, ASTM International (1971) 230-242.

[15] D.S. Dugdale, Yielding of steel sheets containing slits, Journal of the Mechanics and Physics of Solids, 8 (1960) 100-104.

[16] W. Schaef, M. Marx, H. Vehoff, A. Heckl, P. Randelzhofer, A 3-D view on the mechanisms of short fatigue cracks interacting with grain boundaries, Acta Materialia, 59 (2011) 1849-1861.

[17] D.V. Wilson, Reversible work hardening in alloys of cubic metals, Acta Metallurgica, 13 (1965) 807-814.

[18] I. Groma, F.F. Csikor, M. Zaiser, Spatial correlations and higher-order gradient terms in a continuum description of dislocation dynamics, Acta Materialia, 51 (2003) 1271-1281.

[19] G.T. Gray, J.C. Williams, A.W. Thompson, Roughness-Induced Crack Closure: An Explanation for Microstructurally Sensitive Fatigue Crack Growth, Metallurgical Transactions A, 14 (1983) 421-433.

[20] K.S. Chan, Y.W. Kim, Influence of microstructure on crack-tip micromechanics and fracture behaviors of a two-phase TiAl alloy, Metallurgical Transactions A, 23 (1992) 1663-1677.

[21] B. Li, M. Koyama, S. Hamada, H. Noguchi, Threshold stress intensity factor range of a mechanically-long and microstructually-short crack perpendicular to an interface with plastic mismatch, Engineering Fracture Mechanics, 182 (2017) 287-302.

[22] T. Ohmura, A.M. Minor, E.A. Stach, J.W. Morris, Dislocation–grain boundary interactions in martensitic steel observed through in situ nanoindentation in a transmission electron microscope, Journal of Materials Research, 19 (2004) 3626-3632.

[23] T.C. Lee, I.M. Robertson, H.K. Birnbaum, AnIn Situ transmission electron microscope deformation study of the slip transfer mechanisms in metals, Metallurgical Transactions A, 21 (1990) 2437-2447.

4.7 Tables and figures

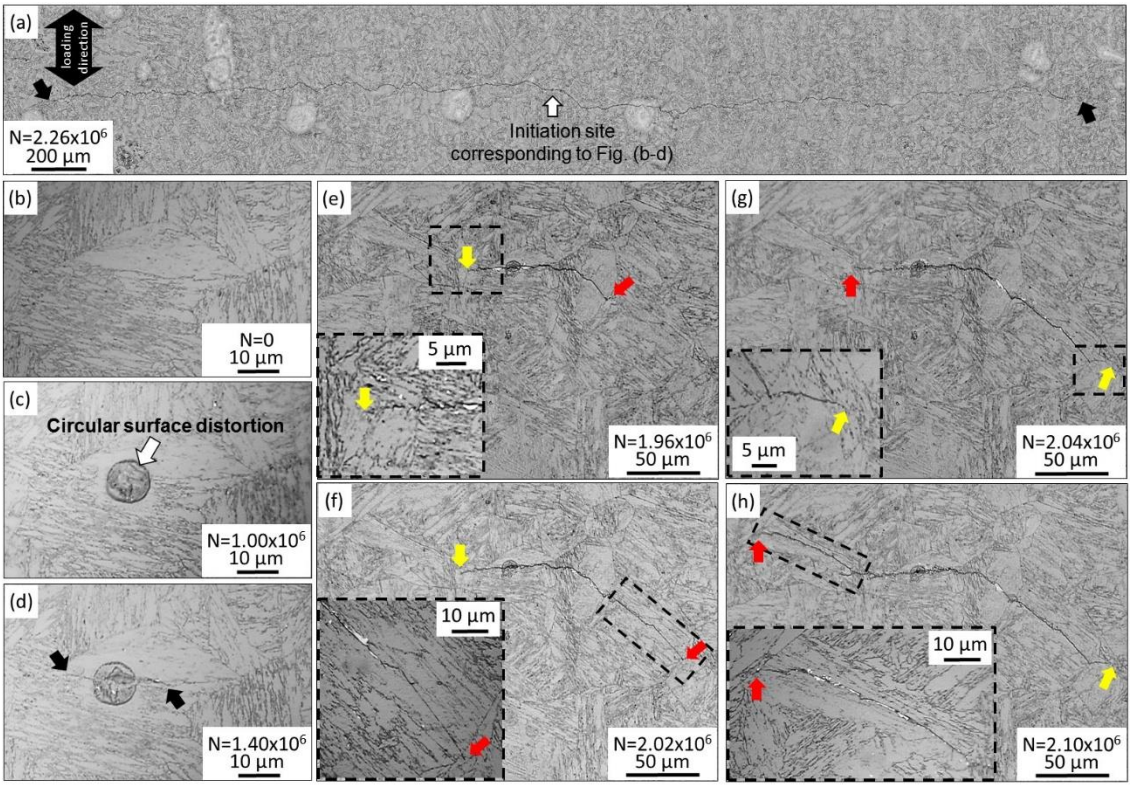

Fig. 4.1. Replica images showing surface fatigue crack behavior for the high cycle fatigue condition at a stress amplitude of 450 MPa with fatigue life of 2.27×10^6 cycles. (a) Fatigue crack propagation path. (b–d) Crack initiation processing. (e–f) and (g–h) Fatigue crack propagated along the laminated structure preferentially indicated by red arrows.

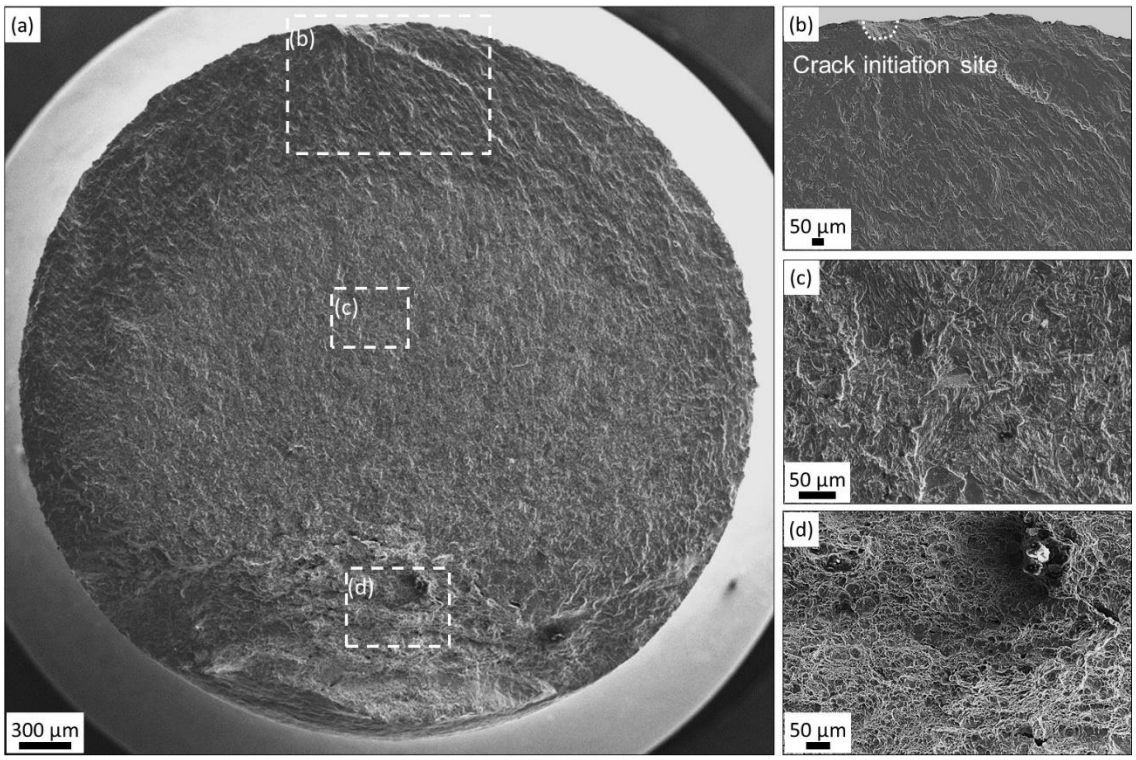

Fig. 4.2. Fracture surface at 450 MPa without brittle fracture phenomenon. (a) Fracture surface. (b) Magnified location near crack initiation. (c) Example of crack propagation area. (d) Final fracture area with a dimple feature.

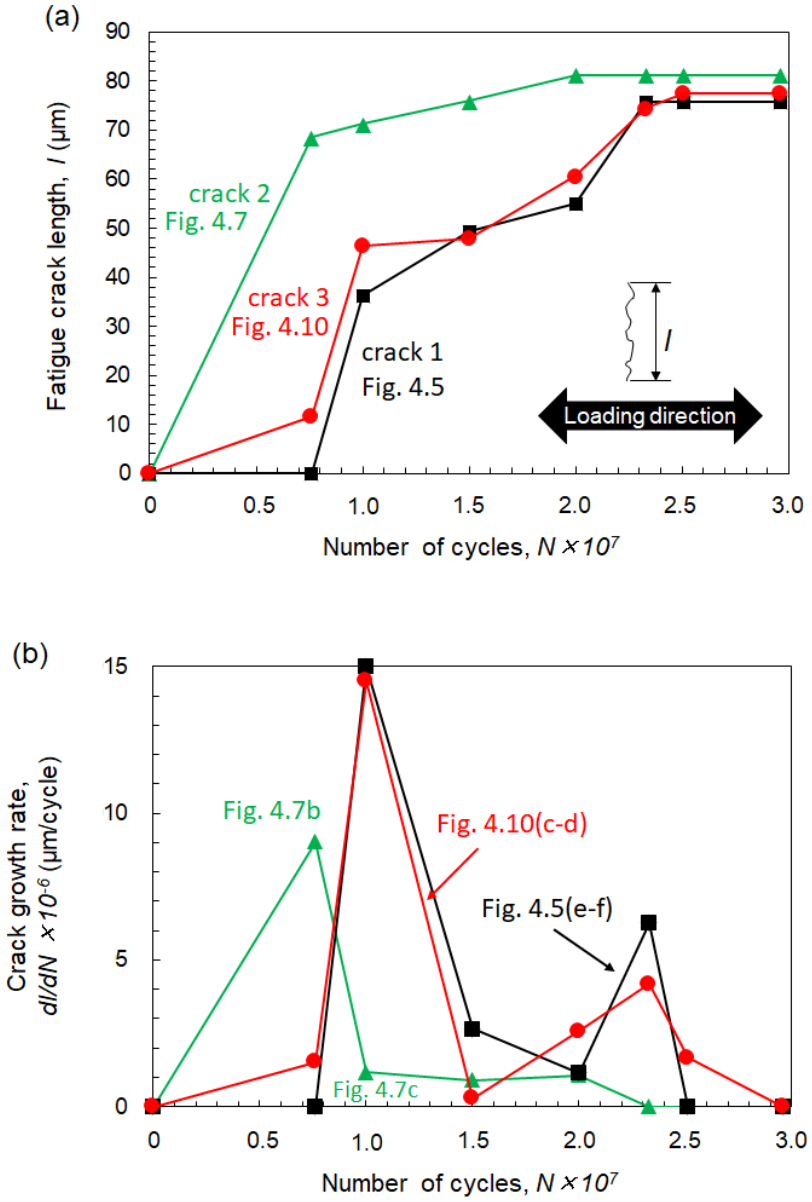

Fig. 4.3. Surface fatigue crack growth data at the fatigue limit of 400 MPa. (a) Fatigue crack length and (b) corresponding crack growth rate plotted against the number of cycles. Some data were extracted from chapter 2.

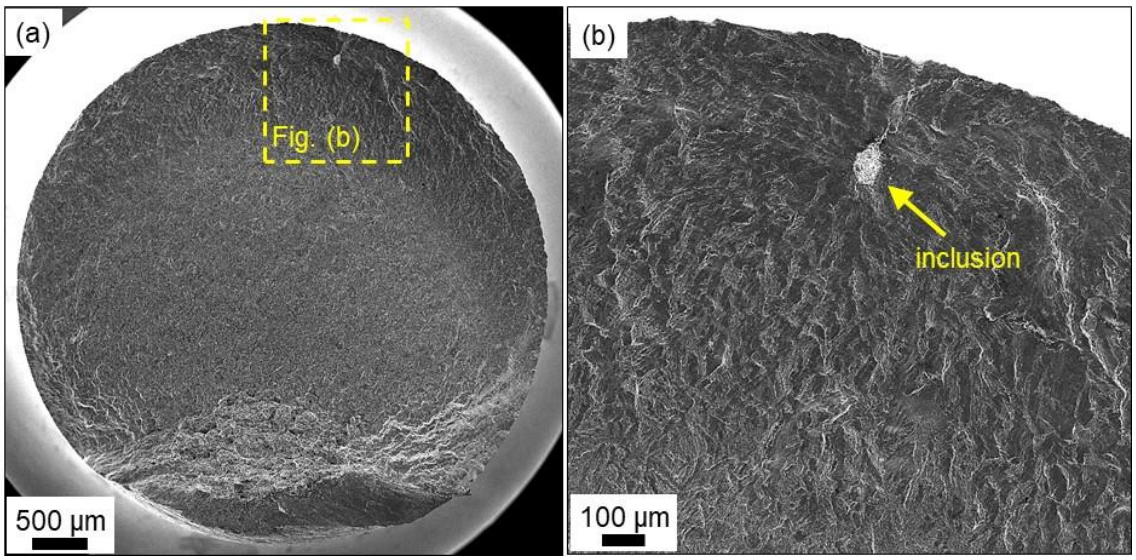

Fig. 4.4. Fracture surface at 400 MPa. (a) Fracture surface and (b) fatigue crack initiation from an internal inclusion.

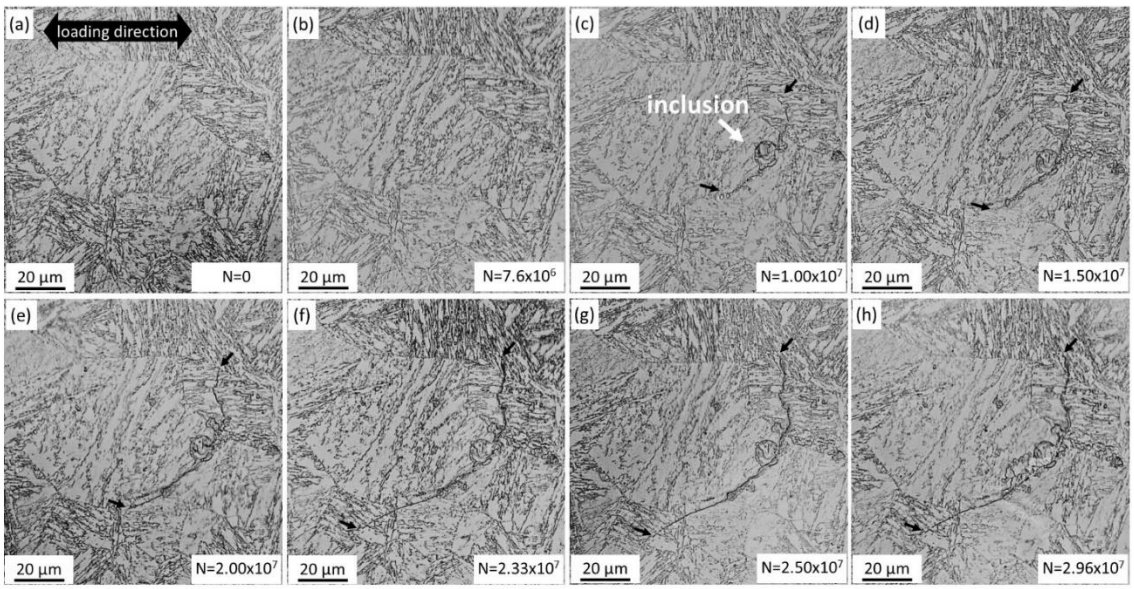

Fig. 4.5. Inverted replica images of non-propagation surface crack 1 at 400 MPa as shown in Fig. 4.3. Initial microstructure before fatigue testing. (b) Microstructure before the crack initiation during testing. (c) Crack initiation. (d–e) Crack propagation. (f–h) Crack non-propagation.

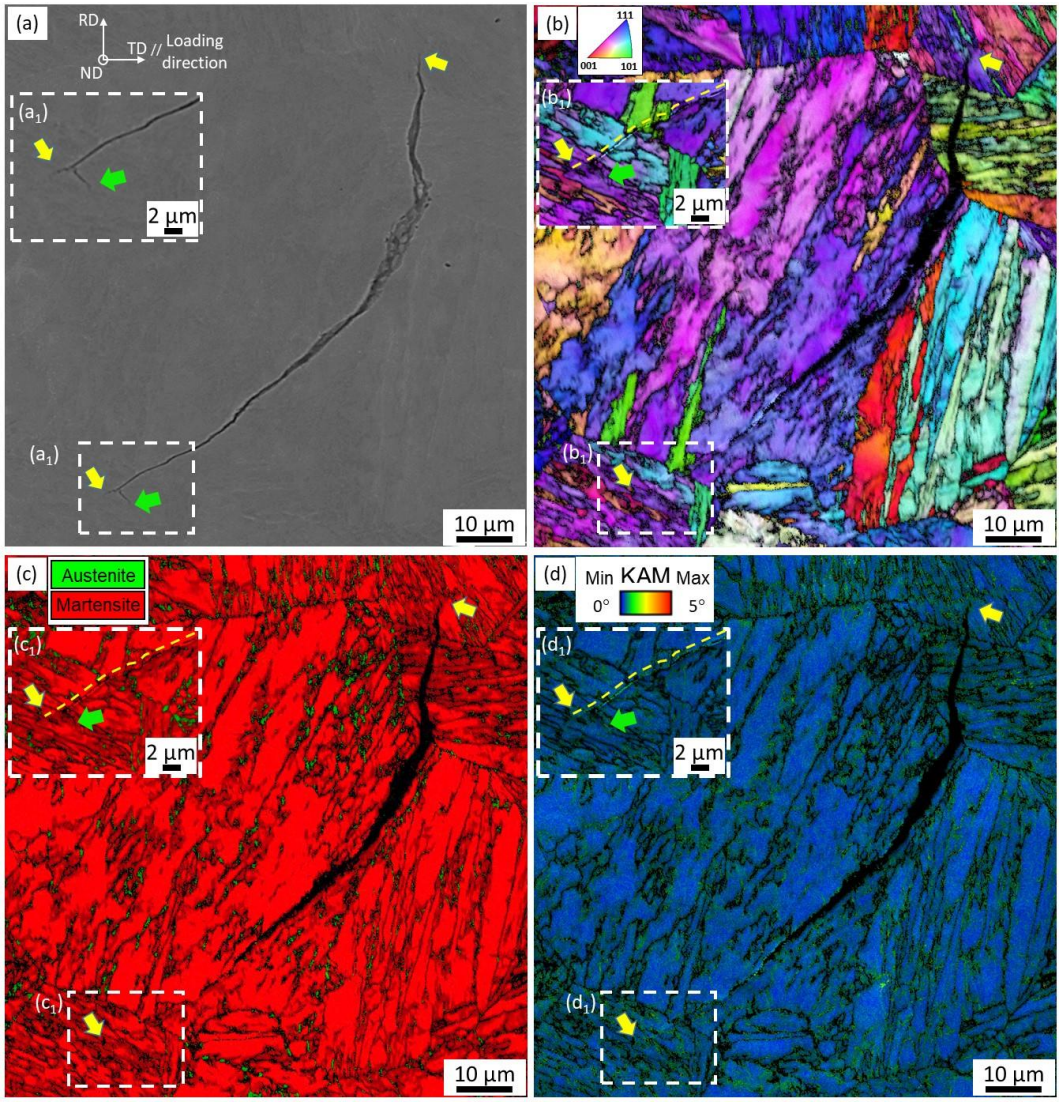

Fig. 4.6. EBSD data for the non-propagating crack at 400 MPa corresponding to Fig. 4.5h. (a) SEM image. (b) ND-IPF map with IQ contrast. (c) Phase map with IQ contrast. (d) KAM with IQ contrast. The yellow arrows indicate fatigue crack tips; the green arrow indicates fatigue crack branching.

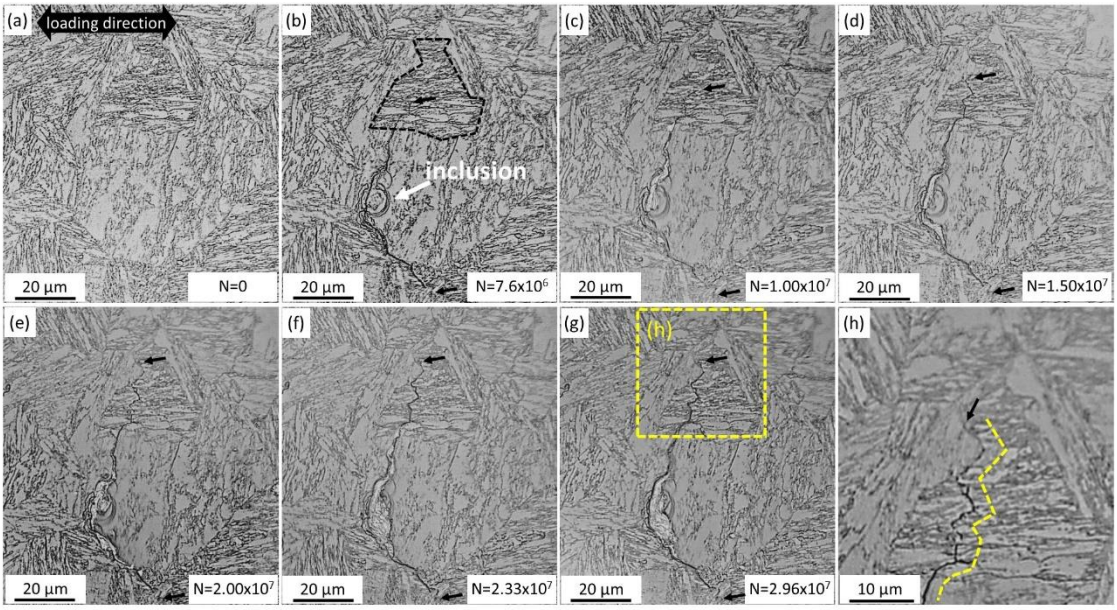

Fig. 4.7. Inverted replica images of non-propagation surface crack 2 at 400 MPa as shown in Fig. 4.3. (a) Initial microstructure before fatigue testing. (b) Fatigue crack initiated at the inclusion and propagated along the boundaries. (c–d) One side of the crack stopped whereas the other side propagated across the lamellar alignment in a zigzag path. (e–g) Crack non-propagation. (h) The magnified crack path with a zigzag pattern is obtained from Fig. 4.7g.

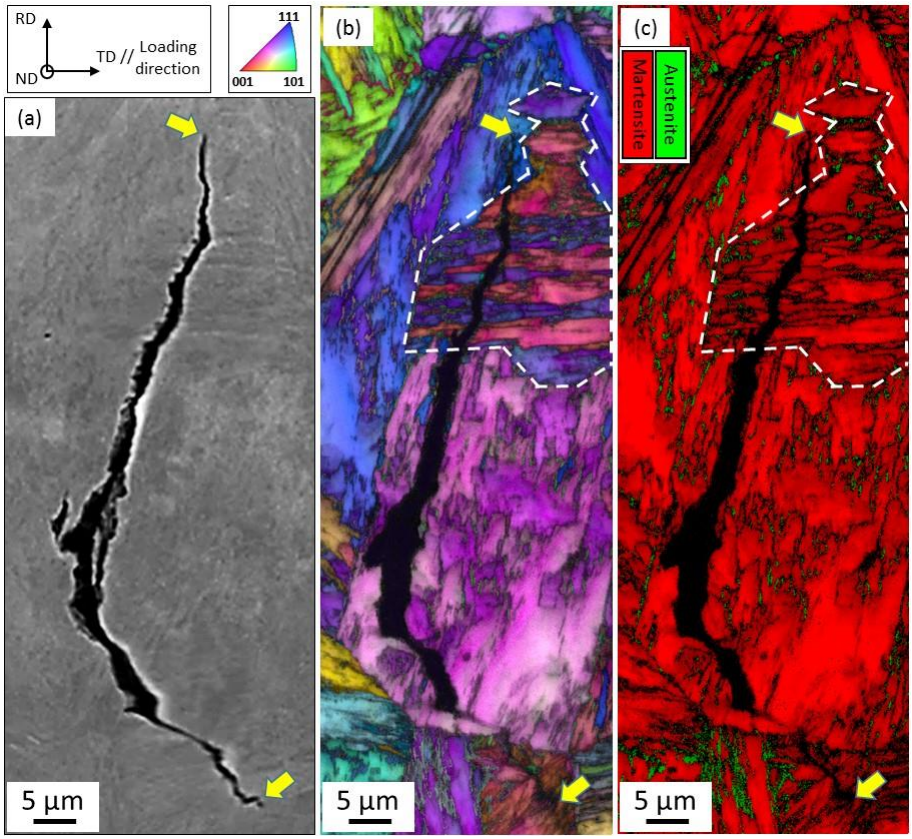

Fig. 4.8. Fatigue crack with non-propagation at 400 MPa corresponding to Fig. 4.7g. The specimen surface was slightly polished after the fatigue test. (a) SEM image, corresponding to the EBSD results (b) ND-IPF map with IQ contrast, and (c) phase map with IQ contrast. Fatigue crack tips are indicated by yellow arrows.

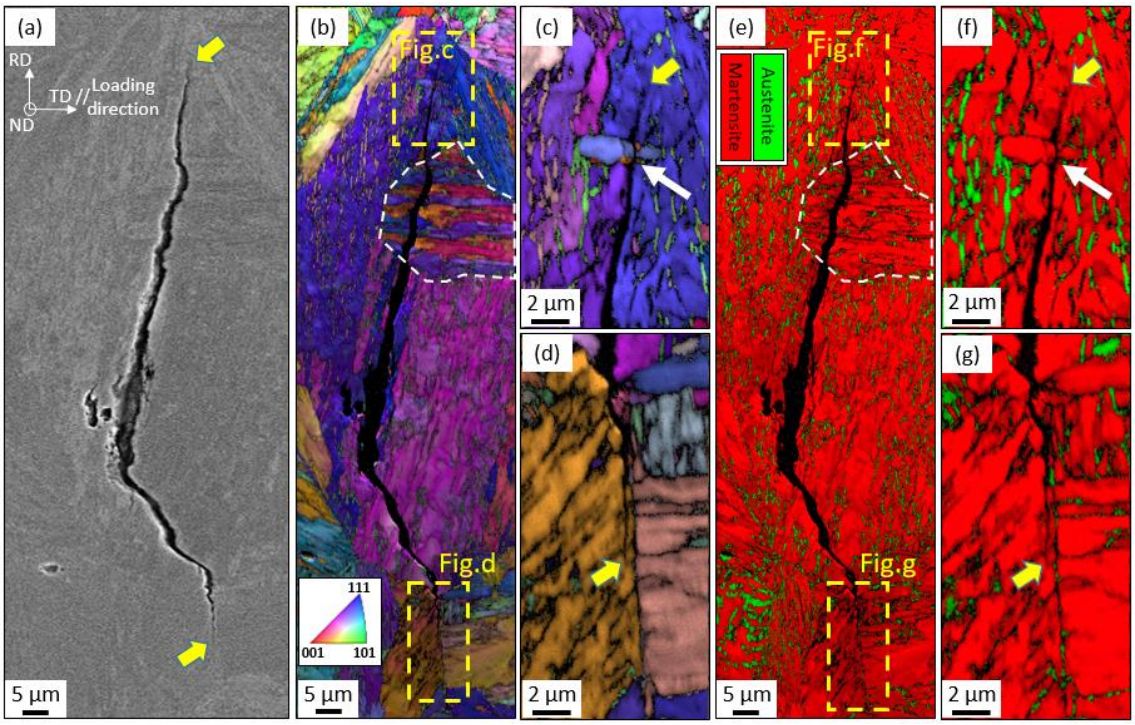

Fig. 4.9. Fatigue crack with non-propagation at 400 MPa polished at a depth of approximately 12 μm from the surface. (a) SEM image. (b) ND-IPF map with IQ. (e) Phase map with IQ. (c–d) and (f–g) Magnified images of the crack tip. The crack tips are indicated by yellow arrows. A deflected crack path was formed when the crack propagated across a grain (indicated by white arrow).

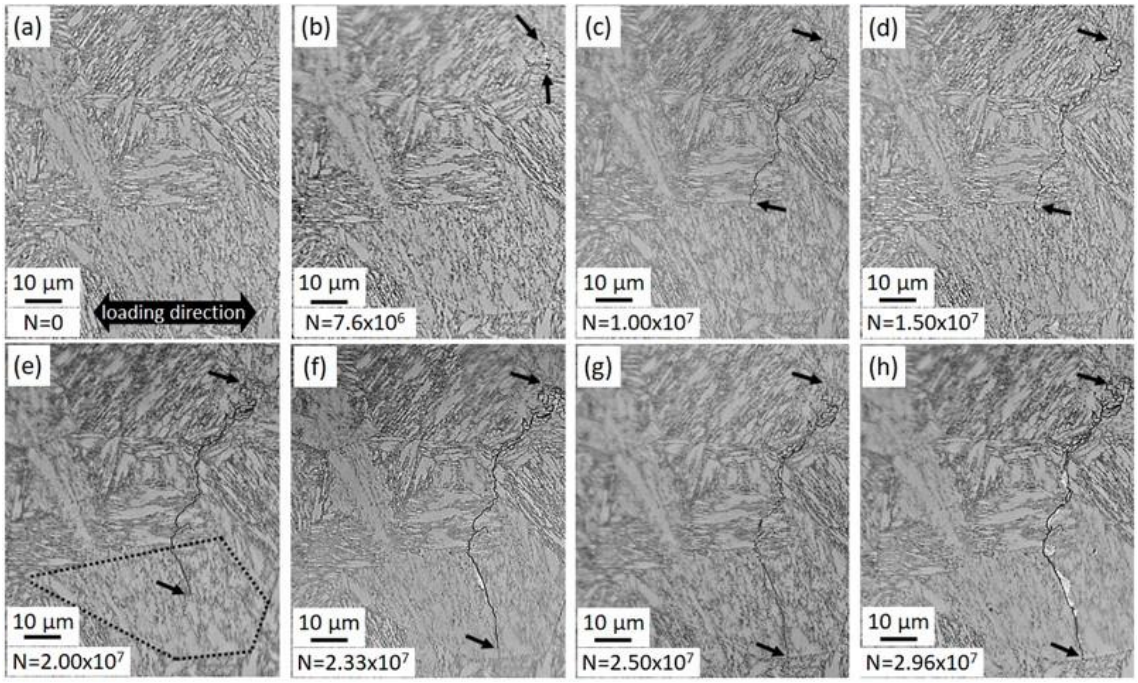

Fig. 4.10. Inverted replica images of non-propagation surface crack 3 at 400 MPa shown in Fig. 4.3. (a) Initial microstructure before fatigue testing. (b) Fatigue crack initiated. (c) Crack propagated along and across the boundaries. (d) Fatigue crack stopped at the maraging martensite packet boundary. (e–f) Fatigue crack continued to propagate across the boundary and along the lamellar alignment. (g–h). Non-propagation crack formed owing to the barrier of the packet boundary.

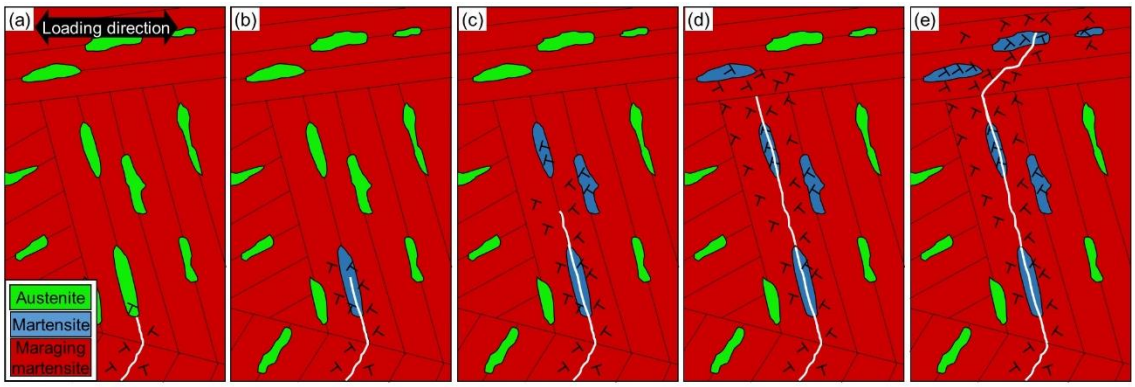

Fig. 4.11. Schematic of crack propagation. Crack path is indicated by a white line. The distribution of dislocation shows the plastic zone at the crack tip. (a) A small crack propagates along the boundaries to approach an austenite with low amount of dislocation. (b) Crack propagates within the austenite, which results in martensitic transformation. (c) Austenite transforms to martensite in advance owing to plastic zone evolution with an increase in crack length. (d) Crack is deflected by the boundary when it attempts to propagate across the maraging martensite along the maximum shear plane. (e) Crack propagates across a few lamellae in a zigzag path.

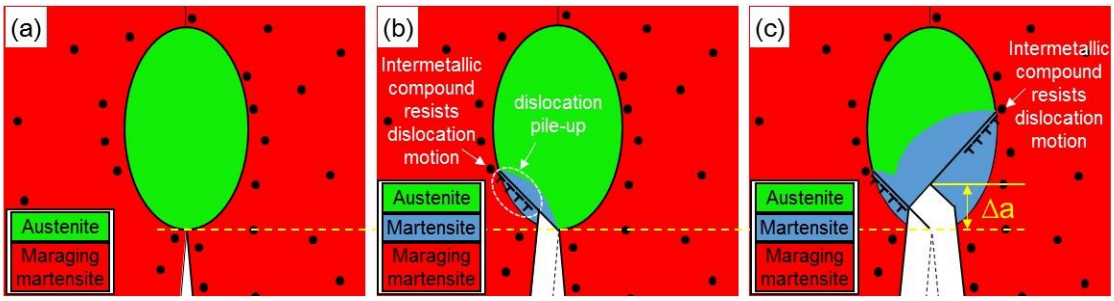

Fig. 4.12. Schematic of the crack blunting process. Stress accommodation ahead of the crack tip. (a) Fatigue crack propagates along the laminates and approaches the austenite. (b–c) Crack-tip-opening-induced martensitic transformation and the intermetallic compounds enable dislocation motion resistance.

CHAPTER 5. Physical mechanism of roughness-induced crack closure failure

5.1 Introduction

Fatigue crack roughness can be formed through microstructure-dependent crack deflection [1], such as preferential crack propagations along twin/grain boundary in austenitic steels [2] and laminated structure in pearlitic steels [3]. As shown in chapter 3 and 4, the hierarchical soft-austenite/hard-martensite laminated microstructure of TRIP-maraging steels guides crack propagation along austenite region, resulting in frequent crack deflection. According to the RICC mechanism, once the crack roughness appears during cyclic loading, asymmetric crack tip deformation causes a mismatch between the crack surfaces [4]. The mismatch causes a premature crack surface contact, assisting crack closure and subsequently decelerating fatigue crack growth rate [5, 6].

Phenomenologically, in TRIP-maraging steels, the increase in austenite size and connectivity was reported to reduce resistance to low-cycle fatigue [7]. Assuming RICC, the fact indicates that the annealing-time-dependent microstructure significantly affects crack deflection/closure behaviors and associated fatigue crack growth rate. However, the crack roughness and associated crack closure with different annealing time have not been thoroughly clarified as shown in Chapter 3 and 4. In addition, the worn crack surface might be a hint to investigate microstructure dependence of the RICC, because

the wear resistance of the crack surface topography is key to maintain the roughness during cyclic loading [8]. As reported previously [7], hardness that is a primary factor affecting wear resistance, is also dependent on annealing time at 873 K. Therefore, the key points in this study is placed on (1) crack roughness and associated crack closure and (2) wear resistance of the fatigue crack region.

For both points (1) and (2), direct observations of fatigue crack in post-mortem specimens are expected to clarify the microstructural effects on the low-cycle fatigue of the TRIP-maraging steel. In order to clarify microstructure-dependent crack roughness including its crack length dependence, only two-dimensional characterization of surface cracks sometimes misleads understanding of its true nature, because of difference in mechanical condition between specimen interior and surface. To solve this problem, we here present the three-dimensional crack roughness features. Then, we discuss the correspondence with microstructure, crack roughness, and hardness-based wear behavior toward revealing significance of RICC in fatigue crack growth of TRIP-maraging steels with different annealing times.

5.2 Experimental procedure and microstructure characterization

In this study, we focus on the low cycle fatigue results obtained from chapter 3, where a 1 h-steel fractured at 800 MPa, and a 8 h-steel fractured at 780. In the fatigue-fractured specimens, sub-cracks of 1100 μm from 1 h-steel and 800 μm from 8 h-steel were selected for crack morphology observations. The Vickers hardness values 15 μm from the fracture surface were measured along the circumference of the specimen. Other details of microstructure characteristics are listed in Table 5.1.

The observation of crack surface concentrated on the roughness evolution along

radial direction by means of mechanical serial sectioning, because the newly formed crack surfaces have rougher morphology, while the crack surfaces far from crack tip show relative smooth topography after a long-term cyclic wear [9]. Prior to polishing, an indent was marked by the Vickers hardness tester under measurement condition of 0.05 kgf, in order to ensure that the observing region is identical during serial sectioning. After each serial sectioning, the crack surface roughness evolution was presented through scanning electron microscopy (SEM) at an accelerating voltage of 20 kV. This microstructure characterization process is shown in Fig. 5.1. In addition, the further analysis of effect of microstructure on crack growth was detected by electron backscatter diffraction (EBSD) measurements at an accelerating voltage of 20 kV and a beam step size of 70 nm. Electron channeling contrast imaging (ECCI) technique was carried out at an accelerating voltage of 30 kV.

5.3 Results

5.3.1 Fractographic viewpoint of the crack roughness

In the chapter 3, fracture surfaces showed smooth topographic feature involving friction scratches (Figs. 3.10a_2 and b_2). This topographic feature is an indirect evidence of occurrence of wear, which is associated with repetitive crack surfaces contact during the fatigue tests. Regarding wear, hardness is an important factor to maintain the crack roughness during long loading cycles. Therefore, the hardness values of 1h- and 8h-steels were measured as listed in Table 5.1.

5.3.2 Three-dimensional characteristics of roughness in 1 h-steel

Figure 5.2a shows a three-dimensional morphology of a fatigue crack of 1 h-steel tested at 800 MPa. The crack propagated until a surface crack length of approximately

1 mm. The three-dimensional zigzag morphology is clearly demonstrated here. The regions outlined by blue dashed line in Fig. 5.2b show a set of relatively low magnification images, which correspond to each section of Fig. 5.2a, respectively. The long crack showed tortuous crack path as indicated by yellow dotted line. Magnified images shown in Figs. 5.2c_1-c_5 indicates micrometer-scale roughness more clearly. Notably, although Figs. 5.2c_1-c_2 show crack zigzag path without crack closure near the specimen surface, the crack surfaces contact each other in the specimen interior. In other words, crack closure occurred near the crack front. Furthermore, the degree of crack surface roughness gradually increased with depth of observation region, and mismatch of the crack surfaces were observed as well. Correspondingly, the frequency of crack closure region increases with increasing depth of the observation region as highlighted by yellow arrows in Figs. 5.2c_3-c_5. This fact indicates that crack roughness significantly contributes to the occurrence of crack closure, i.e., RICC. Particularly, the crack roughness was enhanced by the crack branching as indicated by blue arrows or deflection mainly along the lamellae boundaries in Fig. 5.2c, as well as the crack coalescence shown in Fig. 5.2c_3. The crack propagation with zigzag pattern was not only in the two-dimensional view, but also along radial direction. To be specific, the sub-crack as presented on the surface (Fig. 5.2c_1) is formed by the branched crack propagating beneath specimen surface and then changing the direction towards surface indicated by the white arrows in Fig. 5.2c_2. In addition, Fig. 5.2d quantitatively shows projection distances from center line of each image to respective positions of the crack, which is plotted against serial sectioning depth. For instance, the projection distances in Fig. 5.2c_1 corresponds to the length of yellow arrows. The average height of the crack roughness along the depth direction was approximately 7 μm.

Figure 5.3a shows microstructural crystallographic features of the region outlined by dashed blue lines in Fig. 5.2b$_6$. A crack transgranularly propagates across numerous maraging martensite blocks with zigzag path. The KAM map shows that the plastic deformation is mainly distributed along grain boundaries acting a preferential formation site of the retained austenite, while maraging martensite interior barely shows damage (Fig. 5.3b). Furthermore, we note coarse laths indicated by white arrows in Fig. 5.3b. Figure 5.3c$_1$ shows an ECC image including the coarse laths. In one of coarse lath regions as shown in Fig. 5.3c$_2$, the crack surfaces show significant asymmetric topography. A side of crack surfaces presents a submicrometer-scale serration-like roughness, while the other side shows a smooth topography caused by wear. Another coarse lath region also shows worn crack surfaces as indicated by red arrow in Fig. 5.3c$_3$, which cannot contribute to crack closure. The region near the worn surface presents coarse and thin laths as shown in Fig. 5.3c$_4$. The coarse lath martensite shows a large amount of lattice distortion, while the thin lath contained relatively less lattice distortion.

5.3.3 Three-dimensional characteristics of roughness in 8 h-steel

Figure 5.4a shows a the three-dimensionally zigzag fatigue crack with 800 μm length in 8 h-steel tested at 780 MPa. At different depths, the identical region outlined by yellow lines in Fig. 5.4b is magnified to exhibit a crack mainly along lamellar alignment (Fig. 5.4c), which results in a micrometer-scale crack surface roughness. Notably, the configurations of the crack do not show grain-size-scale change with specimen depth from surface to 26 μm as shown in Figs. 5.4c$_1$-c$_3$. Significant changes in crack shape was observed in the curvature of the crack surface and the presence of submicrometer-scale roughness as indicated by yellow dashed circle. The

submicrometer-scale roughness could remain because wear did not occur at this location owing to crack closure at neighboring place. A grain-size-scale change appeared when the specimen was ground from 26 to 40 μm in depth as shown in Fig. 5.4c_4, because the crack is deflected by branched crack indicated by blue dashed line. Again, no grain-size-scale change in crack shape was observed from 40 to 51 μm in depth. The presence of roughness causes crack closure as indicated by yellow arrows, irrespective of depth along the radial direction. Figure 5.4d shows roughness profiles along the radial direction. The parts of the fluctuant segments show an average crack roughness height of around 9.0 μm.

Figures 5.5a_1-a_3 show the evolution of the micrometer-scale roughness associated with crack coalescence. A microstructural feature and plastic strain distribution of the region where crack coalescence occurred on the surface is characterized after the serial sectioning process, as shown in Figs. 5.5b and 5.5c. The ND-IPF map with IQ contrast mainly presents an interlamellar crack, and the relevant KAM map shows an extensive plastic deformation.

5.4 Discussion

5.4.1 Roughness originating from crack propagation

In low cycle fatigue, the high applied-stress leads to transformation from retained austenite to fresh martensite at early fatigue stage. The macroscopic yielding causes multi-crack initiations at fresh martensite and pre-existing defects such as inclusion (Fig. 5.6a_1 and b_1). Subsequently, the initial cracks preferentially propagate along lamellar alignment, because (i) the fresh martensite inherits the original austenite distribution pattern, which is located at prior austenite boundary and various maraging martensite

boundaries [10], (ii) the fresh martensite is softer than maraging martensite owing to the absence of intermetallic compounds [7], and (iii) the intermetallic compounds contribute to plastic deformation resistance in maraging martensite by pinning dislocation [11, 12]. Thus, crack surface exhibits a micrometer-scale roughness. In 1 h-steel, the highly deformed fresh martensite will cause a local nm-scale roughness due to the volume dilatation [7]. With increasing crack length, the stress intensity factor is enhanced to a certain value that assists crack to break through the maraging martensite blocks as shown in Fig. 5.3a (schematically in Figs. 5.6a_2 and b_2). In this situation, cracks show submicrometer-scale rough surfaces due to the different orientation of the blocks. In addition, the submicrometer-scale roughness is also observed inside coarse lath of 1 h-steel (Fig. 5.3c_2), which is formed by the mix-mode I+II when the slip plan is diagonal to the loading direction. Furthermore, crack coalescence also contributes the micrometer-scale roughness as shown in Figs. 5.2c_3 and 5.5a_1-a_2 (schematically in Figs. 5.6a_3 and b_3). Thus, both steels have similar crack surface roughness pattern in terms of interlamellar, transgranular and coalescing crack, which act as macroscopic factor for crack closure. The microscopic factor stems from the asymmetric crack wake plasticity i.e. mismatched crack surfaces [13, 14], which results from inhomogeneous microstructure resistance to dislocation motion. When crack tip deformation drives crack surface shift, those factors contribute to crack closure i.e. RICC and associated deceleration of growth rate [5]. However, owing to the crack surface contact accompanied by friction, the roughness of fracture surface was inevitably worn as shown in chapter 3 (Figs. 3.10a_2 and b_2). Therefore, in the following, evolution of crack surface wear will be described.

5.4.2 Effect of hardness on crack roughness: a viewpoint of wear

As mentioned above, the transgranular crack across laminated microstructure has a more finely zigzag path (Figs. 5.2c_3 and 5.4c_2), compared to the interlamellar cracking. Although the frequent crack deflection contributes to crack closure, the inevitable wear progressively reduces the roughness height to weaken RICC as schematically shown in Fig. 5.7. In loading process, the advancing crack tip generates new submicrometer-scale roughness (Fig. 5.7a). During unloading, the crack surface asperities prematurely contact and flaws are remained. With the mismatched surfaces reciprocal sliding under the crack tip driving, interaction force facilitates the flaws growth (Fig. 5.7b). Finally, asperities are fractured to become smooth topography (Fig. 5.7c). In the following crack re-sharpening process, new flaws are introduced on the smooth surface by asperities. The subsequently shifting crack surface asperities stretches the flaws to leave scratches (Fig. 5.7d). Therefore, when roughness is reduced to a certain height that both crack surfaces cannot locally contact each other, RICC becomes impossible.

According to the results, two steels show a distinct degree of worn surfaces (Figs. 5.2 and 5.4). Particularly, the submicrometer-scale roughness can be obviously observed in 1 h-steel, instead of 8 h-steel. This reveals that 1 h-steel has stronger wear resistance than 8 h-steel, because of its higher hardness particularly in the vicinity of crack (Table 5.1). The hardness-dependence of wear resistance detected by A.J. Perez-Unzueta and J.H. Beynon [15], showed that, during pure sliding wear tests, the pearlitic rail steel has higher value of hardness by decreasing the lamellar spacing and can effectively reduce the wear, because the high hardness stems from high work-hardening. In the dry wear test, J.Kalousek et al. [16] reported that both tempered martensite and bainite steels showed improved wear resistance through increasing the hardness. These studies

demonstrated that the hardness is crucial for wear resistance.

The hardness is associated with the heat treatment in the present steels. Here, it should be noted that the austenite reversion process is under over-annealing [17-19]. In the previous work [7], increasing austenite grain size with annealing time results in softening austenite, i.e. the austenite in 1 h-steel is harder than that in 8 h-steel. Correspondingly, the hardness of fresh martensite transformed from austenite in 1 h-steel is higher than that in 8 h-steel. In terms of maraging martensite, the hardness is reduced with over-annealing time [20-23]. This is attributed to the dislocations re-arrangement and associated decrement of dislocation density in maraging martensite. Also, the intermetallic compound re-arrangement and coarsening decrease its density, and thus the interparticle spacing increases. Therefore, during plastic strain, dislocation line easily tends to loop around the particles in 8 h-steel, resulting in deterioration in impeding effect on dislocation motion and finally softening the maraging martensite. As presented by KAM maps, in 8 h-steel, the maraging martensite suffers from severe plastic deformation, while that in 1 h-steel shows barely plastic deformation except in the vicinity of crack (Figs. 5.3b and 5.5c). This reflects that the maraging martensite in 1 h-steel has high hardness and effectively resists plastic deformation. Therefore, on the overview of point, the 1 h-steel is harder than 8 h-steel. Correspondingly, the 1 h-steel possesses stronger wear resistance and associated long-term effective RICC.

5.4.3 Influence of coarse lath martensite on RICC

In the 1 h-steel, Fatigue crack across martensite blocks involves coarse and thin lathes. The hardness of coarse lath is lower than that of thin lath [24], resulting in accelerating crack growth in the coarse lath region. Since the plastic deformation in

coarse lath is preferentially along slip plane [25], when the slip plane is diagonal to the loading direction, fatigue crack across coarse lath easily forms a submicrometer-scale serration-like path by mix-mode I+II (Fig. 5.3c$_2$). Thus, this submicrometer-scale roughness contributes to crack closure. However, the wear causes an asymmetric worn surfaces probable due to the inhomogeneous hardness.

Similar case also occurred at another coarse lath region where a crack propagated with a zigzag pattern path. The wear also destroys the matched fracture surface roughness, leaving asymmetric crack flanks. Specifically, the upper crack surface was smoother (region indicated by red arrow in Fig. 5.3c$_3$). At the same side of crack, the thin lath showed a bright contrast in ECC image, irrespective of crystallographic orientation (Fig. 5.3c$_3$). Since grains with optimized surface orientation for Bragg's condition must show dark contrast, the orientation-independent bright contrast indicates that the thin laths contain high lattice defect density such as dislocation. In contrast, a partial region of coarse lath showed dark contrast and the other region particularly near the lath boundary showed bright contrast. With the same context above, the contrast gradient indicates lattice distortion, which is plausibly attributed to dislocation accumulation near the lath boundary. In other words, plastic strain heterogeneously evolved in the coarse lath, arising from the low density of intrinsic dislocation. Generally, crystallographic defect such as dislocation and grain boundary is preferential nucleation site for precipitation particles. Thus, the amount of particle is less due to the less dislocation in coarse lath. Accordingly, at high stress amplitude, the pinning effect of particle on motion of large amount of the newly-generated dislocation is limited. Finally, dislocation distribution becomes inhomogeneous, further affecting crystal strength. At unloading process, the asymmetric crack surfaces tend to return to original position and

form a cavity, instead of crack closure, resulting in RICC failure. Thus, the influence of coarse lath martensite on RICC is significant detrimental and acts as potential crack path, because of low hardness and rapid wear consumption. In this regard, the high hardness appears to be especially important with respect to high wear resistance and associated long-term effective RICC.

The unpolished surface of 8 h-steel shows RICC while 1 h-steel does not show that. Instead, this one-sided situation cannot judge that 8 h-steel has high degree of roughness. Based on the above results, internal crack behavior presented by serial sectioning uncovered that two-dimensional characterization easily misleads understanding. In fact, crack surfaces present different roughness in different depth owing to the wear. Furthermore, since the wear related to the hardness, the 'soft' 8 h-steel had a larger range of worn crack surface than the 1 h-steel. Accordingly, the assessment on RICC through three-dimensional investigation is more comprehensive.

5.5 Section Conclusion

The different heat treatment generates different microstructure with various hardness that influences fatigue crack growth and associated roughness. The roughness evolution is investigated through serial sectioning mechanical polishing. The conclusion is as follows:

(1). Low-cycle fatigue resistance in 1 h-steel is superior to that of 8 h-steel. This is not only due to the low austenite connectivity, but also the strong wear resistance. 8 h-steel mainly shows interlamellar cracking due to the high austenite connectivity, while 1 h-steel shows transgranular crack across laminated microstructure that results in a submicrometer-scale roughness.

(2). Owing to the existing wear during crack surfaces contacting each other, the crack surfaces far from crack front become smooth, while the surfaces near the crack front is rough. This morphology evolution is more evident in the ‘hard’ 1 h-steel, compared to the ‘soft’ 8 h-steel that shows smooth crack surfaces in most regions, because the hardness determines the wear resistance. Therefore, the 1 h-steel has long-term effective RICC.

(3). In 1 h-steel, the roughness in coarse lath is worn easier than that in thin lath. Thus, the influence of coarse lath martensite on RICC is significant detrimental and acts as potential crack path, because of low hardness and rapid wear consumption.

5.6 References

[1] S. Suresh, R.O. Ritchie, A geometric model for fatigue crack closure induced by fracture surface roughness, Metallurgical Transactions A 13(9) (1982) 1627-1631.

[2] Y.-B. Ju, M. Koyama, T. Sawaguchi, K. Tsuzaki, H. Noguchi, In situ microscopic observations of low-cycle fatigue-crack propagation in high-Mn austenitic alloys with deformation-induced ε-martensitic transformation, Acta Materialia 112 (2016) 326-336.

[3] G.T. Gray, J.C. Williams, A.W. Thompson, Roughness-Induced Crack Closure: An Explanation for Microstructurally Sensitive Fatigue Crack Growth, Metallurgical Transactions A 14(2) (1983) 421-433.

[4] J. Pokluda, R. Pippan, Analysis of roughness-induced crack closure based on asymmetric crack-wake plasticity and size ratio effect, Materials Science and Engineering: A 462(1) (2007) 355-358.

[5] S. Suresh, Crack deflection: Implications for the growth of long and short fatigue cracks, Metallurgical Transactions A 14(11) (1983) 2375-2385.

[6] R. Ritchie, S. Suresh, Some considerations on fatigue crack closure at near-threshold stress intensities due to fracture surface morphology, Metallurgical Transactions A 13(5) (1982) 937-940.

[7] Z. Zhang, M. Koyama, M.M. Wang, K. Tsuzaki, C.C. Tasan, H. Noguchi, Effects of lamella size and connectivity on fatigue crack resistance of TRIP-maraging steel, International Journal of Fatigue 100, Part 1 (2017) 176-186.

[8] N. Gates, A. Fatemi, Friction and roughness induced closure effects on shear-mode crack growth and branching mechanisms, International Journal of Fatigue 92 (2016) 442-458.

[9] T.S. Gross, D.A. Mendelsohn, On the effect of crack face contact and friction due to fracture surface roughness in edge cracks subjected to external shear, Engineering Fracture Mechanics 31(3) (1988) 405-420.

[10] M.M. Wang, C.C. Tasan, D. Ponge, A. Kostka, D. Raabe, Smaller is less stable: Size effects on twinning vs. transformation of reverted austenite in TRIP-maraging steels, Acta Materialia 79 (2014) 268-281.

[11] D. Raabe, D. Ponge, O. Dmitrieva, B. Sander, Designing ultrahigh strength steels with good ductility by combining transformation induced plasticity and martensite aging, Advanced Engineering Materials 11(7) (2009) 547-555.

[12] J. Millán, S. Sandlöbes, A. Al-Zubi, T. Hickel, P. Choi, J. Neugebauer, D. Ponge, D. Raabe, Designing Heusler nanoprecipitates by elastic misfit stabilization in Fe–Mn maraging steels, Acta Materialia 76 (2014) 94-105.

[13] R. Pippan, G. Strobl, H. Kreuzer, C. Motz, Asymmetric crack wake plasticity – a reason for roughness induced crack closure, Acta Materialia 52(15) (2004) 4493-4502.

[14] J. Pokluda, Dislocation-based model of plasticity and roughness-induced crack closure, International Journal of Fatigue 46(Supplement C) (2013) 35-40.

[15] A.J. Perez-Unzueta, J.H. Beynon, Microstructure and wear resistance of pearlitic rail steels, Wear 162(Part A) (1993) 173-182.

[16] J. Kalousek, D.M. Fegredo, E.E. Laufer, The wear resistance and worn metallography of pearlite, bainite and tempered martensite rail steel microstructures of high hardness, Wear 105(3) (1985) 199-222.

[17] D. Raabe, D. Ponge, O. Dmitrieva, B. Sander, Nanoprecipitate-hardened 1.5 GPa steels with unexpected high ductility, Scripta Materialia 60(12) (2009) 1141-1144.

[18] O. Dmitrieva, D. Ponge, G. Inden, J. Millán, P. Choi, J. Sietsma, D. Raabe, Chemical gradients across phase boundaries between martensite and austenite in steel studied by atom probe tomography and simulation, Acta Materialia 59(1) (2011) 364-374.

[19] F. Moszner, E. Povoden-Karadeniz, S. Pogatscher, P.J. Uggowitzer, Y. Estrin, S.S.A. Gerstl, E. Kozeschnik, J.F. Löffler, Reverse α′→γ transformation mechanisms of martensitic Fe–Mn and age-hardenable Fe–Mn–Pd alloys upon fast and slow continuous heating, Acta Materialia 72(Supplement C) (2014) 99-109.

[20] L.K. Singhal, J.W. Martin, The mechanism of tensile yield in an age-hardened steel containing γ′ (ordered Ni3Ti) precipitates, Acta Metallurgica 16(7) (1968) 947-953.

[21] H. Shercliff, M. Ashby, A process model for age hardening of aluminium alloys—I. The model, Acta Metallurgica et Materialia 38(10) (1990) 1789-1802.

[22] F. Moszner, A.S. Sologubenko, M. Schinhammer, C. Lerchbacher, A.C. Hänzi, H. Leitner, P.J. Uggowitzer, J.F. Löffler, Precipitation hardening of biodegradable Fe–Mn–Pd alloys, Acta Materialia 59(3) (2011) 981-991.

[23] J. Millán, D. Ponge, D. Raabe, P. Choi, O. Dmitrieva, Characterization of Nano-Sized Precipitates in a Mn-Based Lean Maraging Steel by Atom Probe Tomography, steel research international 82(2) (2011) 137-145.

[24] L. Morsdorf, C.C. Tasan, D. Ponge, D. Raabe, 3D structural and atomic-scale analysis of lath martensite: Effect of the transformation sequence, Acta Materialia 95 (2015) 366-377.

[25] L. Morsdorf, O. Jeannin, D. Barbier, M. Mitsuhara, D. Raabe, C.C. Tasan, Multiple mechanisms of lath martensite plasticity, Acta Materialia 121 (2016) 202-214.

5.7 Tables and figures

Table 5.1. Microstructure size of 1h- and 8h-steels.
Vickers hardness tests were conducted at 0.05 kgf.

Annealing time	Prior austenite grain size (μm)	Packet size (μm)	Block thickness (μm)	Lath thickness (μm)	HV before tests	HV near the fracture surface
1 hour	30	10	3	0.8	356	468
8 hour	29.7	9.7	2.7	0.5	261	329

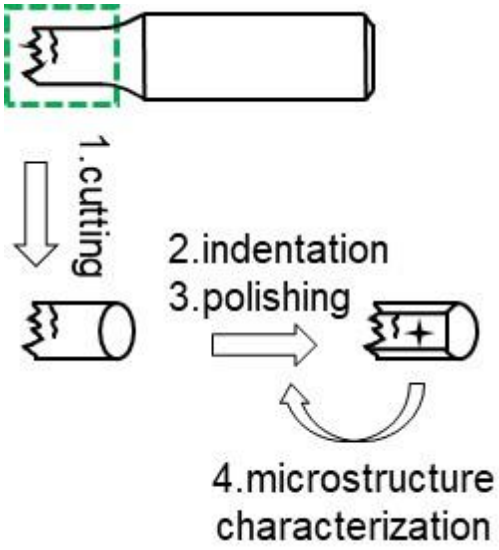

Fig 5.1. Three-dimensional microstructure characterization process with serial sectioning.

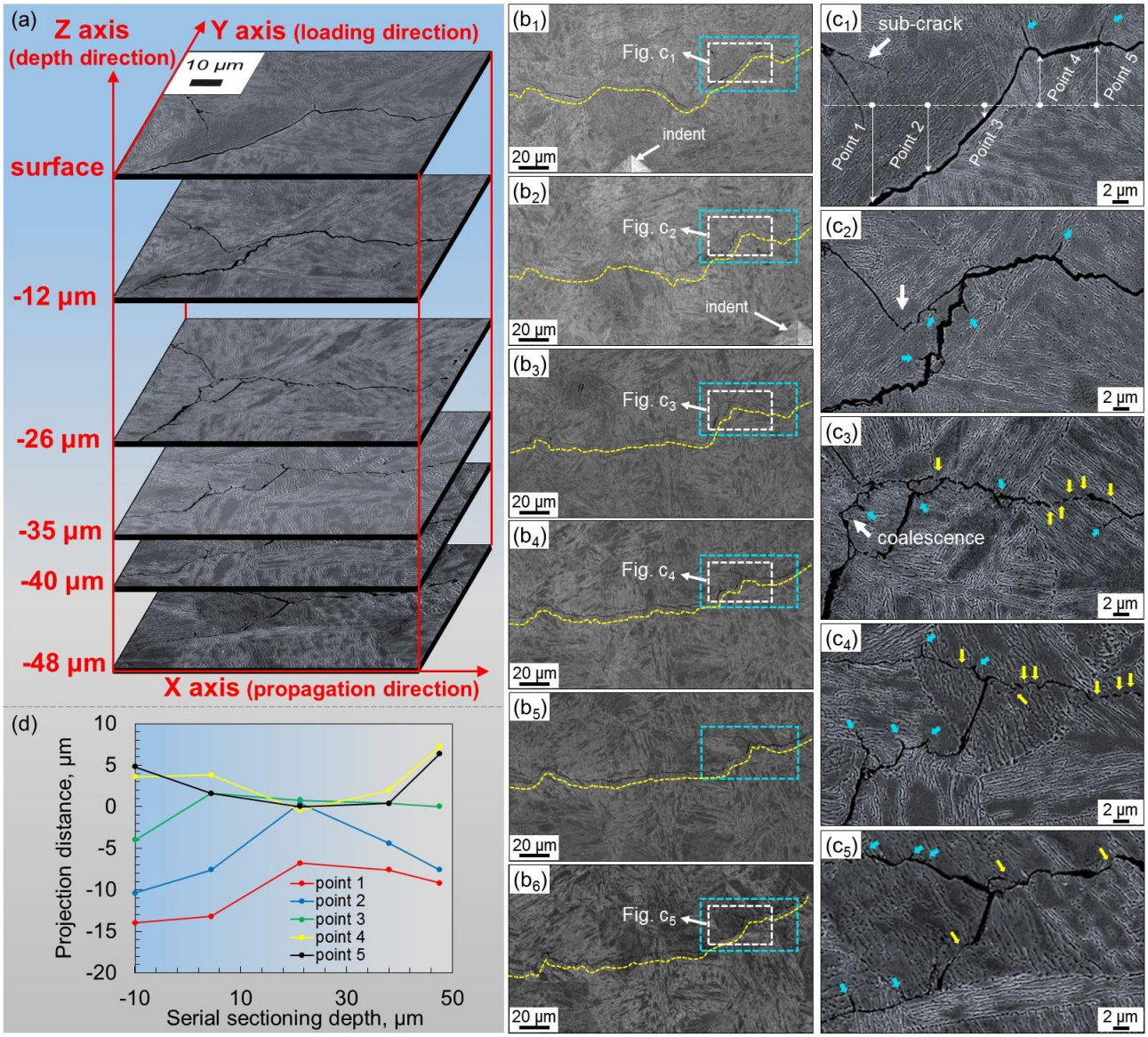

Fig. 5.2. 1h-steel at 800 MPa with fatigue life of 2.23×10^4 cycles. (a) Three-dimensional microstructure characterization by serial sectioning. (b) Long zigzag crack. The regions outlined by blue and white dashed lines are magnified as shown in Fig. 5.2a and Fig. 5.2c. (c) The evolution of crack surface roughness with different depths. The blue and yellow arrows indicate crack branching and crack closure, respectively. (d) Projection distance from center line of each image to crack, is plotted against serial sectioning depth. The average height of crack roughness is approximately 7 μm.

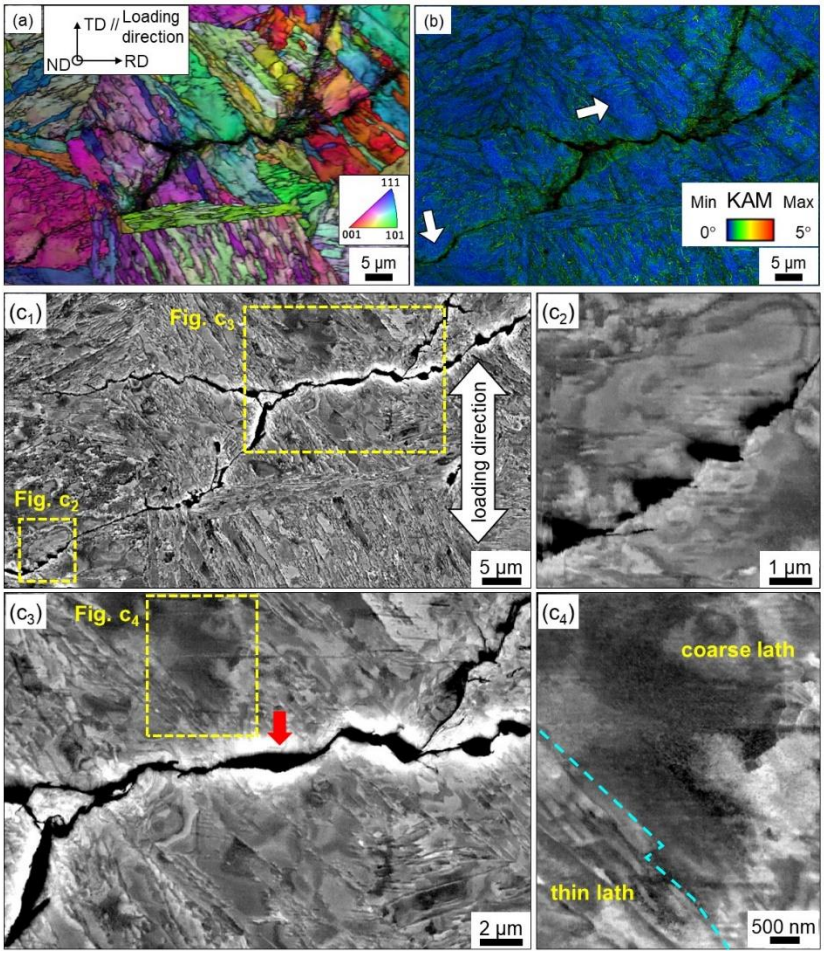

Fig. 5.3. Microstructure characterization of 1h-steel at 800 MPa obtained after the failure at 2.23×10^4 cycles, corresponding to the region outlined by blue dashed line in Fig. 5.2b$_6$. EBSD data is shown by (a) ND-IPF map with IQ contrast, and (b) KAM map. The white arrows indicate coarse laths. (c$_1$) Identical zigzag crack is characterized by ECCI technique. (c$_2$-c$_3$) Crack surfaces show asymmetric roughness. The red arrow indicates the worn surfaces. (c$_4$) A region near worn surface includes coarse and thin laths.

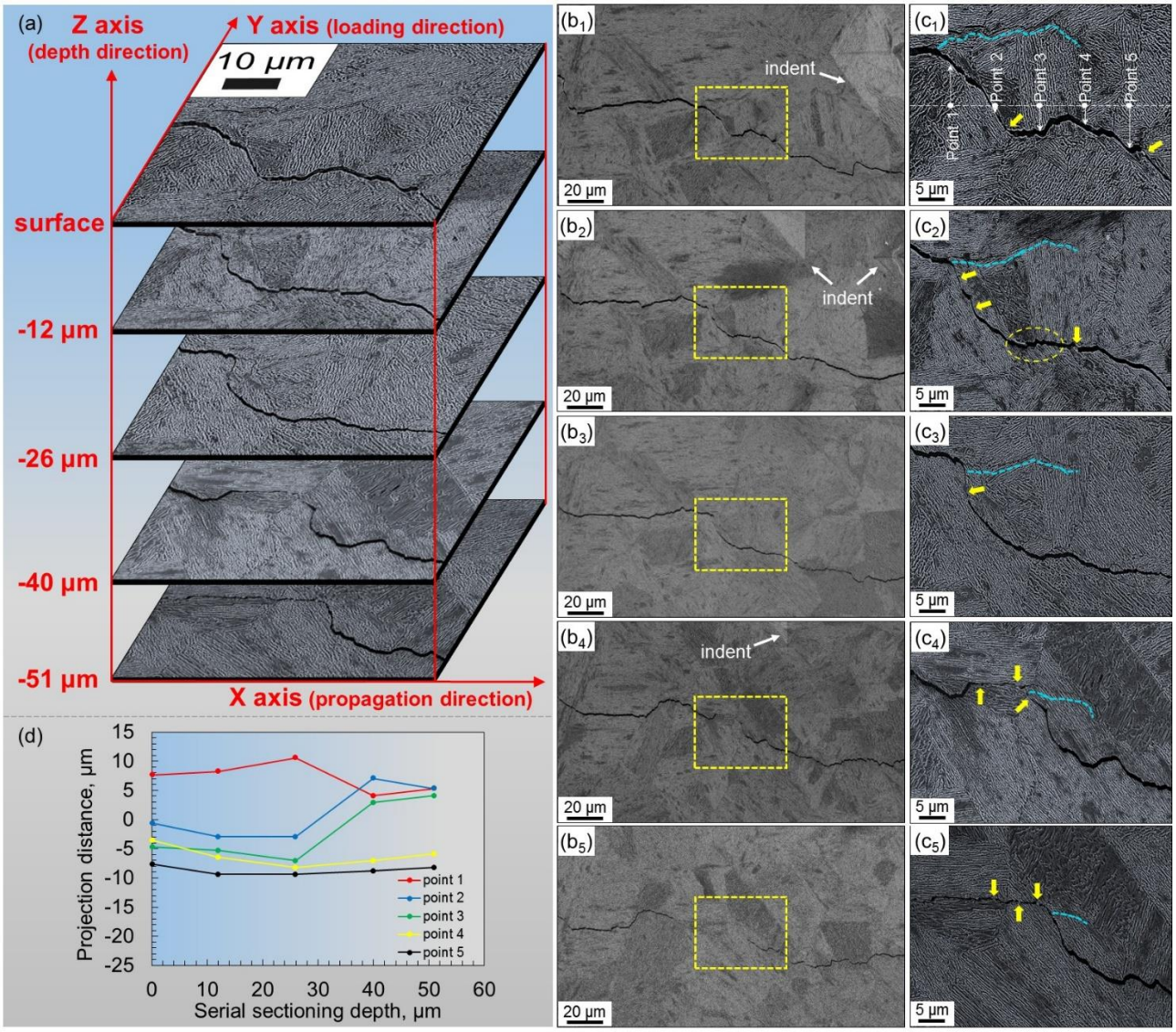

Fig. 5.4. 8h-steel at 780 MPa with fatigue life of 1.61×10^4 cycles. (a) Three-dimensional microstructure characterizations by serial sectioning. (b) The local regions indicated by yellow dashed lines correspond to Figs 5.4a and 5.4c. (c) Crack propagation along lamellar alignment caused crack closure indicated by yellow arrows. (d) Projection distance from center line of each image to crack, is plotted against serial sectioning depth.

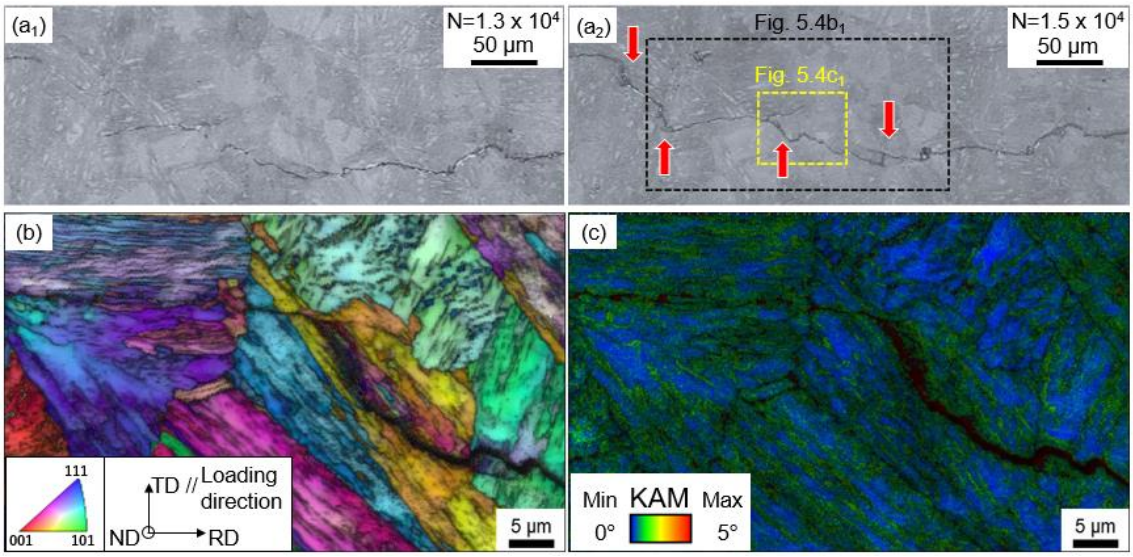

Fig. 5.5. Fatigue crack propagation path of 8 h-steel at 780 MPa. (a_1-a_2) A set of inverted replica images shows that crack coalescences cause the micrometer-scale roughness indicated by the red arrows. After serial sectioning to -51 µm, microstructure of yellow outline in Fig. 5.5a_2 is characterized by EBSD as presented in (b) ND-IPF map with IQ contrast and (c) KAM map.

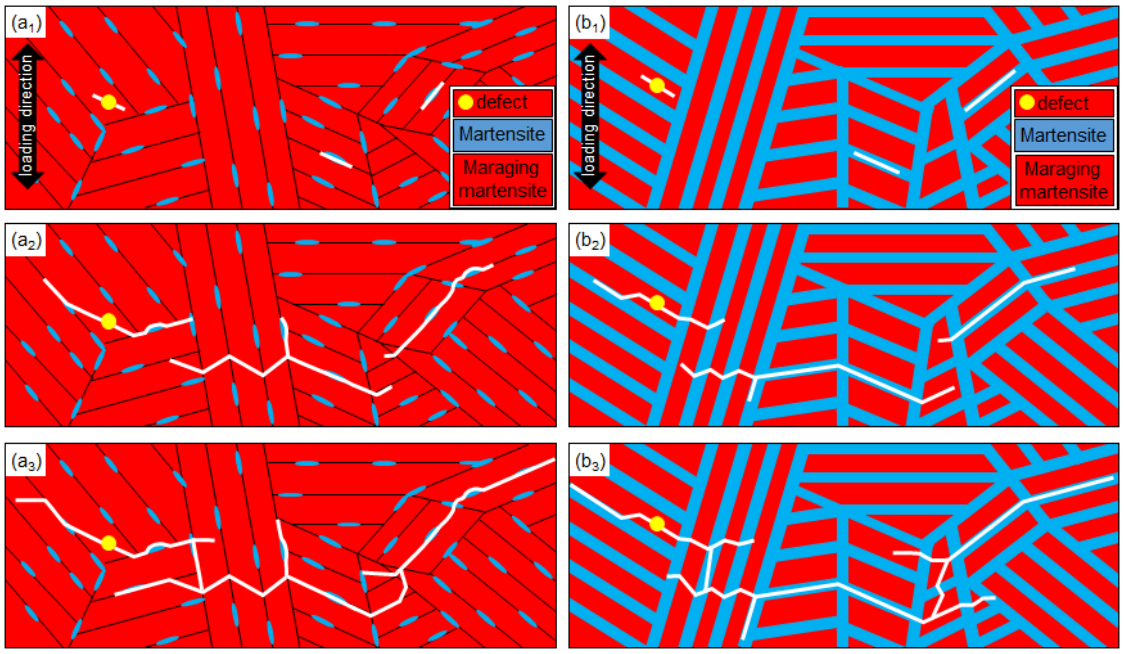

Fig. 5.6. Schematic of fatigue crack behavior at low cycle fatigue in (a) 1 h-steel and (b) 8 h-steel. (a_1, b_1) Cracks initiate from defect and transformed martensite region. (a_2, b_2) Cracks across maraging martensite blocks form submicrometer-scale roughness; Lamellar alignments build up micrometer-scale roughness. (a_3, b_3) Crack coalescences contribute to the micrometer-scale roughness. The white lines indicate fatigue crack.

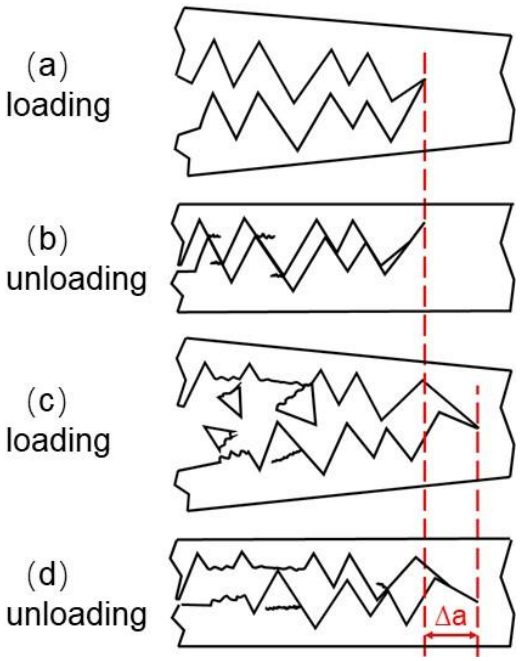

Fig. 5.7. Schematic of the submicrometer-scale roughness evolution during fatigue crack propagation. (a) Submicrometer-scale roughness is generated near crack tip. (b) Crack surfaces contact each other results in flaws on asperities. (c) Relative slip between both surfaces causes the asperities fracture. (d) The worn surface becomes smooth without RICC effect. Δa is fatigue crack growth length.

CHAPTER 6. General Conclusions and Outlook

6.1 Conclusions

As a new alloy, TRIP-maraging steel presents a robustness in fatigue performance. This attributed to two aspects in terms of laminated austenite/maraging martensite structure and deformation-induced martensitic transformation. Laminated structure resisting crack growth is predominantly due to roughness-induced crack closure (RICC) stemming from a zigzag crack propagation path within the austenite region. Martensitic transformation, which causes volume expansion from face centered cubic (FCC) to body centered cubic (BCC), decelerates crack growth rate by increasing local hardness and transformation-induced crack closure.

Here, it is worth noting that presently experimental TRIP-maraging steel is still not optimized, specifically on the aspect of the austenite fraction. Results show that austenite strength decreases with annealing time. Thus, crack preferentially initiates from inclusion in the TRIP-maraging steel annealed at 873 K for 1 h, while occurs at austenite region in the steel annealed for 8 h. However, the total fatigue life of short annealing steel is superior. In other words, steel annealed for 1 h shows great potential on fatigue initiation life if the inclusion issue can be effectively controlled.

In terms of maraging martensite, it also contributes fatigue resistance because of the high strength stemming from the intermetallic compounds resistance to the motion of

dislocation. Similarly, dislocation from austenite is restricted to transmit into maraging martensite. Therefore, experimental results show that crack along austenite-related regions. As mentioned above, austenite transformation to martensite contributes to crack growth deceleration. However, according to the experimental results and microstructural mechanism on dislocation motion, austenite is preferentially site for crack propagation, due to the elastic misfit among maraging martensite, transformation-induced martensite and austenite. Therefore, austenite fraction is intrinsically critical factor. The steel with high austenite fraction, i.e., high degree of austenite connectivity, has a rapid crack propagation.

Laminated microstructure contributes to zigzag crack path and promotes the associated roughness-induced crack closure (RICC). RICC related to the wear resistance has been clarified via three-dimensional serial sectioning. The roughness far from the crack tip easily disappears with number of cycles in a soft material, and thus hardness effect on wear behavior of crack surface roughness involves a wide crack length range. The wear resistance related to hardness is verified as present work. More specifically, the higher hardness obtained through controlling the annealing time enables to improve wear resistance. Therefore, the hardness is crucial criteria for RICC.

6.2 Outlook

According to the present work, it is worth further studying RICC effect, particularly quantify the effect of friction stress on roughness, which will significant contribute to fatigue life prediction and improvement of finite element method accuracy. For small crack, ΔK_{th} in TRIP-maraging steel should be lower than that in maraging steel owing to the yield stress dependence. However, the existing of RICC effect might influence the

value of ΔK_{th}. It is expected that ΔK_{th} in TRIP-maraging steel increases sharply with small crack length due to the roughness formation, compared to that in maraging steel. This experiment will be carried out using different size of notched specimen. In addition, present work shows that TRIP-maraging steels have large potential in mechanic properties. In order to reduce the negative effect that initial crack grows rapidly along austenite-related boundary, grain size reduction might be a solution. This strategy can simultaneously enhance crack deflection frequency, material hardness and associated wear resistance. However, decreasing grain size can cause a drop in roughness height. It would be interesting to exploring the influence of these variations on RICC. Considering the situation of engineering application, welding process is used widely for assembling and frame structure. The microstructure matrix of weld pool of TRIP-maraging steel should be fully lath martensite, and residual stress is generated during welding. In order to obtain fine laminated microstructure with specific mechanic properties, it is essential to carry out annealing heat treatment. Correspondingly, the effect of microstructure and residual stress on fatigue crack resistance needs to be examined.

From the viewpoint of modern industries, specifically in automobile industry, ferrite/martensite dual-phase (DP) steels and TRIP aided multi-phase steels have been widely used in the frame structure and body sheets, because of extraordinary formability combined with shock absorption energy. The applications of these steels in automobile have same goal that simultaneous increasing the structure strength and reducing CO_2 emission through lowing thickness of body sheets. Experimental results show that TRIP-maraging steel is superior to DP steel and TRIP steel in not only tensile properties, but also fatigue performance. Therefore, probably, TRIP-maraging steel would be the next generation material in automobile industry.

Acknowledgement

This study was conducted in the Solid Mechanics Laboratory, Department of Mechanical Engineering, Kyushu University, Japan. Firstly, I would like to give my sincere gratitude to Professor Hiroshi Noguchi for giving me opportunity to do research. Under his guidance, I understand the importance of originality, which makes human being life convenient, interesting and bright, and even leads society development. I am also honored for receiving guidance from Professor Kaneaki Tsuzaki. His mental spirit reminds me to keep an optimistic and positive attitude in work. I also appreciate the valuable advice from Professor Hiroyuki Toda for my PhD thesis. I also would like to express my appreciation to Assistant Professor Motomichi Koyama for his great support in my research work. He is admirable man with rich knowledge and humor. In addition, I want to thank Associate Professor Shigeru Hamada for his careful instruction in CAE application.

I would like sincerely thank Doctor Meimei Wang from Max-Planck-Institut für Eisenforschung and Professor Cemal Cem Tasan from Massachusetts Institute of Technology for preparing experimental materials. I also want to thank my friends for their help in my study and sharing colorful life with me. Finally, I want to thank my family for their understanding, encouragement and support.

Zhang Zhao

Japan, July 2018